On the Frame of Reference in Flow Visualization

Master's Thesis
by
Philipp Jung

A document submitted in partial fulfillment of the requirements for the degree of
Master of Science (M.Sc.)
at

RUPRECHT-KARLS-UNIVERSITÄT HEIDELBERG
INSTITUT FÜR INFORMATIK
VISUAL COMPUTING GROUP

Name:	Philipp Jung
Matrikelnummer:	3223122
Betreuer:	Prof. Dr. Filip Sadlo
Datum der Abgabe:	15.03.2019

Hiermit versichere ich, dass ich die vorliegende Masterarbeit selbstständig verfasst und nur die angegebenen Quellen und Hilfsmittel verwendet habe.

Heidelberg, den 15 März 2019

Philipp Jung

Abstract

Motivated by the developments of objective feature extraction frameworks in the years 2017/18 [GGT17; GT18a] and 2019 [Had*19] we review the dependence of vortex core line extraction and time-dependent vector field topology on the respective frame of reference. We compare these frameworks based on their physical interpretability, computation times and quality of resulting features. This includes an evaluation of the author's claims that their frameworks can find local frames of reference in which time-dependent vector fields appear steady. We explore limitations and demonstrate that the birth and death of critical points pose a fundamental problem for this goal. Our findings establish that the transfer of visualization techniques from the steady to the time-dependent case is only possible if the original field appears truly steady in the computed frames of reference. We continue to show that this is a special case, and does not hold for real-world examples. In extension to this, we show that the extraction of hyperbolic trajectories via parallel vectors in these frames of reference can mitigate problems related to curved solutions. For the two-dimensional case, we additionally prove the equivalence of parallel vectors solutions and critical points in the newly created steady vector field. Moreover, we demonstrate that invariant manifolds from the steady frame of reference have very limited meaning for the original vector field.

Zusammenfassung

Inspiriert von den aktuellen Entwicklungen von objektiven Feature-Extraktion Frameworks der Jahre 2017/18 [GGT17; GT18a] und 2019 [Had*19], überprüfen wir die Abhängigkeit von Wirbelkernlinien und zeitabhängiger Vektorfeld-Topologie von dem jeweiligen Bezugssystem. Wir vergleichen diese Frameworks anhand ihrer physikalischen Interpretation, Rechenzeit und Qualität der Resultate. Dies umfasst eine Evaluation der Aussage der Autoren, dass diese Frameworks lokale Bezugssysteme finden in denen zeitabhängige Vektorfelder stationär erscheinen. Des Weiteren untersuchen wir mögliche Einschränkungen dieser Techniken und demonstrieren, dass die Entstehung sowie die Auflösung von kritischen Punkten ein fundamentales Problem für das Erreichen dieses Zieles darstellen. Unsere Ergebnisse zeigen, dass Methoden der stationären Vektorfeldvisualisierung nur in den zeitabhängigen Fall übertragen werden können, wenn das originale Vektorfeld hinsichtlich des berechneten Bezugsystems tatsächlich stationär ist. Wir zeigen weiter auf, dass es sich hierbei nur um Spezialfälle handelt und die Techniken nur bedingt auf reale Probleme übertragen werden können. Weiterführend erörtern wir, dass die Extraktion von hyperbolischen Trajektorien verbessert werden kann indem Parallel Vectors (PV) in dem neuen Bezugssystem angewendet werden, und so Probleme, die bei gekrümmten Lösungen auftreten, vermieden werden. Für den zweidimensionalen Fall beweisen wir zusätzlich die Äquivalenz von kritischen Punkten in Beobachter-Vektorfeldern und der Anwendung von PV auf das ursprüngliche Vektorfeld und das Beobachter-Vektorfeld. Darüber hinaus demonstrieren wir, dass Separatrizen und die Stabilität von kritischen Punkten des stationären Feldes nur eine begrenzte Aussagekraft für das ursprüngliche Vektorfeld haben.

Contents

1 Introduction

The ultimate goal of many theories in the natural sciences is the ability to make accurate predictions of natural systems. A model must be able to explain phenomena observed in the past and is used as a basis for future predictions. To this end, a mathematical foundation is required, and for a wide variety of phenomena, from the behavior of fluids to the orbits of planets, dynamical systems serve as this mathematical basis. For example, meteorologists use dynamical systems and vector fields to describe the behavior of the atmosphere of the Earth. However, in order to accurately represent such complex natural phenomena the models themselves become quite complex. Consider such a model of the Earth's atmosphere that describes the motion of individual particles. How can scientists gain insight into large-scale phenomena like tornados or tropical storms? A prominent way to do this is information reduction, i.e., extract the most relevant structures from the dynamical system and visualize them in a concise way. In case of a vortex, e.g., a tornado, we can capture a large part of the information by representing the central axis around which the air rotates. The field of scientific visualization aims to find methods and visualization techniques that can concisely represent features like vortex core lines, i.e., the central rotational axis of a tornado. Vortex core lines are just one of many features. These features include ridges and valleys, local minima and maxima of scalar fields, Lagrangian coherent structures, structures within a fluid that separate particles into regions of different behavior, and many more. What many of these features have in common, is the fact that they are more or less visible or invisible, depending on the respective observer. By an observer we mean a frame of reference, i.e., some reference relative to which we can make measurements. Consider for example, a ball repeatedly thrown up in the air by a passenger on a train. From the perspective of the passenger the ball only moves up and down, but for an observer standing outside and observing the train passing by, the ball additionally moves in the direction of the train. We know that within all inertial reference frames, i.e., frames that are only rotated and constantly translated, the observed physical phenomena are equivalent. However, feature extraction techniques typically explicitly depend on the frame of reference, and may give different solutions for different frames of reference. For example, the common vortex core line extraction by Sujudi and Haimes [SH95b] exploits the parallelism of velocity and acceleration. From this we directly see that a constant speed translation changes the velocity and thereby impacts the extraction of vortex core lines. In order to mitigate these problems, feature extraction techniques that are invariant under certain classes of observer motion have been introduced. Although these problems are not limited to vortices, vortex extraction has been the driving force behind these developments [Hal05; RP98; Wei*07b].

In recent years, research has shifted from the formulation of invariant feature extraction techniques to the development of frameworks, that allow existing methods to become objective, i.e., invariant under rigid body motion of the frame of reference. In 2017 Günther et al. [GGT17] presented a framework that enables existing vortex measures to become objective. Shortly after, in 2018, they introduced a revised version that includes invariance under affine observer transformations. While both methods build on a discrete neighborhood, Hadwiger et al. [Had*19] introduced a similar technique in 2019 that operates globally, thereby, bypassing the need for a discrete neighborhood. We present the three techniques in detail in Chapter 6.

1.1 Related Work

In the context of frame-independent feature extraction, we distinguish the following classes of observer motion: 1) Galilean, i.e., constant speed translation, and 2) rigid body, i.e., continuous rotation and translation. Later, we additionally take a look at general affine transformations which include scaling and shearing. Techniques that are invariant under the respective classes are called: Galilean invariant, objective, and hyperobjective. Sometimes the subclass of rotation invariant measures is included, it resides between Galilean invariance and objectivity. Vortices have traditionally been one of the most important features in fluid visualization and early definitions are especially sensitive to changes of the frame of reference. For this reason, vortex extraction has been a key driving factor in the development of Galilean invariant and objective methods. Vortex extractors are typically divided into line-based and region-based methods.

Region-based methods highlight regions within the flow that exhibit vortex-like behavior. Typical these volume-like structures are found by thresholding of vortex indicator fields like pressure or vorticity. Today, the λ_2 criterion by Jeong and Hussain [JH95] and the Q criterion by Hunt et al. [Hun87; HWM88] are widely used for the extraction of vortex regions. Combinations and further developments based on these criteria were introduced by Biswas et al. [Bis*15]. More recently, an objective vortex measure was presented by Haller [Hal05], and a Galilean invariant vortex region criterion was presented by Kasten et al. [Kas*11; Kas*12].

Line-based methods aim to find the common axis around which fluid particles rotate. One of the first approaches was presented by Sujudi and Haimes [SH95b] which is based on the eigenvalues and eigenvectors of the Jacobian of the flow. Peikert and Roth [PR99] later introduced the parallel vectors (PV) operator and showed that the criterion of Sujudi and Haimes may be expressed as the parallelism of velocity and acceleration. They further developed a higher order method that addresses the problems related to curved vortex core lines [RP98], but introduce their own class of detection issues. Sahner et al. [Sah*07; SWH05] proposed a Galilean invariant vortex core line extractor based on extremum-lines of region based-criteria such as the λ_2 and Q criterion.

The above mentioned techniques mainly focus on steady, time-independent dynamical systems. For the extension to time-dependent flows, Theisel et al. [The*05a], Fuchs et al. [Fuc*08] and Weinkauf et al. [Wei*07b] base their vortex extraction techniques on a derived vector field, called feature flow field [TS03]. The feature flow field transforms the original vector field into a locally Galilean invariant frame, and hence, methods based upon it, become Galilean invariant as well. The idea behind these time-dependent vortex extractors is to find a suiting (local) frame of reference in which the vector field appears steady. And thus, methods originally developed for steady vector fields may be applied to time-dependent vector fields within the new frame of reference. The most basic frame transformation is the subtraction of a mean flow. This approach models an observer that moves with constant velocity, the mean velocity, with the flow [Wei*07b]. We distinguish two types, on the one hand, methods that find a single global frame of reference, i.e., one observer, and on the other hand, methods that find local frames of reference, i.e., multiple observers. Such a single Euclidean observer is related to the standard frame of reference, sometimes called lab frame, in the sense that it is a transformed version of the same. The transformation between Euclidean frames of reference according to Truesdell and Noll [TN04] is discussed in Section 3.1. The subtraction of a mean flow falls in the first category of a global observer. The application of a similar transformation was presented by Haller et al. [Hal*16], where the authors model a frame of reference spinning with the average vorticity of the flow.

However, as Perry and Chong [PC87] showed, a single observer is not able to view general vector fields as steady. Therefore, in order to steadify a time-dependent vector field, multiple observers that are able to adapt locally, are required. The feature flow field [TS03] is an example of such an approach. Since then, a multitude of techniques based on local frames of reference have been presented, including the aforementioned time-dependent vortex extractors based on the feature flow field [Fuc*08; The*05a; Wei*07b]. This steadification of vector fields allows for the application of other techniques from steady vector field visualization to the time-dependent case. Bujack et al. [BHJ16] proposed to use multiple observers based on the loci of Galilean invariant critical points, isolated zeros of the vector field, and compute steady vector field topology from those. Recently, Günther and Theisel presented frameworks that compute such local observers for general vector field such that the observed field appears as steady as possible. These frameworks are rotation invariant [GST16], objective [GGT17], and finally hyperobjective [GT18a]. Wiebel et al. [WGS02; WSG04] decompose a vector field into a localized component and a harmonic component and base their analysis on the localized component. Bhatia et al. [Bha*13; Bha*14] presented local frames of reference based on the Helmholtz-Hodge decomposition (HHD), that partitions a vector field into a curl-free, a divergence-free and harmonic part. They extended their work to account for boundary conditions by introducing the natural Helmholtz-Hodge decomposition [BPB14]. Finally, Hadwiger et al. [Had*19] addressed advantages and problems of both local and global observers and presented a hybrid approach that aims to find locally adaptive observers that globally behave as similar as possible.

There exist a multitude of techniques that aim to find (local) reference frames that allow the application of techniques from steady vector field visualization to the time-dependent case. This motivates us to investigate not only their practical applicability but also their physical interpretations. The frameworks of Hadwiger et al. [Had*19] and Günther et al. [GGT17; GT18a] introduced in 2019 and 2017/18, respectively, incorporate a large set of ideas presented on this topic in the last decade. Therefore, in this thesis we focus on these two frameworks. Our contributions include:

- A comprehensive comparison of the two frameworks based on their ability to find suiting frames of reference for both analytical and real-world datasets. This includes a study on vortex core extraction in steady frames of reference.
- Detailed investigations on feature extraction in the steady frame and their relation to phenomena of the original unsteady vector field, specifically steady vector field topology. We show how this relates to streak-based vector field topology [SW10] and the extraction of hyperbolic trajectories.
- Evidence that these frameworks are able to find (local) frames of reference in which certain classes of time-dependent vector fields appear steady, but are unable to provide such frames in general.
- A proof that, generally, we cannot transfer methods from steady vector field visualization to the time-dependent case.

Furthermore, we show that the current time-dependent method, streak-based vector field topology, may be improved by applying it in the objective frames provided by these techniques and evaluate in practical use-cases. In extension to this, we demonstrate that this can avoid problems related to curved solutions of the parallel vectors operator [PR99]. Finally, we extend parts of our findings to the three-dimensional case and put these techniques into context to other vector field decompositions, like the Helmholtz-Hodge decomposition.

1.2 Overview

In Chapter 2, we introduce basic notions required within this thesis. We present frames of reference and observer relative motion in Chapter 3 before we briefly review vortex extraction methods in Chapter 4. The traditional notion of steady vector field topology and possible time-dependent counterparts are reviewed in Chapter 5. Historically, vortex extraction has been the key driving force behind local frames of reference introduced in Chapter 6. Building on this, in Chapter 7 we formulate and discuss open research questions and implications that arise from these techniques and present the methodology employed in Chapter 8 to explore these topics.

2 Dynamical Systems and Vector Fields

In this chapter, we introduce fundamental notions, definitions, and terminology related to dynamical systems and vector fields. The nomenclature and certain definitions are adapted from Wiggins [Wig03], and Guckenheimer and Holmes [GH13].

Dynamical systems are widely used in mathematics, physics, chemistry and other fields to give natural phenomena a theoretical basis. We distinguish autonomous dynamical systems, that do not explicitly depend on time, and non-autonomous (time-dependent) systems. An autonomous dynamical system is defined by an equation:

$$\dot{\mathbf{x}} = \mathbf{u}(\mathbf{x}), \quad \mathbf{x}(t_0) = \mathbf{x}_0, \tag{2.1}$$

where $\dot{\mathbf{x}} := \frac{\mathrm{d}\mathbf{x}}{\mathrm{d}t}$. $\mathbf{x}(t) \in \mathbb{R}$ is the state of the system at time t and $\mathbf{u} : \mathbb{R}^n \to \mathbb{R}^n$ is its vector field. Since autonomous systems do not depend on time, we may set the initial time $t_0 = 0$. A dynamical system that explicitly depends on time

$$\dot{\mathbf{x}} = \mathbf{u}(\mathbf{x}, t), \quad \mathbf{x}(t_0) = \mathbf{x}_0, \tag{2.2}$$

is called non-autonomous or time-dependent. Autonomous systems are sometimes referred to as steady, and non-autonomous system as unsteady. Further, we call an autonomous dynamical system linear, if its vector field $\mathbf{u}(\mathbf{x})$ is a linear map. For non-autonomous or time-dependent systems we require its vector field $\mathbf{u}(\mathbf{x}, t)$ to be linear in $\mathbf{x}$. By a solution of Equation (2.1) we mean a map $\mathbf{x}$

$$\begin{aligned} \mathbf{x} : \mathbb{R} &\to \mathbb{R}^n \\ t &\mapsto \mathbf{x}(t) \end{aligned} \tag{2.3}$$

in a way that $\mathbf{x}(t)$ satisfies

$$\dot{\mathbf{x}}(t) = \mathbf{x}(\mathbf{x}(t)). \tag{2.4}$$

This map $\mathbf{x}$ can be interpreted as a curve in $\mathbb{R}^n$ where Equation (2.1) gives the tangent vector at each point of the curve. A specific solution is often identified by a point in space it passes through at a given time, i.e., $\mathbf{x}(t_0) = \mathbf{x}_0$. We can include this into the original expression, by as $\mathbf{x}(t, t_0, \mathbf{x_0})$. Now, the geometrical interpretation of a solution as a tangent curve becomes clear, i.e., as the graph of $\mathbf{x}(t, t_0, \mathbf{x}_0)$.

Definition 2.1 (Tangent Curve)**.** Let $\mathbf{u} : \mathbb{R}^n \to \mathbb{R}^n$ be an n-dimensional vector field. Then $\mathcal{L}(s) \in \mathbb{R}^n$ is called tangent curve of $\mathbf{u}$, if the tangent vectors of $\mathcal{L}(s)$ are given by $\mathbf{u}(\mathbf{x})$, where s parameterizes the curve. Tangent curves are solutions of autonomous systems of ordinary (ODE) or partial (PDE) differential equations.

$$\frac{\mathrm{d}}{\mathrm{d}s}\mathcal{L}(s) = \mathbf{u}(\mathcal{L}(s)), \quad \mathcal{L}(0) = \mathbf{x}_0 \tag{2.5}$$

Note that for all $\mathbf{x}$, where $\mathbf{u}(\mathbf{x}) \neq \mathbf{0}$, there exists a unique tangent curve through the point $\mathbf{x}$. Hence, tangent curves cannot intersect each other.

Following the definition of Marsden and Hughes [MH94], solutions to the initial value problem (IVP) of a dynamical system as defined by Equations (2.1) and (2.2) are called flow. The flow of a time-independent vector field $\mathbf{u}(\mathbf{x})$ defined on $\mathbb{R}^n$ is a map $\phi : \mathbb{R} \times \mathbb{R}^n \to \mathbb{R}^n$ that sends a point $\mathbf{x}$ to its image along the integral curve of $\mathbf{u}$ through $\mathbf{x}$ after time t. We denote this by $\phi_t(\mathbf{x})$.

This concept is analogously extended to the time-dependent case by including time as explicit parameter into Equation (2.4): $\dot{\mathbf{x}}(t) = \mathbf{u}(\mathbf{x}(t), t)$. Thus, the time-dependent flow $\Psi : I \times I \times \mathbb{R}^n \to \mathbb{R}^n$ maps a point $\mathbf{x} \in \mathbb{R}^n$ at time s to its image along the integral curve of $\mathbf{u}(\mathbf{x}, t)$ at time t. We denote this by $\Psi_{t,s}(\mathbf{x})$. As a side note, the notion of Ψ is also applicable in the time-independent case: $\Psi_{t,s}(\mathbf{x}) = \phi_{t-s}(\mathbf{x})$. The one-parameter family of flows describes all solutions of a dynamical system, typically referred to as the flow map of the vector field. In flow visualization, the flow $\Psi_{t,s}$, is often written as ϕ_t^τ usually with the meaning $\Psi_{t+\tau,t}$. However, we chose to follow the first notion where $\Psi_{t,s}^{-1} = \Psi_{s,t}$ holds, which simplifies notation later on.

2.1 The Space-Time Domain

In some cases it might be desireable to represent a time-dependent vector field as a steady one. An n^{th} order time-dependent system can by transformed to an $(n+1)^{\text{th}}$ order time-independent system by the use of an additional state δ:

$$\begin{aligned} \dot{\mathbf{x}} &= \mathbf{u}(\mathbf{x}, \delta), & \mathbf{x}(t_0) &= \mathbf{x}_0, \\ \dot{\delta} &= 1, & \delta(t_0) &= t_0. \end{aligned} \tag{2.6}$$

Solutions of the new steady system are of the form

$$\begin{pmatrix} \mathbf{x}(t) \\ \delta(t) \end{pmatrix}. \tag{2.7}$$

This can be seen as stacking the vector field at increasing time steps (Figure 2.1).

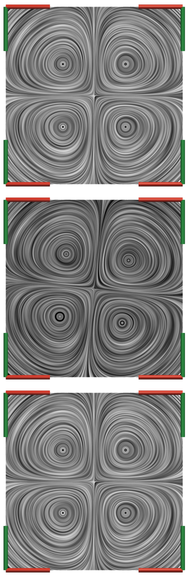

(a) Selected Time Steps

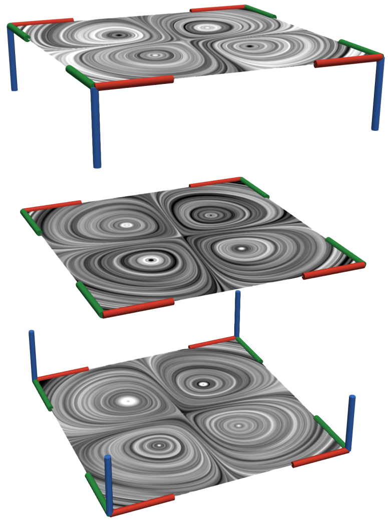

(b) Space-Time Representation

Figure 2.1: Selected time-steps of the time-dependent four centers model, discussed later in Section 8.1.1, show four centers rotating around each other. The instantaneous behavior of tangent curves of the vector field is visualized as line integral convolution (LIC) (a). The corresponding space-time representation shows the same selected time steps. The slices are translated along the time axis, i.e., time is represented as additional dimension, increasing from bottom to top (b).

2.2 Characteristic Curves of Vector Fields

For steady (time-independent) systems, tangent curves are called streamlines. Unsteady (time-dependent) vector fields have two additional types of characteristic curves, pathlines and streaklines. All three types coincide in the case of steady vector fields. Figure 2.2 shows an interpretation of all three types.

2.2.1 Streamlines

Streamlines, sometimes called field lines, are tangent curves of the vector field frozen at a fixed point in time $\bar{t}$. They are interpreted as trajectories of massless particles tangentially following the flow, as illustrated in Figure 2.2a.

$$\frac{\mathrm{d}}{\mathrm{d}s}\mathcal{L}(s) = \mathbf{u}(\mathcal{L}(s), \bar{t}\,), \quad \mathcal{L}(0) = \mathbf{x}_0. \tag{2.8}$$

Streamlines are obtained by integrating Equation (2.8)

$$\mathcal{L}(s) = \mathbf{x}_0 + \int_{s_0}^{s} \mathbf{u}(\mathcal{L}(\tau), \bar{t}\,)\,\mathrm{d}\tau. \tag{2.9}$$

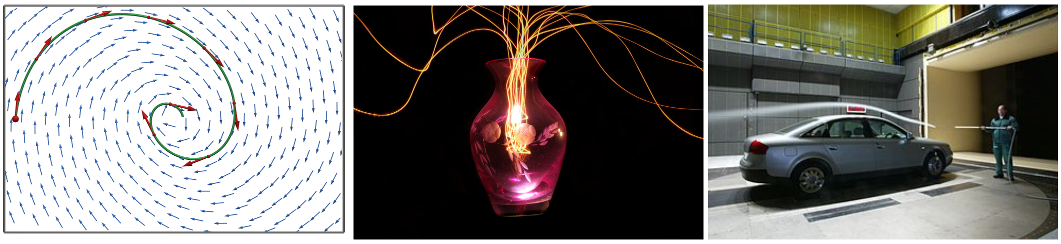

(a) Streamline (b) Pathline (c) Streakline

Figure 2.2: The three types of characteristic curves depicted: Streamlines (a) shown in green, follow the instantaneous vector field (blue arrows). The red arrows indicate that the streamline follows the vector field tangentially. A long-exposure shot of sparks escaping from a vase (b) [Com14]. Under the assumption that the sparks are massless, their trajectories are pathlines. Streaklines used to visualize the flow around a car inside a wind tunnel (c) [Com18]. They are obtained by continuously seeding particles in front of the car.

Figure 2.2a depicts a streamline (green) within a steady vector field visualized by blue arrows. Since streamlines characterize the vector field frozen at a fixed point in time, they exist only within this time step in the space-time domain as depicted in Figure 2.3. To obtain stream lines within the space-time domain, the time parameter is frozen, i.e., the streamlines live in a slice orthogonal to the time-axis.

$$\frac{\mathrm{d}}{\mathrm{d}s}\begin{pmatrix}\mathcal{L}\\ s\end{pmatrix} = \begin{pmatrix}\mathbf{u}(\mathcal{L}(s),\bar{t}\,)\\ 0\end{pmatrix}, \quad \begin{pmatrix}\mathcal{L}\\ s\end{pmatrix}(0) = \begin{pmatrix}\mathbf{x}_0\\ s_0\end{pmatrix}. \tag{2.10}$$

We may describe them by tangent curves of the derived space-time vector field

$$\mathbf{p}(\mathbf{x},t) := \begin{pmatrix}\mathbf{u}(\mathbf{x},t)\\ 0\end{pmatrix}. \tag{2.11}$$

$\mathcal{L}(\mathbf{x}_0,\bar{t}\,)$ denotes a streamline, i.e., the tangent curve through $\mathbf{x}_0$ at time $\bar{t}$.

2.2.2 Pathlines

In contrast to stream lines, path lines take the change of the underlying vector field into account. We can think of this as massless particles moving tangentially along a changing velocity field, as illustrated in Figure 2.2b.

$$\frac{\mathrm{d}}{\mathrm{d}s}\mathcal{L}(s) = \mathbf{u}(\mathcal{L}(s),t\,), \quad \mathcal{L}(t_0) = \mathbf{x}_0. \tag{2.12}$$

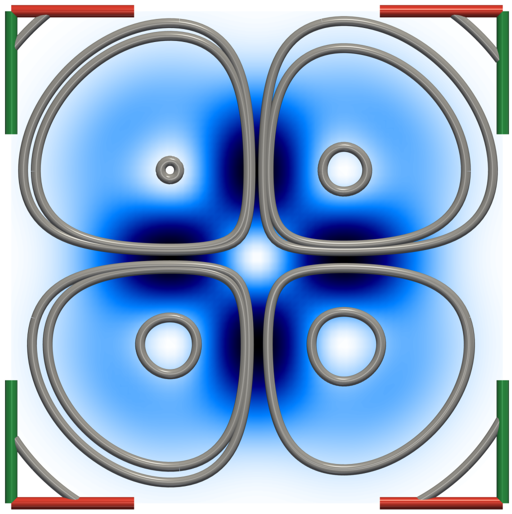

(a) Streamlines

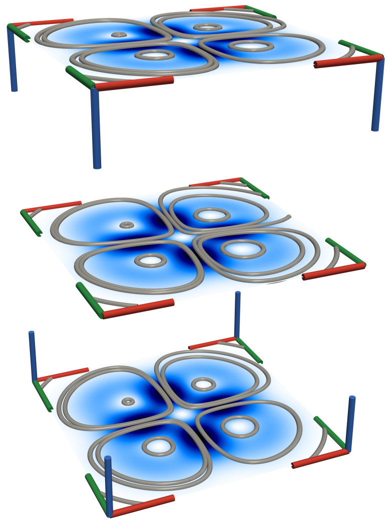

(b) Space-Time Streamlines

Figure 2.3: Streamlines of the four centers model frozen at time $\bar{t} = 0$ (a). The corresponding streamlines at different time steps of the vector field within the space-time domain (b). Holding t constant corresponds to a tangent curve that lies within a time-slice, i.e., the last component of the derived space-time field is set to 0.

Analogously to streamlines, pathlines are obtained by integrating Equation (2.12). Their space-time version are tangent curves of the derived space-time field

$$\mathbf{p}(\mathbf{x}, t) := \begin{pmatrix} \mathbf{u}(\mathbf{x}, t) \\ 1 \end{pmatrix}, \tag{2.13}$$

and may be obtained by integrating the autonomous system

$$\frac{\mathrm{d}}{\mathrm{d}s} \begin{pmatrix} \mathcal{L} \\ t \end{pmatrix} = \begin{pmatrix} \mathbf{u}(\mathcal{L}(t), t\,) \\ 1 \end{pmatrix}, \quad \begin{pmatrix} \mathcal{L} \\ t \end{pmatrix}(0) = \begin{pmatrix} \mathbf{x}_0 \\ t_0 \end{pmatrix}. \tag{2.14}$$

Figure 2.4 shows an example in both space and space-time domain. $\mathcal{L}(\mathbf{x}_0, t_0; t)$ denotes a pathline, meaning the tangent curve with initial conditions $(\mathbf{x}_0, t_0)$.

2.2.3 Streaklines

Streaklines are obtained by continuously seeding particles at a fixed position and interpreting the connection set of these particles as a connected line. Think of this as continuously releasing dye from a fixed position into the surrounding flow, compare Figure 2.2c. The resulting line pattern is called a streakline. Streaklines are commonly used to reveal features like vortices. More precisely, a streakline is the set of all particles at a given point in time that have past through the same

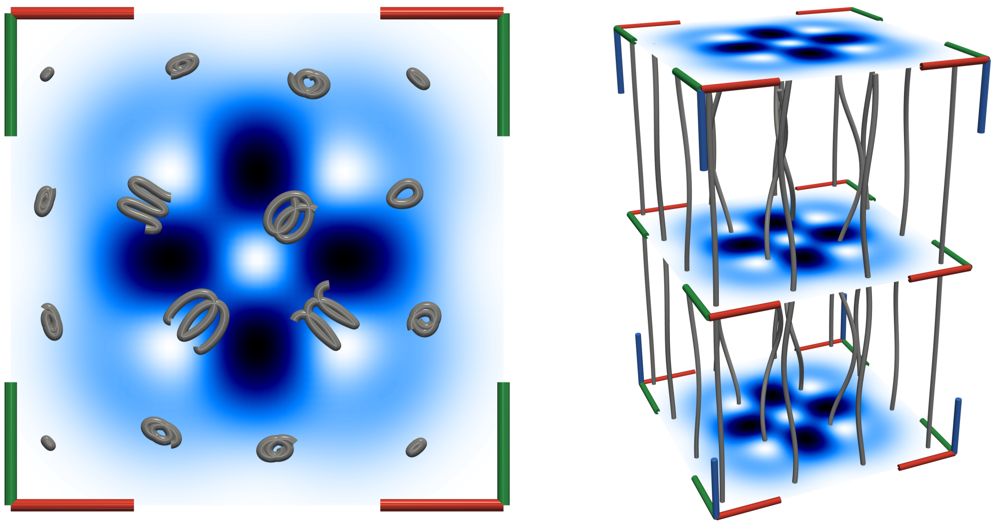

(a) Pathlines (b) Space-Time Path Lines

Figure 2.4: Pathlines of the vector field seeded at time t_0 (a). Streamlines of the corresponding space-time vector field (b). These streamlines in the extended domain correspond to pathlines in the original 2D domain. We may obtain pathlines of the original time-dependent field by computing streamlines in the space-time domain and then projecting them onto the x-y plane.

point in space some time in the past. In contrast to streamlines, one cannot identify streaklines solely by a point in space and time.

Computationally, streaklines of a time-dependent vector field may be obtained by first computing a stream surface in the derived vector field $\mathbf{p}(\mathbf{x}, t)$, seeded along a line segment starting from a point $(\mathbf{x}, t_0)$ extending in positive t-direction parallel to the t-axis, see Figure 2.5a. A stream surface is the union of streamlines seeded continuously along a seeding curve. The streakline at time τ is then given by the intersection curve of this surface with the hyperplane at $t = \tau$. According to Weinkauf and Theisel [WT10] streaklines may also be obtained by tangent curves of a derived vector field based on the evaluation of the flow map.

Generalized Streaklines [Wie*07] One may allow motion of the seed location of the stream surface. This corresponds to a moving seed that continuously releases dye into the flow. For the computation, this means the seed curve in space-time can have arbitrary form, while evolving in positive time direction (Figure 2.5b).

2.3 Total Derivative

Before we move on to stability considerations of trajectories, we shortly introduce the total derivate needed for further analysis. The total derivative, in contrast to

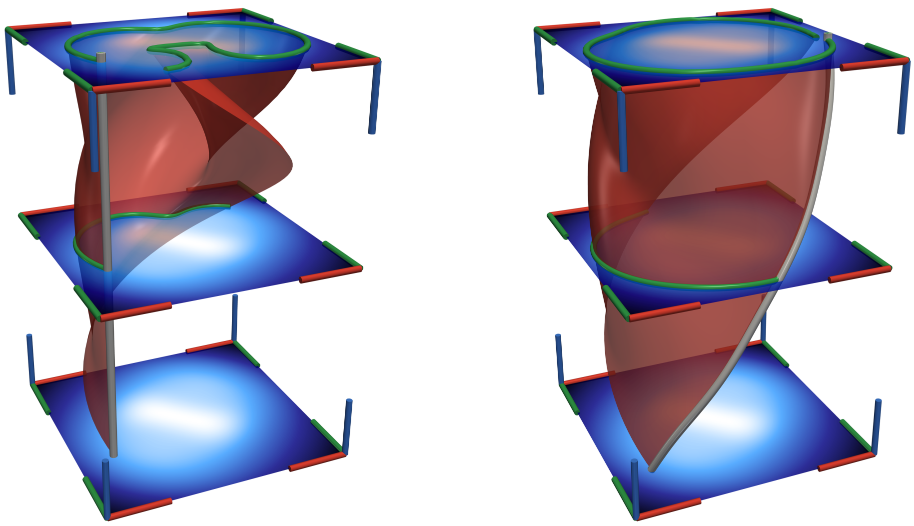

(a) Space-Time Streakline (b) Generalized Space-Time Streakline

Figure 2.5: The seed location (gray vertical tube) in space-time corresponds to a single stationary seed point in space. Seeding particles at this location continuously over time translates to seeding streamlines with continuously increasing t component, i.e., along the gray vertical tube. Streaklines (green) at a given time are then represented by the intersection curve of the stream surface (red), the union of all seeded streamlines, and a hyperplane perpendicular to the time axis (a). Generalized streaklines allow the seed to move continuously over time (gray tube), i.e., the line in space-time is no longer straight (b).

the partial derivative $\frac{\partial f}{\partial t}$—which captures the change of f given the change in t—assumes that the other arguments $\mathbf{x}(t)$ of f also depend on t and takes these into account, to find the overall dependency of f on t. The total derivative of a function

$$\begin{aligned} f : \mathbb{R} \times \mathbb{R}^n &\to \mathbb{R} \\ (t, \mathbf{x}) &\mapsto s, \end{aligned} \tag{2.15}$$

is given by:

$$\frac{\mathrm{d}f}{\mathrm{d}t} = \frac{\partial f}{\partial t} + \sum_{i=1}^{n} \left(\frac{\partial f}{\partial x_i} \frac{\mathrm{d}x_i}{\mathrm{d}t} \right). \tag{2.16}$$

In the context of fluid mechanics the total derivative is called material derivative.

2.4 Stability of Trajectories

It is often of interest how solutions with small perturbations in initial conditions behave with respect to each other, i.e., the attracting or separating characteristics of trajectories. This is especially important in numerics where computationally ob-

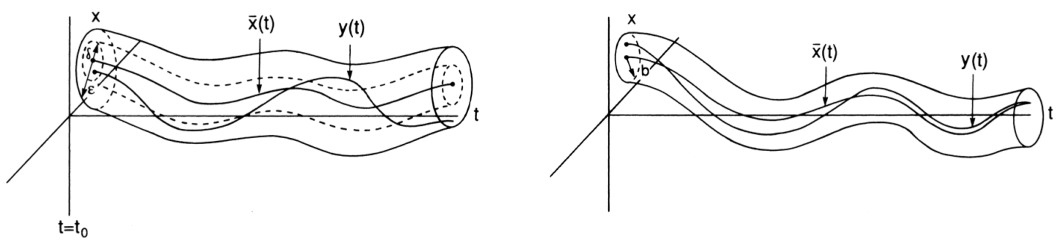

(a) Lyapunov Stability (b) Asymptotic Stability

Figure 2.6: Solutions $\mathbf{y}(t)$ started in the vicinity of $\mathbf{x}$ that stay within its vicinity are called Lyapunov stable (a). Solutions that additionally converge toward $\mathbf{x}$ are called asymptotically stable (b). Images from Wiggins [Wig03] [a].

[a] Adapted by permission from Springer Nature: Springer eBook S.Wiggins. Introduction to applied nonlinear dynamical systems and chaos, pages 10-22, Springer Science & Business Media, 2003

tained solutions may include numerical errors which can be amplified during integration. We differentiate two types of stability 1) Lyapunov stability, and 2) asymptotic stability. Roughly speaking, a solution $\mathbf{x}(t)$ is called stable (or Lyapunov stable) if solutions starting "close to" $\mathbf{x}(t)$ at a given time remain close to $\mathbf{x}(t)$. A solution is called asymptotically stable if nearby solutions not only stay close by but also converge toward $\mathbf{x}(t)$ as $t \to \infty$. Formally, these are defined as follows [Wig03]:

Definition 2.2 (Lyapunov Stability)**.** A solution $\mathbf{x}(t)$ is said to be stable (or Lyapunov stable) if, given a fixed $\epsilon > 0$, there exists a $\delta = \delta(\epsilon) > 0$ so that for any other solution, $\mathbf{y}(t)$ satisfying $\|\mathbf{x}(t_0) - \mathbf{y}(t_0) < \delta\|$ (with $\|\cdot\|$ being a norm on $\mathbb{R}^n$), follows $\|\mathbf{x}(t) - \mathbf{y}(t) < \epsilon\|$ for all $t > t_0, t_0 \in \mathbb{R}$.

Definition 2.3 (Asymptotic Stability)**.** A solution $\mathbf{x}(t)$ is called asymptotically stable if in addition to being Lyapunov stable there exists a constant $b > 0$ for any other solution $\mathbf{y}(t)$ so that $\|\mathbf{x}(t_0) - \mathbf{y}(t_0) < b\|$ then follows $\lim_{t\to\infty} \|\mathbf{x}(t) - \mathbf{y}(t)\| = 0$.

Figure 2.6 illustrates these two concepts and their differences. Solutions that are not (asymptotically) stable are called (asymptotically) unstable.

2.5 Linearization

In order to determine the stability of a solution $\mathbf{x}(t)$, one has to understand the behavior of solutions near $\mathbf{x}(t)$. Let an arbitrary solution near $\mathbf{x}(t)$ be given by

$$\mathbf{y}(t) = \mathbf{x}(t) + \mathbf{c}. \tag{2.17}$$

Substituting this into Equation (2.2) and Taylor expanding around $\mathbf{x}(t)$

$$\dot{\mathbf{y}} = \dot{\mathbf{x}}(t) + \dot{\mathbf{c}} = \mathbf{u}((\mathbf{x}(t)) + D\mathbf{u}(\mathbf{x}(t)) \cdot c + \mathcal{O}\Big(\|\mathbf{c}\|^2\Big), \tag{2.18}$$

where D is the total derivative of $\mathbf{u}$. Simplifying with $\dot{\mathbf{x}}(t) = \mathbf{u}(\mathbf{x}(t))$ yields

$$\dot{\mathbf{c}} = D\mathbf{u}(\mathbf{x}(t)) \cdot \mathbf{c} + \mathcal{O}\left(\|\mathbf{c}\|^2\right). \tag{2.19}$$

Equation (2.19) describes the evolution of solutions near $\mathbf{x}(t)$. For stability, only solutions arbitrarily close to $\mathbf{x}(t)$ are relevant. Thus, the linear system is studied:

$$\dot{\mathbf{c}} = D\mathbf{u}(\mathbf{x}(t)) \cdot \mathbf{c}. \tag{2.20}$$

Meaning, if $\mathbf{x}(t)$ is an equilibrium solution, then $D\mathbf{u}(\mathbf{x}(t)) = D\mathbf{u}(\mathbf{x})$ is a constant matrix, and a solution of Equation (2.20) through a point $c_0 \in \mathbb{R}$ can be written as

$$\mathbf{c}(t) = e^{D\mathbf{u}(\mathbf{x})t}\mathbf{c}_0. \tag{2.21}$$

Hence, a solution $\mathbf{c}(t)$ is asymptotically stable, if all eigenvalues of $D\mathbf{u}(\mathbf{x})$ have negative real parts. According to Wiggins [Wig03, Theorem 1.2.5] stability of the linearized system implies stability of the nonlinear system .

Theorem 2.4. A fixed point solution $\bar{\mathbf{x}} = \mathbf{u}(\mathbf{x})$ of the nonlinear system $\mathbf{u}$ is stable, if all eigenvalues of the Jacobian $\mathbf{J}_\mathbf{u}(\bar{\mathbf{x}})$ have negative real part.

D is the matrix of partial derivatives of $\mathbf{u}(\mathbf{x}(t))$ and is called the Jacobian matrix.

Definition 2.5 (Jacobian Matrix)**.** Given an n-dimensional vector field $\mathbf{u} : \mathbb{R}^n \to \mathbb{R}^n$, the Jacobian matrix at a point $\mathbf{x}$ is the $n \times n$ matrix of partial derivatives

$$\mathbf{J}_\mathbf{u}(\mathbf{x}) = \nabla\mathbf{u}(\mathbf{x}) = \begin{pmatrix} \frac{\partial}{\partial x_1}u_1 & \cdots & \frac{\partial}{\partial x_n}u_1 \\ \vdots & \ddots & \vdots \\ \frac{\partial}{\partial x_1}u_n & \cdots & \frac{\partial}{\partial x_n}u_n \end{pmatrix}. \tag{2.22}$$

In case of a time-dependent vector field $\mathbf{u} : \mathbb{R}^n \times \mathbb{R} \to \mathbb{R}^n$, the Jacobian matrix at point $\mathbf{x}$ in space and t in time is written as $\mathbf{J}_\mathbf{u}(\mathbf{x}, t)$. Since the gradients $\nabla u_1, \cdots, \nabla u_n$ are column vectors, but are here written as row vectors, the Jacobian matrix is sometimes defined as the transposed of the above. However, the advantage of this notation is that the linear approximation of the vector field $\mathbf{u}$ is given by left-multiplication of the Jacobian and the vector field.

2.6 Invariant Manifolds

For a fixed point $\bar{\mathbf{x}} = \mathbf{u}(\mathbf{x})$ we consider the local behavior of the linear system. The three subspaces of $\mathbf{J}_\mathbf{u}(\bar{\mathbf{x}})$ denoted $\mathcal{E}^s, \mathcal{E}^u$ and $\mathcal{E}^c$, partition the domain $\mathbb{R}^n$:

- $\mathcal{E}^s$, stable subspace, eigenvalues with negative real part,
- $\mathcal{E}^u$, unstable subspace, eigenvalues with positive real part,

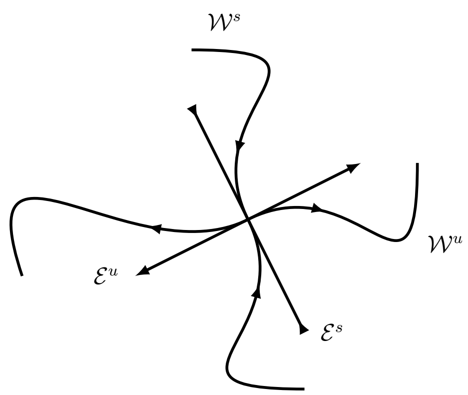

Figure 2.7: The global invariant manifolds $\mathcal{W}^u, \mathcal{W}^s$ coincide locally with the linearized versions $\mathcal{E}^u$ and $\mathcal{E}^s$. This fact can be exploited to compute the global invariant manifolds from the eigenvectors of the Jacobian of a fixed point, see Section 5.1.4.

- $\mathcal{E}^c$, center subspace, eigenvalues with zero real part.

These subspaces are invariant since solutions with initial conditions contained in a subspace, stay within this subspace for all time.

Definition 2.6 (Invariant Manifold)**.** A (k-)subspace $\mathcal{S} \subset \mathbb{R}^n$ that is locally homeomorphic to a k-dimensional Euclidean space is called manifold. The manifold $\mathcal{S}$ is called invariant under the flow of a vector field, if for all initial conditions $\mathbf{x} \in \mathcal{S}$ the trajectory through $\mathbf{x}$ remains within $\mathcal{S}$ for all integration times t, i.e., the $\mathcal{S}$ is tangent to the vector field and is thereby a stream surface.

A hyperbolic point is a fixed point $\mathbf{x}_e$ where the Jacobian matrix $\mathbf{J}_u(\mathbf{x}_e)$ has no eigenvalue with zero real part, i.e., the linearized system has no center subspace, but both stable and unstable subspaces exist. In this case, solutions with initial conditions in $\mathcal{E}^s$ converge to $\mathbf{x}_e$ as $t \to +\infty$ and solutions with initial conditions in $\mathcal{E}^u$ approach $\mathbf{x}_e$ as $t \to -\infty$. Invariant manifolds $\mathcal{E}^s$ and $\mathcal{E}^u$ of the linearized system are tangent to the invariant manifolds $\mathcal{W}^s$ and $\mathcal{W}^u$ of the non-linear system, compare Figure 2.7. These invariant manifolds, given within a small neighborhood of $\mathbf{x}_e$ where the linear term of the Taylor expansion dominates, can be extended to global invariant manifolds using the flow of the vector field, i.e., integrating a tangent curve with initial conditions on the invariant manifolds $\mathcal{E}^s$ and $\mathcal{E}^u$ of the linear system. These properties are later exploited to compute the global invariant manifolds using the eigenvectors of matrix $\mathbf{J}_{\mathbf{x}_e}$.

2.7 Stability of Trajectories of Time-Dependent Systems

For general non-autonomous systems, the stability of a solution trajectory $\mathbf{x}(t)$ cannot not be inferred from the eigenvalues of the Jacobian $\mathbf{J}(\mathbf{x}(t))$. Following the

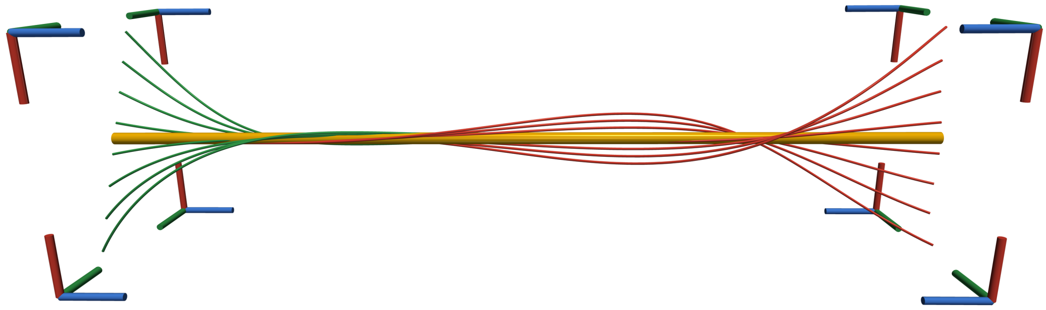

Figure 2.8: Stable (green) and unstable (red) solutions of Equation (2.24) in the space-time domain, where time increases to the right. The trivial solution $\mathbf{y}_0 = \mathbf{0}$ is shown in yellow. In contrast to the instantaneous stability analysis, which would indicate stability of $\mathbf{y}_0$, we can see from the diverging behavior of solutions (red) nearby, that the trivial solution cannot be stable.

example from Hale [Hal80], the Markus-Yamabe equation illustrates this fact. Consider the time-periodic linear vector field

$$\begin{pmatrix} \dot{x_1} \\ x_2 \end{pmatrix} = A(t) \begin{pmatrix} x_1 \\ x_3 \end{pmatrix}, \tag{2.23}$$

with

$$A(t) = \begin{pmatrix} -1 + \frac{3}{2}\cos^2(t) & 1 - \frac{3}{2}\cos(t)\sin(t) \\ -1 - \frac{3}{2}\cos(t)\sin(t) & -1 + \frac{3}{2}\sin^2(t) \end{pmatrix}. \tag{2.24}$$

The eigenvalues of $A(t)$ are independent of t and both have negative real part $\lambda_i = \frac{1}{4}(-1 \pm i\sqrt{7})$. Theorem 2.4 might suggest stability of the solution $\mathbf{y} = (0,0)^{\mathrm{T}}$. However, as it turns out, there are two linearly independent solutions, namely

$$\mathbf{y}_1(t) = \begin{pmatrix} -\cos(t) \\ \sin(t) \end{pmatrix} e^{(\frac{t}{2})}, \quad \mathbf{y}_2(t) = \begin{pmatrix} \sin(t) \\ \cos(t) \end{pmatrix} e^{(-t)}, \tag{2.25}$$

which give rise to solutions of the form $\mathbf{y}'_{1,2} = c \cdot \mathbf{y}_{1,2}$ for $c \in \mathbb{R}$. Even solutions $\mathbf{y}'_{1,2}$ starting arbitrarily close to $\mathbf{y}$ diverge rather than converge toward it. Hence, $\mathbf{y}$ is unstable which is not clear from the eigenvalues of $A(t)$. Figure 2.8 shows stable (green) and unstable (red) solutions, compare Wiggins [Wig03, Example 1.2.1].

2.8 Eulerian and Lagrangian View

The concepts introduced up until this point—fixed points and stationary points—are describing a dynamical system from an Eulerian view, i.e., observe a specific location in space and the flow passing through over time. One may interpret this as sitting on a bench overlooking the flow of a river. This flow is described by $\mathbf{u}(\mathbf{x}, t)$. The Lagrangian view, in contrast, can be seen as traveling on a boat with the flow of the river. Where the individual particle is described by $\mathcal{L}(\mathbf{x}_0, t)$. More precisely, we look at individual particles within the flow, i.e., travel with them being advected along a pathline. Both carry the same information and they relate as follows:

$$\mathbf{u}(\mathcal{L}(\mathbf{x}_0, t; t), t) = \frac{\partial \mathcal{L}}{\partial t}(\mathbf{x}, t_0; t) \tag{2.26}$$

In fluid dynamics Eulerian methods typically work on a fixed mesh of the domain, while Lagrangian methods feature particles moving along the vector field. We are mostly interested in features moving with the flow, such as vortices and streaklines. Hence, the Lagrangian view is the natural representation to use. In the autonomous case both views coincide. For example, in the setady case vortices are special types of fixed points and flow transport is described by invariant manifolds. Hence, we now turn to non-autonomous dynamical systems.

2.9 Lagrangian Coherent Structures

Since non-autonomous (time-dependent) systems have no stable and unstable manifolds tied to fixed points, one searches for new concepts with domain separating qualities. Lagrangian Coherent Structures (LCS) are just constructs that separate the flow into regions of qualitatively different behavior. Consider a non-autonomous dynamical system given by its vector field $\mathbf{u}(\mathbf{x}, t)$, where $(\mathbf{x}, t) \in \mathbb{R}^n \times \mathbb{R}$, with its corresponding flow $\Psi_{t,t_0}(\mathbf{x})$. A line or surface of initial particle locations $\mathcal{M}(t_0) \in \mathbb{R}^n$ which is advected with the flow $\mathcal{M}(t) = \Psi_{t,t_0}(\mathcal{M}(t_0))$ is called material line or material surface. Since solutions starting within $\mathcal{M}(t)$ at time t by definition remain within $\mathcal{M}(t)$, every material surface gives rise to an invariant manifold $\bigcup_t(\mathcal{M}(t))$. All of these invariant manifolds separate the flow in some sense. However, only material surfaces that have the highest impact on the overall dynamics of the system are of interest. Such manifolds are called Lagrangian coherent structures. The impact of a solution on the system is measured by its impact on nearby solutions.

2.10 The Finite-Time Lyapunov Exponent

A measure for the growth of infinitesimally perturbations in the initial conditions are the Lyapunov exponents. We note that for an n-dimensional vector field $\mathbf{u}(\mathbf{x}, t)$ each solution has n Lyapunov exponents (LE), where the largest Lyapunov exponent $\sigma_{t_0}^{\infty}(\mathbf{x})$ measures the largest possible divergence of a second trajectory starting

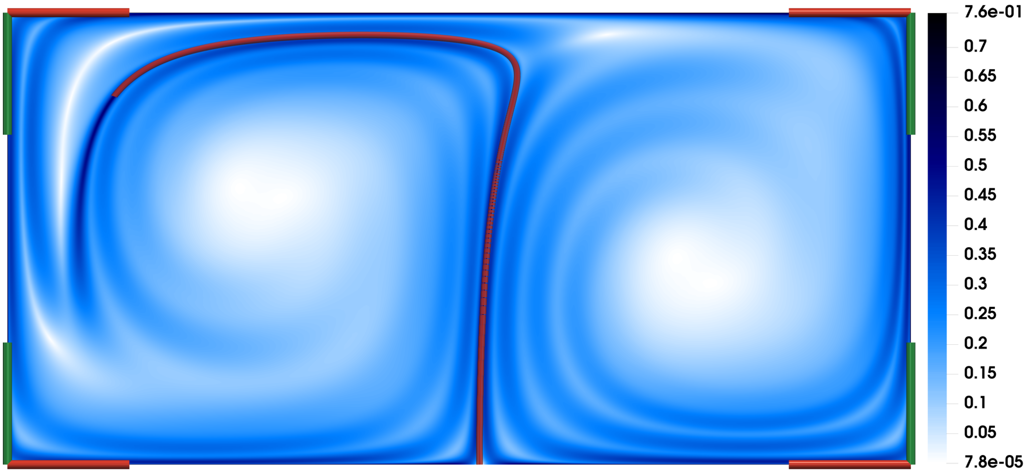

Figure 2.9: Finite-time Lyapunov exponent (FTLE) of the Double Gyre model by Shadden et al. [SLM05]. With initial time $t_0 = 0$ and advection time $T = 10s$. The FTLE ridge in the middle is clearly visible and partitions the domain and may be extracted (red tube) by the means of height ridges.

infinitesimal close to the original one. For a general dynamical system, the largest Lyapunov exponent is defined as

$$\sigma_{t_0}^{\infty}(\mathbf{x}) = \lim_{T\to\infty} \lim_{\|\delta(t_0)\to 0\|} \frac{1}{|T|} \ln(\frac{\|\delta(t_0+T)\|}{\|\delta(t_0)\|}), \tag{2.27}$$

where δ measures the perturbation at time t and maximizes the quantity $\sigma_{t_0}^{\infty}(\mathbf{x})$. In the case of non-autonomous dynamical systems, the maximum Lyapunov exponent is commonly approximated by considering the separation after a finite advection time T, called finite-time Lyapunov exponent (FTLE),

$$\sigma_{t_0}^{\mathrm{T}}(\mathbf{x}) = \lim_{\|\delta(t_0)\to 0\|} \frac{1}{|T|} \ln(\frac{\|\delta(t_0+T)\|}{\|\delta(t_0)\|}). \tag{2.28}$$

Haller [Hal01] shows that Equation (2.28) can be more efficiently computed by means of the flow map $\Psi_{t_0+T,t_0}(\mathbf{x})$, where the direction of maximum growth of perturbation is given by the eigenvector corresponding to $\lambda_{\max}$ of the Cauchy-Green tensor

$$C_{t_0}^{\mathrm{T}} = (\nabla\Psi_{t_0+T,t_0}(\mathbf{x}))^{\mathrm{T}} \cdot \nabla\Psi_{t_0+T,t_0}(\mathbf{x}), \tag{2.29}$$

and the maximum stretching is determined by the largest eigenvalue

$$\sigma_{t_0}^{\mathrm{T}}(\mathbf{x}) = \frac{1}{T} \log\left(\sqrt{\lambda_{\max}(\mathbf{x})}\right). \tag{2.30}$$

Note that this is a measure defined on a trajectory basis, i.e., for a fixed start time t_0 each point $\mathbf{x} \in \mathbb{R}$ uniquely identifies a pathline. This directly implies that for the computation of LCS one needs to compute the flow map $\Psi_{t_0+T,t_0}(\mathbf{x})$ for the entire domain (or of a sampled version). The initial particle locations $\mathcal{M}(t_0)$ of a Lagrangian coherent structure can be extracted by ridges and valleys of the scalar indicator field $\sigma_{t_0}^{\mathrm{T}}(\mathbf{x})$. Figure 2.9 shows a numerically computed FTLE field for the Double Gyre model from Shadden et al. [SLM05], which is described in detail in Section 8.1.3. Ridges and valleys are structures of codimension one representing local maxima and minima in all but one direction. Although FTLE ridges are commonly used to extract LCS, Shadden et al. [SLM05] showed that only ridges with negligible cross-flow coincide with LCS. Some of the shortcomings have been addressed by various authors [BR10; FSP12; Guo*16; Hal11; Hal15; HS11; TCH11]. We refer to Heine et al. [Hei*16] for a comprehensive overview.

2.10.1 Height Ridges

Definition 2.7 (Ridge)**.** Let $f : \mathbb{R}^n \to \mathbb{R}$ be an n-dimensional scalar field, then a ridge is a set of points $\mathbf{x} \in \mathbb{R}^n$, where f is a local maximum in at least one direction. Ridges are d-manifolds where f has a local maximum in $n - d$ directions.

There exist a multitude of different definitions [Har83; Lin98; SV52] for ridges. However, we follow Eberlys' height ridges [Ebe*94]. The definition is founded on eigenvalues of the Hessian of f, which is the matrix $\mathbf{H}_f$ of second-order partial derivatives. We can interpret $\mathbf{H}_f$ as the Jacobian of the gradient vector field ∇f

$$\nabla f(\mathbf{x}) = \left(\frac{\partial f(\mathbf{x})}{\partial x_1}, \cdots, \frac{\partial f(\mathbf{x})}{\partial x_n}\right)^{\mathrm{T}}, \quad \mathbf{H}_f = \mathbf{J}_{\nabla f}^{\mathrm{T}}(\mathbf{x}). \tag{2.31}$$

Consider the descendingly sorted eigenvalues λ_i with corresponding eigenvectors $\mathbf{e}_i$ of the Hessian, then a point $\mathbf{x}$ lies on a d-dimensional height ride, if for $j = d+1, \cdots, n$,

$$\mathbf{e}_j \cdot \nabla f = 0, \quad \lambda_j < 0. \tag{2.32}$$

The first part of Equation (2.32) is an isosurface and may be extracted by the marching cubes [LC87] or marching tetrahedra algorithm [DK91]. However, this requires consistently oriented eigenvectors of the Hessian, which is typically done using principal component analysis [FP01; JC16]. The first part can be reformulated to a parallel vectors condition

$$\mathbf{e}_j \parallel \nabla f. \tag{2.33}$$

This formulation requires explicit computation of the eigenvectors of the Hessian $\mathbf{H}_\mathbf{J}$, which can lead to significant accumulation of numerical errors. This can be mitigated by the use of an implicit formulation $\mathbf{H}_f \nabla f \parallel \nabla f$, where the calculation of $\mathbf{e}_j$ is not necessary. Such formulations using the parallelism of two vector fields are commonly employed to find solutions using the parallel vectors (PV) operator, as introduced in Section 4.2.1.

In the aforementioned case of ridges of the FTLE field (see Figure 2.9), additional filtering might be required since numerical computation of second-order derivatives can amplify numerical errors [SP09]. With this definition, valleys of the original field f can be found by extracting ridges of the negative field, i.e., $-f$.

2.11 Hyperbolic Trajectories

Hyperbolic regions within a flow field are isolating neighborhoods [Hal00] along which particles traveling with the flow are separated. In order to truly separate particles within the flow, these regions need to advect with the flow. Hence, we can characterize this by the behavior of a trajectory (pathline) moving with the region. According to Haller only trajectories that are locally for the longest time hyperbolic, are hyperbolic trajectories. The correct mathematical notion for hyperbolic trajectories is the one of an exponential dichotomy. This classifies a trajectory $\mathbf{x}(t)$ of the time-dependent vector field $\mathbf{u}$ as hyperbolic if the linearized system

$$\dot{\mathbf{y}} = \mathbf{J}_{\mathbf{u}}(\mathbf{x}(t), t)\mathbf{y}, \tag{2.34}$$

of the trajectory has an exponential dichotomy. A precise description of these notions is given by Mancho et al. [Man*03] and further information by Wiggins [Wig03].

For our application the physical interpretation of these phenomena shall suffice. These notions were coined by Haller [Hal00] for the two-dimensional case and later extended to the three-dimensional case [Hal01]. We give a brief introduction to the 2D case. According to Haller instantaneous hyperbolicity can be measured by a strictly negative determinant of the Jacobian $\det \mathbf{J}_{\mathbf{u}}(\mathbf{x}, t) < 0$. This implies two real eigenvalues of opposite sign of the Jacobian at the point $\mathbf{x}$, i.e., $\lambda_1 < 0, \lambda_2 > 0$. This notion can be used as a scalar indicator field for hyperbolicity within a time-dependent flow field by considering this indicator field over a period of time $[t_0, t_0{+}T]$

$$I_T(\mathbf{x}_0) = \max_{t\in[t_0,t_0+T]} \{t : \det \mathbf{J}_{\mathbf{u}}(\mathbf{x}, \tau) < 0, \quad t_0 \leq \tau \leq t\}. \tag{2.35}$$

Haller calls this property hyperbolicity time with mhe minimal eigenvalues of $\mathbf{J}_{\mathbf{u}}$

$$\lambda_1^{\min} = \min_{t\in[t_0,t_0+T]} \lambda_1(t), \qquad \lambda_2^{\min} = \min_{t\in[t_0,t_0+T]} \lambda_2(t). \tag{2.36}$$

Consider the smoothly oriented unit eigenvectors $\mathbf{e}_1(t), \mathbf{e}_2(t)$ corresponding to the eigenvalues $-\lambda_1(t), \lambda_2(t)$, and the angle between them denoted by $\kappa(t)$ and the matrix $M(t) = (\mathbf{e}_1(t), \mathbf{e}_2(t))$. Then Haller defines the following invariant quantities

$$\begin{aligned} \alpha = \min_{t\in[t_0,t_0+T]} |\sin(\kappa(t))| &= \frac{1}{\sqrt{(2)}} \max_{t\in[t_0,t_0+T]} \left\| M^{-1}(t) \right\|_F, \\ \beta &= \frac{1}{\sqrt{(2)}} \max_{t\in[t_0,t_0+T]} \left\| \dot{M}(t) \right\|_F, \end{aligned} \tag{2.37}$$

where $\|A\|_F = \sqrt{\sum |A_{ij}|^2}$ denotes the Frobenius norm. With these notions Haller [Hal00] defines sufficient criteria for hyperbolicity and uniform finite-time hyperbolicity, i.e., the existence of finite-time stable and unstable manifolds,

$$\sqrt{2}\beta\left[\frac{1}{\lambda_1^{\min}} + \frac{1}{\lambda_2^{\min}}\right] < \alpha. \tag{2.38}$$

Haller describes this by the facts that the Lagrangian and Eulerian time scales along the trajectory $\mathbf{x}(t)$ captured by α and β are sufficiently separated. Meaning, the relative motion of coherent structures is slower than that of typical particles.

The motivation, behind this is that in general the local hyperbolicity (Equation (2.34)) cannot be used to characterize time-dependent hyperbolicity. However, the counterexamples in literature all achieve this by rapidly changing the eigenvectors of the Jacobian $\mathbf{J_u}$, and Equation (2.38) ensures that these conditions cannot be present. Furthermore, the permitted ratio of α and β can be lower the higher the instantaneous hyperbolicity is. This means, that if in addition to instantaneous hyperbolicity $\det \mathbf{J_u}(\mathbf{x}, t) < 0$, Equation (2.38) holds, hyperbolicity of a trajectory may be characterized by the instantaneous hyperbolicity. Haller further proves that if the velocity of the coherent structures is below a certain limit, instantaneous hyperbolicity alone can be used to study a hyperbolic trajectory and thereby giving a necessary condition for hyperbolic trajectories.

The author goes on to extract the most relevant hyperbolic structures [Hal01], which they define as the trajectories that exhibit hyperbolic behavior for the longest time, i.e., maxima in the hyperbolicity time indicator field. Or in other words, trajectories from which other trajectories diverge, in both forward and backward time. These most relevant structures define Lagrangian coherent structures (LCS). The separating characteristics of hyperbolic trajectories are especially useful for the exploration of time-dependent vector field topology, discussed in Section 5.2.

2.12 Divergence and Curl

Divergence and curl capture two essential properties of vector fields, 1) local in and outflow around a point, and 2) local corresponding angular motion:

$$\operatorname{div}(\mathbf{u}(\mathbf{x},t)) = \nabla \cdot \mathbf{u}(\mathbf{x}) = \operatorname{trace}(\nabla \mathbf{u}(\mathbf{x})) = \lim_{V \to \mathbf{0}} \frac{1}{V} \int_{\partial V} \mathbf{u} \times \hat{\mathbf{n}} \, \mathrm{d}S, \tag{2.39}$$

$$\operatorname{curl}(\mathbf{u}(\mathbf{x},t)) = \boldsymbol{\omega}(\mathbf{u}(\mathbf{x},t)) = \nabla \times \mathbf{u}(\mathbf{x},t) = \lim_{V \to \mathbf{0}} \frac{1}{V} \int_{\partial V} \mathbf{u} \cdot \hat{\mathbf{n}} \, \mathrm{d}S. \tag{2.40}$$

The divergence captures the net outflow at a point $\mathbf{x}$, i.e., positive divergence indicates net outflow and negative net inflow, c.f. Figure 2.10a. The curl is a vector valued measure of the local rotation, where the direction represents the axis of rotation and magnitude indicates rotational strength. A vector field representing velocity is called velocity field and its curl is commonly referred to as vorticity. The angular velocity of the flow infinitesimally close around a point $\mathbf{x}$ is given by $\frac{1}{2}\|\boldsymbol{\omega}\|$.

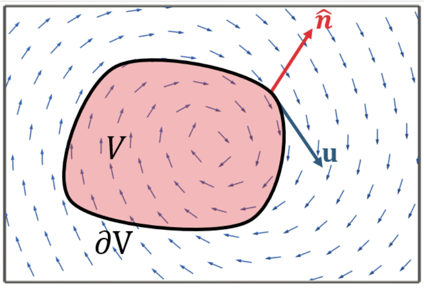

(a) Curl/Divergence

(b) Linked Vortex Lines

Figure 2.10: Construction of curl and divergence as the integral over the surface of a shrinking volume (a). Two linked vortex lines with Gaussian linking number -4, which illustrates the meaning of helicity (b) [Che*17].

Note that the curl is divergence-free, and the gradient is curl-free, implying that any conservative vector field, i.e., the gradient field of a scalar field, is curl free. Further, in the special case of a vector field on $\mathbb{R}^3$, there exists a unique decomposition into a divergence-free and curl-free component, this is sometimes referred to as the Helmholtz's theorem [Hel58]. Since the curl of a vector field is again a vector field, one may think of characteristic curves of the vorticity field. Typically, streamlines of the vorticity field are called vortex lines.

2.12.1 Helicity

The interplay of vortex lines is captured by helicity, which represents the winding of vortex lines around each other (see Figure 2.10b)The helicity within a region V of a vorticity field $\boldsymbol{\omega}$ is given with the aid of a vector potential $\mathbf{u}$ where $\mathrm{curl}(\mathbf{u}) = \boldsymbol{\omega}$

$$H(\boldsymbol{\omega}) := \int_V \mathbf{u} \cdot \boldsymbol{\omega} \,\mathrm{d}V. \tag{2.41}$$

Helicity of a vector field $\mathbf{u}$ is defined as above, where $\boldsymbol{\omega} = \nabla \times \mathbf{u}$ is the curl. Within the flow visualization community helicity is also known as the local property $h(\mathbf{u}) := \mathbf{u} \cdot (\nabla \times \mathbf{u})$. For the remainder of this thesis, we refer to the first (global) definition.

2.13 Matrix Decompositions

There exist a variety of matrix decompositions important for flow visualization and analysis. They are commonly used by vortex detectors or ridge criteria. We shortly introduce matrix decompositions used within this thesis.

2.13.1 Symmetric and Antisymmetric Part

A Matrix M can be decomposed into a symmetric $\mathbf{S}$ and antisymmetric part $\mathbf{\Omega}$:

$$\mathbf{S} = \frac{M + M^{\mathrm{T}}}{2}, \quad \mathbf{\Omega} = \frac{M - M^{\mathrm{T}}}{2}, \tag{2.42}$$

with $M = \mathbf{S} + \mathbf{\Omega}$. When M is the Jacobian $\mathbf{J}$ of a velocity field, $\mathbf{S}$ is called the strain rate tensor and $\mathbf{\Omega}$ the vorticity tensor. The strain rate tensor $\mathbf{S}$ captures the locate rate of change of deformation within the vector field. The vorticity tensor $\mathbf{\Omega}$, on the other hand, measures the local rotation and is closely related to vorticity [Sad10].

2.13.2 Helmholtz-Hodge Decomposition

The Helmholtz-Hodge decomposition (HHD) decomposes a vector field into a scalar potential, which is curl-free (Section 2.12), a vector potential, which is divergence free, and a harmonic part, which is an irrational/conservative vector field, i.e., a gradient vector field. Bhatia et al. [Bha*13] give an detailed overview of the topic. The terminology is based on Bhatia et al. [Bha*13] and Chorin et al. [CMM90].

Theorem 2.8. A vector field $\mathbf{u}$ can by uniquely decomposed into three components. 1) an irrational (curl-free) component $\mathbf{d}$, 2) an incompressible (divergence-free) component $\mathbf{r}$, and, 3) a harmonic (curl-free and divergence-free) component $\mathbf{h}$.

$$\mathbf{u} = \nabla D + \nabla \times \mathbf{R} + \mathbf{h} \tag{2.43}$$

$$= \mathbf{d} + \mathbf{r} + \mathbf{h}. \tag{2.44}$$

The harmonic part can be integrated into either the curl-free $\mathbf{d}$ or divergence-free part $\mathbf{r}$. However, to make the decomposition unique, it is extracted into its own component $\mathbf{h}$. Thereby this decomposition characterizes the original vector field $\mathbf{u}$

$$\nabla \cdot \mathbf{d} = \nabla \cdot \mathbf{u}, \quad \text{and} \quad \nabla \times \mathbf{r} = \nabla \times \mathbf{u}. \tag{2.45}$$

3 Frames of Reference

The frame of reference consists of a set of criteria to which relative measurements can be made. Consider a train moving with constant velocity on a railway. From the outside the train appears to move in a specific direction. However, for passengers on the train, the outside world appears to be moving and the train itself itself appears steady. Furthermore, an astronaut on the international space station, not only registers the motion of the train along the railway but also the rotation of the railway with the earth and the rotation around the sun. Of course, the physics do not change depending on the observer, further, the principle of relativity states that the laws of physics have the same form in all inertial frames of reference. This is also true for special and general relativity. However, our perception of certain phenomena do depend on the chosen frame of reference. For example, we recognize the rotation of a playing vinyl record, but now imagine standing on the record itself and looking downward. There is no relative motion between us (the observer) and the turning record. This fact, that any perceived motion is relative to some observer, poses a fundamental challenge in flow visualization. Consider some basic properties of a flow field, such as characteristic curves or even the steadiness of the flow itself. These properties are directly influenced by perspective of the observer. A flow field may appear steady for some observers, but seems to be unsteady for another observer moving relative to the flow. While all frames of reference are equal, i.e., carry equivalent information, feature extraction techniques, like vortex extractors, highly depend on the specific frame of reference and are not invariant under certain observer transformations, i.e., the position of a detected vortex changes depending on the frame of reference, or the vortex might not be detected at all. Therefore, the invariance of feature extraction techniques with respect to certain classes of observer transformations is highly desireable. Recent advances in invariant formulation of vortex measures separate observer transformation into four different classes, namely 1) Galilean, 2) rotation, 3) rigid body, and 4) affine transformations. In this chapter, we introduce each of these four classes in detail. Their impact on the extraction of certain flow features, most prominently vortices, is covered in Chapter 4.

3.1 Translation between Frames of Reference

By a transformation of the observer, or frame of reference, we mean a transformation of the domain that maps a point $\mathbf{x}$ at time t to another point $\mathbf{x}^*$ at time t^* [GST16;

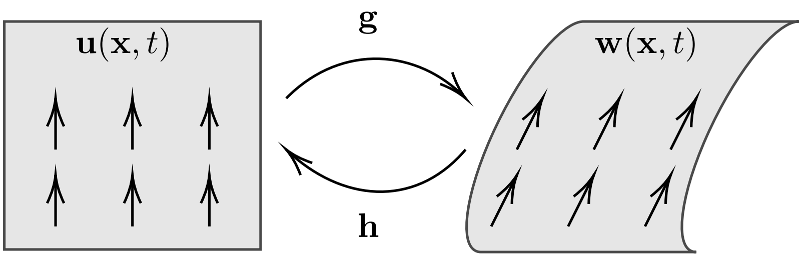

Figure 3.1: Transformation $\mathbf{g}$ and back transformation $\mathbf{h}$ of the original vector field $\mathbf{u}(\mathbf{x}, t)$, and its domain, to another vector field $\mathbf{w}(\mathbf{x}, t)$.

TN04]. Consider a non-autonomous dynamical system and its vector field $\mathbf{u} : \mathbb{R}^n \times \mathbb{R} \to \mathbb{R}^n$, then a domain transformation is a differential map

$$\begin{aligned} \mathbf{g} : \mathbb{R}^n \times \mathbb{R} &\to \mathbb{R}^n, \\ (\mathbf{x}, t) &\mapsto \mathbf{x}^*, \end{aligned} \tag{3.1}$$

with a uniform inverse $\mathbf{h} : \mathbb{R}^n \times \mathbb{R} \to \mathbb{R}^n$ where

$$\mathbf{h}(\mathbf{g}(\mathbf{x}, t), t^*) = \mathbf{g}(\mathbf{h}(\mathbf{x}^*, t^*), t) \tag{3.2}$$

holds for all $(\mathbf{x}^*, t^*) \in \mathbb{R}^n \times \mathbb{R}$. With this transformation, a new vector field $\mathbf{w}(\mathbf{x}^*, t^*)$ on $\mathbf{g}(\mathbb{R}^n)$ can be defined, that maps pathlines of $\mathbf{u}$ to pathlines of $\mathbf{w}$. This uniquely defines a new vector field $\mathbf{w}$ [Kuh*12]

$$\mathbf{w}(\mathbf{x}^*, t^*) = (\nabla \mathbf{h}(\mathbf{x}^*, t^*))^{-1} (\mathbf{u}(\mathbf{h}(\mathbf{x}^*, t^*), t) - \mathbf{h}_t(\mathbf{x}^*, t^*)), \tag{3.3}$$

where $\nabla \mathbf{h}$ is the spatial gradient of $\mathbf{h}$ and $\mathbf{h}_t$ its time derivative. By construction (Equation (3.2)) this transformation can be inverted

$$\mathbf{u}(\mathbf{x}, t) = (\nabla \mathbf{g}(\mathbf{x}, t))^{-1} (\mathbf{w}(\mathbf{g}(\mathbf{x}, t), t^*) - \mathbf{g}_t(\mathbf{x}, t)). \tag{3.4}$$

Figure 3.1 illustrates the role of $\mathbf{g}$ and its inverse $\mathbf{h}$.

3.2 Classes of Observer Motion

In the following, we distinguish classes of observer motion and types of invariance related to each class. A general transformation has the form

$$\mathbf{g}(\mathbf{x}, t) = R(t)\mathbf{x} + \mathbf{c}(t), \quad t^* = t + c \tag{3.5}$$

where $R(t)$ is a general time-dependent invertible matrix, $\mathbf{c}(t)$ is a time-dependent translation vector, possibly including a constant, and $c \in \mathbb{R}$ is a constant.

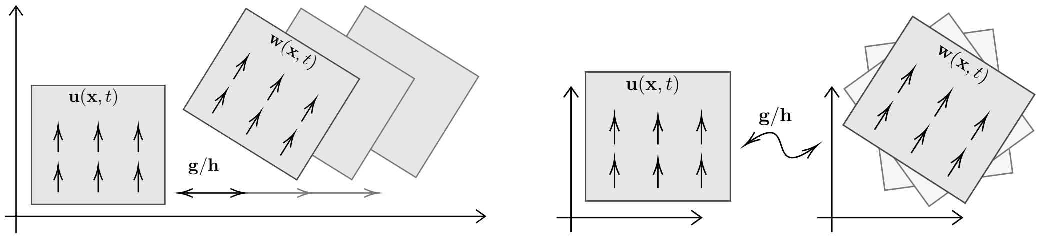

(a) Galilean Transformation (b) Rigid Body Rotation

Figure 3.2: Galilean transformation of the domain of $\mathbf{u}(\mathbf{x}, t)$. Constant rotation and continuous time-dependent translation (a), and continuous rigid body rotation (b).

A scalar-,vector-, or tensor is invariant under a domain transformation if

- a scalar remains unchanged,
- a vector $\mathbf{r}$ is transformed to $\mathbf{r}^* = R(t)\mathbf{r}$,
- a second-order tensor $\mathbf{T}$ is transformed to $\mathbf{T}^* = R(t)\mathbf{T}R(t)^{-1}$.

The four classes of observer motion and invariance respectively impose restrictions on the translation vector $\mathbf{c}(t)$ and the transformation matrix $R(t)$.

3.2.1 Galilean Invariance

A Galilean transformation has the form

$$\mathbf{g}(\mathbf{x}, t) = Q\mathbf{x} + t\mathbf{c} + \mathbf{c}_0, \tag{3.6}$$

where $Q \in \mathrm{SO}(n)$ is a constant rotation matrix, and $t\mathbf{c}$ a linear translation vector and $\mathbf{c}_0$ a constant point (Figure 3.2a). The vector field itself is not Galilean invariant

$$\mathbf{u}^*(\mathbf{x}^*, t^*) = \frac{\mathrm{d}\mathbf{x}^*}{\mathrm{d}t} = \frac{\mathrm{d}\mathbf{x}^*}{\mathrm{d}t}\frac{\mathrm{d}t}{\mathrm{d}t^*} = \frac{\mathrm{d}\mathbf{x}^*}{\mathrm{d}t} = R(t)\frac{\mathrm{d}\mathbf{x}}{\mathrm{d}t^*} + \mathbf{c} = R(t)\mathbf{u}(\mathbf{x}, t) + \mathbf{c}, \tag{3.7}$$

Derivatives of the vector field—like the Jacobian—on the other hand, are Galilean invariant. Hence, almost any measures based on pathlines is Galilean invariant [GGT17], including the flow map Ψ and the FTLE.

3.2.2 Rotation Invariance

A rotational transformation of the domain has the form

$$\mathbf{g}(\mathbf{x}, t) = Q(t)\mathbf{x} + \mathbf{c}_0, \tag{3.8}$$

where $Q \in \mathrm{SO}(n)$ is a time-dependent rotation matrix, and $\mathbf{c}_0$ a constant point, c.f. Figure 3.2b. Rotation invariant measures typically use a translation to polar

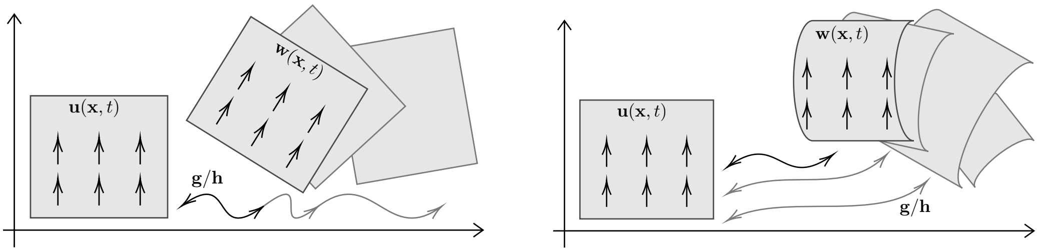

(a) Rigid Body Transformation (b) Affine Transformation

Figure 3.3: Rigid body transformation of the domain of $\mathbf{u}(\mathbf{x}, t)$, i.e., continuous rotation and translation (a), and time-dependent affine transformation. This includes shearing, scaling and general deformation of the domain (b).

coordinates to decouple extraction techniques from rotational influences [GST16]. The importance of rotational invariance is rather small. However, it is a key part on the road to objective measures, i.e., invariance under rigid body motion.

3.2.3 Objectivity

The term objectivity denotes the invariance under rigid body motion, i.e., smooth rotation and translation (Figure 3.3a)

$$\mathbf{g}(\mathbf{x}, t) = Q(t)\mathbf{x} + \mathbf{c}(t), \tag{3.9}$$

where $Q \in \mathrm{SO}(n)$ is a time-dependent rotation matrix, and $\mathbf{c}(t)$ is a time-dependent translation vector. This type of motion is usually associated with a typical observer, conserving shape, i.e., no deformation occurs (Figure 3.3a). Mathematically, transformations of this type, Galilean and rotational transformations as subclasses, are isometries, i.e., they preserve distances.

There exist only few differential objective properties [GGT17; Hal05] of a vector field. The strain rate tensor $\mathbf{S}$, the symmetric part of the Jacobian of the vector field, being one of them. In contrast, the vorticity tensor $\mathbf{\Omega}$ is Galilean invariant but not objective [DL76]. An objective version of $\mathbf{\Omega}$ was presented by Drouot and Lucius [DL76], and Tabor and Klapper [TK94].

3.2.4 Hyperobjectivity

General invertible domain transformations, i.e., affine transformations, are hard to relate to observer relative motion. For example, they include scaling, stretching and shearing of the domain. These transformations become important when multiple observers are at play. This is discussed in detail in Chapter 6. hyperobjective measures are invariant under affine transformations

$$\mathbf{g}(\mathbf{x}, t) = R(t)\mathbf{x} + \mathbf{c}(t), \tag{3.10}$$

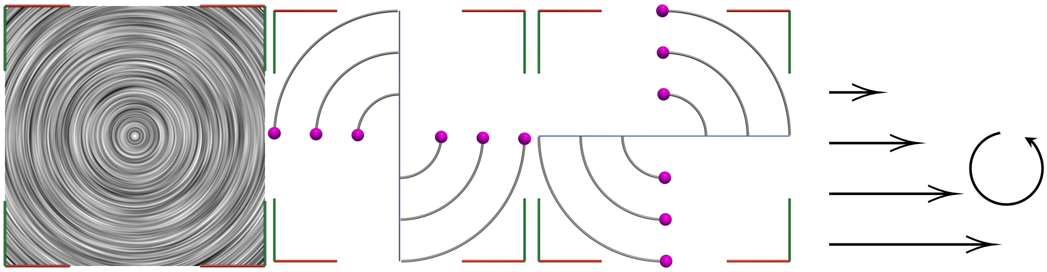

(a) Observer Field $\mathbf{v}$ (b) Observer world lines (c) Observer world lines (d) Induced Rotation

Figure 3.4: Line integral convolution (LIC) of an observer velocity field representing rigid body rotation (a). Observer world lines of the same observer velocity field with different observation times r ((b) and (c)). Both (b) and (c) correspond to a rotation of 90°, but the final location of the observers depend on the observation time, i.e., their starting location at time r represented by the blue lines. Rotation of the original domain is represented by relative observer motion (d).

where R is a general time-dependent invertible matrix and $\mathbf{c}(t)$ a time-dependent translation vector. Transformations of this class no longer preserve distances, c.f. Figure 3.3b. This is the most general class of transformations, it preserves only basic properties, such as the ratio of segments.

One may further think about transformations which also allow $R(t)$ to be non-invertible. However, such transformations include mapping the entire domain to a line or point. In general information is lost under these maps. Therefore, the only classes of transformations we explore are the four mentioned in this chapter.

3.3 Modeling Observer Motion as a Vector Field

For the translation between frames of reference, as it is described by Equation (3.3), one requires an analytical representation of the domain transformation $\mathbf{g}(\mathbf{x}, t)$. However, in practice observer motion is often modeled as a time-dependent vector field, where tangent curves represent the paths of the observer. This means, Equation (3.5) has to be represented in form of an observer flow field, i.e., both translation and rotation have to be encoded. Let $\mathbf{u}(\mathbf{x}, t)$ be an n-dimensional vector field seen through the eyes of some observer $\mathcal{O}$, where the motion of the observer, as defined by Equation (3.5), is modeled by the observer velocity field $\mathbf{v}_{\mathcal{O}}(\mathbf{x}, t)$, sometimes just called observer field. Pathlines of the observer velocity field take the place of the time-dependent translation vector $\mathbf{c}(t)$. We call these pathlines observer world lines. The domain deformation matrix $R(t)$ is defined by relative motion of observer world lines. For the construction of the observer velocity field, consider a pathline through the point $\mathbf{x} \in \mathbb{R}^n$ at a time r, obtained by the flow map with varying parameter t

$$\mathcal{L}_{\mathcal{O}}(\mathbf{x}, r; t) = \Psi^{\mathbf{v}}_{t,r}(\mathbf{x}) = \mathbf{x} + \int_r^t \mathbf{v}(\mathcal{L}(\tau), \tau)\, \mathrm{d}\tau, \tag{3.11}$$

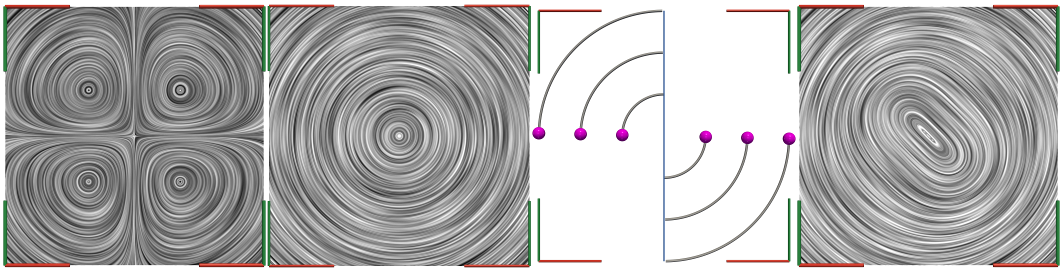

(a) Four Centers Model (b) Observer Motion (c) World Lines (d) Rotating Frame

Figure 3.5: The four centers model in the steady frame (a), observer velocity field (b) and the corresponding observer world lines (c). A snapshot at time $t = 0$ of the field in the rotating frame shows that the vortices are no longer directly visible (d).

with fixed r and $\mathbf{x}$. Since the observer field may be time-dependent, it is crucial to specify an initial point in time r. A general domain transformation, as defined by Equation (3.5), transforms a point $\mathbf{x}$ at a fixed time t to another point $\mathbf{x}^*$ at time t^*. For simplicity, we assume $t^* = t$. We refer to Hadwiger et al. [Had*19] and Günther et al. [GST16] for a more detailed derivation. It might seem natural to set $r = 0$ and simply compute the observer world line from there. However, this choice is entirely arbitrary because the observer could have been started moving previously. There are no restrictions posed on the choice of r and the resulting transformations are equally valid. A fixed observation time has to be chosen nonetheless.

$$\mathbf{x}^* = \Psi^{\mathbf{v}}_{t,r}(\mathbf{x}). \tag{3.12}$$

We can think of r as a reference to which relative measurements are made. For example, consider a continues rigid body rotation defined by a vector field (Figure 3.4a). In order to measure the rotation represented by the observers moving along the velocity field, we need some reference line which corresponds to "no rotation", i.e., the angle between the observer and the reference line (blue) is $0°$, compare Figure 3.4. In this case the choice of r corresponds to the orientation of this reference line.

The role of r will become clear when we look at the rotation and deformation part of our domain transformation. These can be thought of as the relative motion of pathlines of $\mathbf{v}$, c.f. Figure 3.5. Hence, the deformation matrix $R(t)$ is given by

$$R(t) = \nabla\Psi^{\mathbf{v}}_{t,r}(\mathbf{x}). \tag{3.13}$$

Transformation of the original vector field $\mathbf{u}$ into the new observed field $\mathbf{w}_r$ [Had*19]

$$\begin{aligned}\mathbf{w}_r(\mathbf{x},t) =& \nabla\Psi^{\mathbf{v},-1}_{t,r}\Big(\Psi^{\mathbf{v}}_{t,r}(\mathbf{x})\Big)\Big(\mathbf{u}\Big(\Psi^{\mathbf{v}}_{t,r}(\mathbf{x}),t\Big) - \mathbf{v}\Big(\Psi^{\mathbf{v}}_{t,r}(\mathbf{x}),t\Big)\Big)\\ =& \nabla\Psi^{\mathbf{v},-1}_{t,r}\Big(\Psi^{\mathbf{v}}_{t,r}(\mathbf{x})\Big)\Big(\mathbf{u}_{\mathbf{v}}\Big(\Psi^{\mathbf{v}}_{t,r}(\mathbf{x}),t\Big)\Big),\end{aligned} \tag{3.14}$$

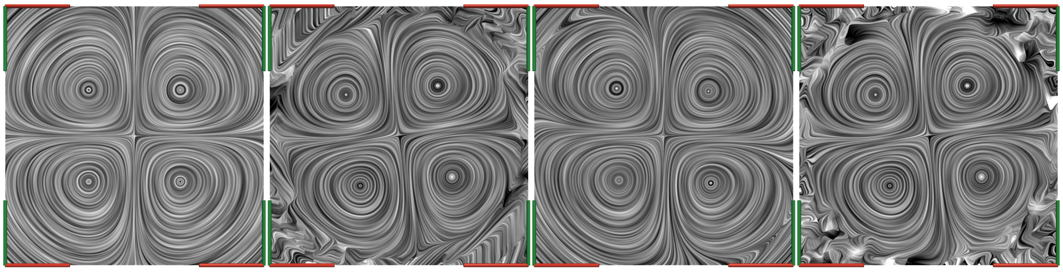

(a) Original Field (b) No-Slip Boundary (c) Clamp Boundary (d) Wrap Boundary

Figure 3.6: Ground truth, i.e., the original four centers model in the steady frame (a). Without any boundary treatment the back transformation heavily distorts the field at the outside (b). Clamping the boundary in this case results in minimal distortions (c). Wrapping the domain at the boundary also distorts the resulting field in this case because the vector field is antisymmetric at the boundaries, i.e., the direction of the field is flipped when moving from the bottom boundary to the top one. The same holds for the left and right boundary (d).

where $\mathbf{u_v}(\mathbf{x}, t) = \mathbf{u}(\mathbf{x}, t) - \mathbf{v}(\mathbf{x}, t)$. Of course general time-dependent vector fields can represent far more (local) transformations than the ones mentioned here, we will discuss these cases in Chapter 6. However, we will generally use vector fields to describe observer motion.

The formulation of observer motion as vector field decomposes the original field

$$\mathbf{u} = \mathbf{v} + \widetilde{\mathbf{w}}, \tag{3.15}$$

where $\widetilde{\mathbf{w}}$ is the representation of $\mathbf{w}$ before being translated into the new frame of reference. However, both fields $\mathbf{w}$ and $\widetilde{\mathbf{w}}$ in conjunction with the observer vector field $\mathbf{v}$ carry the same information. Thus, if feature extraction can be performed in both fields, $\widetilde{\mathbf{w}}$ might be preferable because no domain transformation is required.

A SHORT EXAMPLE As a short example we look at the four centers model as described in Section 8.1.1. The steady version is comprised of four vortices, one in each quadrant of the domain and a saddle-type critical point in the middle, see Figure 3.5a. We introduce a continuously rotating observer described by the velocity field in Figure 3.5b, and translate the model into the rotating frame. Thereby, making it time-dependent. Observer world lines of this particular case are depicted in Figure 3.4. After the transformation, the field in the resulting frame at time $t = 0$ does no longer reveal four vortices, compare Figure 3.5d. This poses difficulties for their extraction, we discuss this in detail in Chapter 4. Of course, we can simply rotate the frame back to the steady frame, by inverting the observer velocity field, i.e., swap the orientation of the vector field.

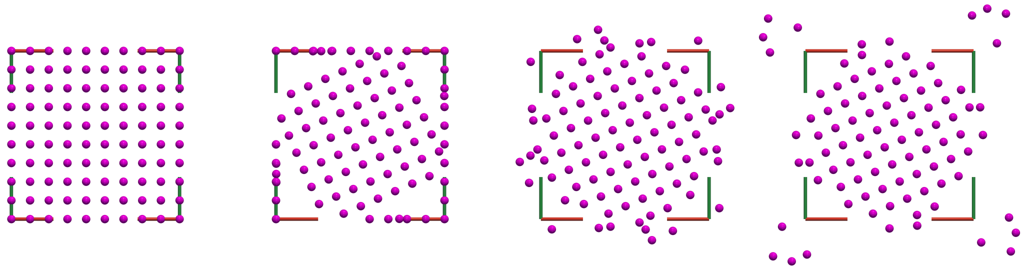

(a) Initial Positions (b) No-Slip Treatment (c) Clamp Boundary (d) Wrap Boundary

Figure 3.7: Initial positions of 100 observers (a). Positions after a rotation with respective boundary treatments, (i) no-slip (b), (ii) clamped (c), and (iii) wrapped (d).

3.3.1 Boundary Issues

In theory, the transformation of a scalar, vector, or tensor field is straightforward following the previous sections. However, in practice this means numerical computation of the flow map of the observer vector field $\mathbf{v}$. This can be problematic for a number of reasons. 1) Numerical integration of the observer field is both expensive and susceptible to accumulation of numerical errors. 2) Discrete datasets have boundaries, and hence, the integration of observer world lines may exit the domain. Since we require derivatives of the flow map of $\mathbf{v}$ these cases need to be treated to prevent discontinuities of the transformed field. The first part is a general problem of numerical integration, and we are thus only concerned with the latter.

To see why the second point poses problems, consider the four centers example from before (Figure 3.5). There we analytically transformed the model into the rotating frame of reference. If we now apply the back transformation numerically, according to Equation (3.14), the result will be distorted, see Figure 3.6. In order to mitigate these issues, we propose to employ boundary treatment. We evaluate three types of boundary treatment. Let the domain $D \subset \mathbb{R}^n$ of a vector field $\mathbf{u}(\mathbf{x})$ be defined by n closed intervals $D_i = [x_i^0, x_i^1] \subset \mathbb{R}, \quad 0 \leq i \leq n.$

1. No-slip, i.e., stop integration $x_i \notin D_i \Rightarrow u_i(x_i) = 0$.

2. Clamp: continue integrating but the value of the vector field on the domain boundary is used in each step, i.e., project the current position onto the boundary by setting the coordinates to the corresponding domain minimum or maximum. This is done separately for all coordinate components:

$$\begin{aligned} x_i < x_i^0 \Rightarrow u_i(x_i) = u_i(x_i^0), \\ x_i > x_i^1 \Rightarrow u_i(x_i) = u_i(x_i^1). \end{aligned} \tag{3.16}$$

3. Wrap: let the integration continue by wrapping the domain so that leaving it in one direction means entering on the opposite site:

$$x_i \notin D_i \Rightarrow u_i(x_i) = u_i\Big((x_i - x_i^0) \mod |x_i^1 - x_i^0|\Big). \tag{3.17}$$

A no-slip boundary is problematic, since the required derivatives of the flow map degenerate when multiple observers get stuck in the boundary, see Figures 3.6b and 3.7b. A conservative approach is clamping the boundary. This way integration does not stop of the domain boundary and continues with a similar direction. Clamping is done for each component individually. Hence, observers that leave the domain can still move along similar paths as observers within the domain. Figures 3.6c and 3.7c show that this results in slight distortion in the transformed frame. However, considering that this can adopt well to general domains, clamping of the frame of reference is a sensible default to improve the transformation. For periodic domains, the wrap option generally fits best. Nevertheless, in non-periodic cases this can result in heavy distortion. Figures 3.6d and 3.7d illustrate how observers that exit the domain are propelled even further away by wrapped boundaries.

4 Vortex Extraction

One of the oldest problems in fluid visualization is the extraction of vortices. Generally, vortices are understood as the rotating motion of a fluid around a common axis, called core line. The visibility of both, the rotational motion and the core line, depend on the chosen frame of reference. Although a multitude of vortex indicators [Hal05; Hal*16; JH95; JMT05] and vortex core lines definitions [Fuc*08; JMT05; LSD90; SH95b; SWH05; Wei*07b] have been proposed over the years, there still is no agreed upon definition of a vortex. Günther and Theisel [GT18b] give an overview of the evolution of vortex definitions and extraction techniques. For basic evaluations, we use two well accepted methods: the λ_2 vortex region criterion [JH95], and the traditional vortex core line definition from Sujudi and Haimes [SH95b].

4.1 Vortex Region Criteria

Vortex region criteria aim to highlight regions containing vortices, i.e., indicators typically take the form of scalar fields where particular high or low values indicate the presence of vortices. Typical visualization approaches for indicator fields are:

- Level sets/contours of the indicator field, which can be extracted by the Marching Cubes [LC87] or Marching Tetrahedra algorithm [DK91].
- Ridge or valley lines and surfaces of the indicator field according to Eberly's height ridges [Ebe*94], c.f. Section 2.10.1.

In the presence of multiple indicator fields, the resulting structures from one indicator can be color coded with the second indicator field to indicate coherence of the vortex indicators. One of the simplest vortex indicators is the vorticity magnitude $\|\boldsymbol{\omega}\|$ from Section 2.12. More sophisticated methods like the λ_2-criterion [JH95] are based on the observations made from the flow governing Navier-Stokes equations. Since this criterion builds on the vorticity tensor $\mathbf{\Omega}$ which is Galilean invariant, the λ_2-criterion is Galilean invariant as well. Recently introduced pathline-based methods—IVD and LAVD [Hal*16]—accumulate relative vorticity along pathlines in order to objectively highlight vortices. While vorticity itself is not objective [GGT17], the subtraction of two vorticity values cancels out spatially constant rotation of the reference frame, and thus is objective [Hal*16]. Drouot and Lucius [DL76] showed that the vorticity tensor $\mathbf{\Omega}$ can be made objective by viewing it in strain tensor basis, which itself is objective

$$\tilde{\mathbf{\Omega}} = \mathbf{\Omega} - \mathbf{W}, \tag{4.1}$$

(a) Von-Kármán Vortex Street Behind an Obstacle

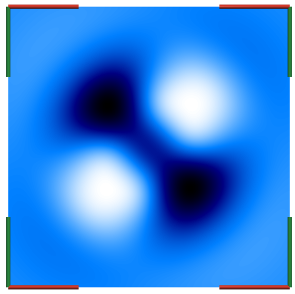

(b) Four Centers Model

Figure 4.1: The λ_2 vortex indicator field for a simulated von-Kármán vortex street (a) and the analytical four centers model from Section 8.1.1 (b).

where the rate of rotation tensor $\mathbf{W}$ is defined as $\frac{\mathrm{d}\mathbf{e}_i}{\mathrm{d}t} = \mathbf{W}\mathbf{e}_i$, with $\mathbf{e}_i$ being the eigenvectors of the strain rate tensor $\mathbf{S}$ (Section 2.13.1) and $\frac{\mathrm{d}}{\mathrm{d}t}$ being the total derivative. Hence, criteria building on the vorticity tensor become objective by substituting the vorticity tensor $\mathbf{\Omega}$ with $\tilde{\mathbf{\Omega}}$ [Mar*16].

4.1.1 λ_2-Criterion

We will briefly introduce a vortex indicator for 3-dimensional velocity fields, the λ_2 criterion by Jeong and Hussain [JH95]. The criterion can be adapted for 2-dimensional flow fields by viewing them as planar 3D flows, i.e., adding a zero-valued third component. The λ_2 indicator field highlights regions where the existence of a vortex is likely. Figure 4.1a shows the λ_2 scalar field of the flow around a cylinder. Vortices form behind the cylinder on the right and within four centers model (Section 8.1.1) are highlighted by the indicator (blue), compare Figure 4.1a.

The derivation of this criterion is motivated by the fact that rotational motion induces a pressure minimum in its center due to centrifugal forces the authors of this paper aim to indicate vortex regions based on the presence of local pressure minima. However, due to viscous effects and strain within the flow, vortices can exist without pressure minima and pressure minima can exist without vortices present. Jeong and Hussain tackle this by deriving the criterion from the flow governing Navier-Stokes equations and neglecting the unwanted effects during the derivation. The Navier-Stokes equations for incompressible flow read:

$$\frac{\mathrm{d}\mathbf{u}}{\mathrm{d}t} = \nu\nabla^2\mathbf{u} - \frac{1}{\rho}\nabla p + \mathbf{g}, \tag{4.2}$$

where $\frac{\mathrm{d}\mathbf{u}}{\mathrm{d}t}$ is the material derivative of $\mathbf{u}$, ν represents constant viscosity, $\nabla^2\mathbf{u}$ is the Laplacian of the vector field $\mathbf{u}$, ρ is density, p is pressure and $\mathbf{g}$ is the constant gravity vector. Local pressure minima are captured within the Hessian (second derivative) of pressure. Hence, the authors turn to the gradient of the Navier-Stokes equation:

$$a_{ij} = \nu \frac{\partial^3 u_i}{\partial^2 x_i \partial x_j} - \frac{1}{\rho}\frac{\partial^2 p}{\partial x_i \partial x_j}, \tag{4.3}$$

where $\mathbf{a} = (a_{ij})$ is the acceleration gradient, the Jacobian of the Laplacian of the velocity field $\mathbf{u}$ and the Hessian of pressure read:

$$\nabla(\Delta \mathbf{u}) = \frac{\partial^3 u_i}{\partial x_i^2 \partial x_j}, \quad \nabla(\nabla p) = \frac{\partial^2 p}{\partial x_i \partial x_j}. \tag{4.4}$$

For a compact representation the sum notation for matrices is used. Then a_{ij} is decomposed into symmetric and anti-symmetric parts:

$$a_{i,j} = \left[\frac{\mathrm{d}\mathbf{S}_{ij}}{\mathrm{d}t} + \boldsymbol{\Omega}_{ik}\boldsymbol{\Omega}_{kj} + \mathbf{S}_{ik}\mathbf{S}_{kj}\right] \tag{4.5}$$

$$+ \left[\frac{\mathrm{d}\boldsymbol{\Omega}_{ij}}{\mathrm{d}t} + \boldsymbol{\Omega}_{ik}\mathbf{S}_{kj} + \mathbf{S}_{ik}\boldsymbol{\Omega}_{kj}\right]. \tag{4.6}$$

The anti-symmetric part corresponds to the vorticity transport equation. However, we are only interested in the symmetric part, and since this decomposition is unique, one can directly work with a single part only. Note that the Hessian is by its nature symmetric and is therefore unaffected by this procedure. Accounting for the symmetric part $\mathbf{S}_u$ of $\nabla(\Delta \mathbf{u})$ and moving it to the other side yields:

$$\frac{\mathrm{d}\mathbf{S}_{ij}}{\mathrm{d}t} - \nu \mathbf{S}_u + \boldsymbol{\Omega}_{ik}\boldsymbol{\Omega}_{kj} + \mathbf{S}_{ik}\mathbf{S}_{kj} = -\frac{1}{\rho}\frac{\partial^2 p}{\partial x_i \partial x_j}. \tag{4.7}$$

By neglecting the unwanted effects, unsteady irrational strain $\frac{\mathrm{d}\mathbf{S}_{ij}}{\mathrm{d}t}$ and viscous effects $-\nu \mathbf{S}_u$, the Hessian of corrected pressure is given by: $\mathbf{R} = \mathbf{S}^2 + \boldsymbol{\Omega}^2$, c.f. Section 2.13.1. A local pressure minimum requires two positive eigenvalues of the pressure tensor $\nabla(\nabla p)$. This translates to two negative eigenvalues of the tensor $\mathbf{R}$. Since $\mathbf{R}$ is symmetric, all eigenvalues are real and can be ordered descendingly $\lambda_1 \geq \lambda_2 \geq \lambda_3$. The authors define vortex regions as connected parts of the velocity field with two negative eigenvalues of $\mathbf{R}$. Hence, the criterion was named λ_2 criterion.

4.2 Vortex Core Lines

Vortex core structures are the (local) axis around a fluid is rotating, i.e., points in 2D and lines in 3D space. A key advantage of vortex core lines is their concise representation of the rotational motion. Meaning a large part of the information of the vortex is captured by a (simple) geometrical structure. Typically, vortex core line definitions use the parallelism of two vector fields [SH95b; Wei*07b]. For example, the criterion by Sujudi and Haimes [SH95b] identifies core lines as loci where velocity and acceleration are parallel, i.e., $\mathbf{u} \parallel \mathbf{J_u u} = \mathbf{a}$, where the acceleration is given by the velocity field and its Jacobian. Thus, vortex core lines in three dimensions are commonly extracted using the parallel vectors (PV) operator by Peikert and Roth [PR99]. The parallelism of two vector fields also plays a role in the extraction of hyperbolic trajectories and bifurcation lines [Mac*16; MSE13], see Section 5.2.1, but is generally used to find vortex core lines, ridges and valleys, as well as separation and attachment lines [Ken98]. Hence, the following introduction of the parallel vectors operator will cover the general case of any two vector fields. In order to obtain specific features, such as vortex core lines, one chooses the two fields accordingly and later filters the resulting loci. For vortex core lines, this means, in addition to the parallelism of velocity and acceleration, we require local rotation, which is indicated by the presence of a pair of complex conjugate eigenvalues of the Jacobian.

4.2.1 The Parallel Vectors Operator

Suppose two vector fields $\mathbf{u}, \mathbf{v} : \mathbb{R}^3 \to \mathbb{R}^3$ sampled on a grid. The formulation of the parallel vectors operator (PV) by Peikert and Roth [PR99] extracts locations on the cell faces where in first approximation $\mathbf{u} \parallel \mathbf{v}$ holds. The authors propose two methods to find such loci:

1. Newton iteration on rectilinear cell faces of the cross product $\mathbf{u} \times \mathbf{v}$. Starting from the middle of the cell and taking a number of Newton-Raphson steps. Zeros of $\mathbf{u} \times \mathbf{v}$ found outside of the cell are discarded. Otherwise it is considered a solution point of $\mathbf{u} \parallel \mathbf{v}$.

2. Solutions of the following eigenvalue problem on triangular cell faces. Suppose the two vector fields are given for the vertices of a triangle, then a continuous approximation within the triangle can be obtained by barycentric interpolation (Appendix A.2.3). Barycentric interpolation uses three coordinates. However, two coordinates s, t are sufficient to uniquely identify a location within the triangle. Now suppose $\mathbf{u}$ and $\mathbf{v}$ can be represented by

$$\mathbf{U}\begin{pmatrix} s \\ t \\ 1 \end{pmatrix}, \quad \mathbf{V}\begin{pmatrix} s \\ t \\ 1 \end{pmatrix}, \tag{4.8}$$

where columns of $\mathbf{U}$ and $\mathbf{V}$ represent the vector field at the vertices. According to Peikert and Roth, locations where $\mathbf{u} \parallel \mathbf{v}$ can be found by solving

$$\mathbf{U}\begin{pmatrix} s \\ t \\ 1 \end{pmatrix} = \lambda \mathbf{V}\begin{pmatrix} s \\ t \\ 1 \end{pmatrix} \iff \mathbf{V}^{-1}\mathbf{U}\begin{pmatrix} s \\ t \\ 1 \end{pmatrix} = \lambda \begin{pmatrix} s \\ t \\ 1 \end{pmatrix}. \tag{4.9}$$

If either $\mathbf{U}$ or $\mathbf{V}$ is not invertible, choose the respective other one, if both are not invertible no solutions exists.

Note that the first method employs bilinear interpolation on cell faces, i.e., the approximation of the vector field on the cell face is quadratic, c.f. Appendix A.2.1 , while the second method approximates the vector field linearly on a triangular face. Futhermore, given a grid with rectilinear cell faces, the second technique can be applied by splitting each rectilinear cell face into two triangles. Due to the quadratic approximation of the vector fields by the first method, and the linear approximation used by the second method, the number and location of the solutions can differ.

Solutions on cell faces are intersections of the structure to be extracted with the respective cell faces. A triangulated, i.e., line or surface representation, is then obtained by connecting solutions on cell faces of the same grid cell.

Parallel Vectors in Space and Space-Time The type of resulting structure depends on the type of phenomena to be extracted. Given two general 2D vector fields $\mathbf{u}$ and $\mathbf{v}$, solutions of $\mathbf{u} \parallel \mathbf{v}$ are zero isolines of the function

$$\det(\mathbf{u}, \mathbf{v}) = \begin{vmatrix} u_1 & v_1 \\ u_2 & v_2 \end{vmatrix}, \tag{4.10}$$

since $\det(\mathbf{u}, \mathbf{v}) = 0 \Leftrightarrow \mathbf{u} \times \mathbf{v} = \mathbf{0} \Leftrightarrow \mathbf{u} \parallel \mathbf{v}$. In the general non-degenerate case this results in line structures in 2D space. However, if the two fields depend on each other, e.g., in the case of Sujudi and Haimes's vortex core line definition, the results need not be lines in 2D space.

Nevertheless, these raw solutions need to be filtered with the appropriate criteria, i.e., presence of complex conjugate eigenvalues of the Jacobian in the case of vortex core lines. If the input vector fields $\mathbf{u}$ and $\mathbf{v}$ are time-dependent, we may evaluate the parallel vectors operator in the space-time domain. As discussed in Section 2.1, we have two choices for the third component of each vector field. Setting the third component to 0 results in the space-time representation of the structures extracted by the original version. By setting the third component to a constant α, typically $\alpha = 1$, the solutions of $\mathbf{u}' \parallel \mathbf{v}'$ correspond to loci where both vector fields are equal, i.e., $\mathbf{u} = \mathbf{v}$. The resulting line in 2D space-time is a subset of the space-time surface defined by $\mathbf{u} \parallel \mathbf{v}$. To see this consider the cross product of the two vector fields

$$\mathbf{u}' \times \mathbf{v}' = \begin{pmatrix} u_1 \\ u_2 \\ \alpha \end{pmatrix} \times \begin{pmatrix} v_1 \\ v_2 \\ \alpha \end{pmatrix} = \begin{pmatrix} \alpha u_2 - \alpha v_2 \\ \alpha u_1 - \alpha v_1 \\ u_1 v_2 - u_2 v_1 \end{pmatrix} = \begin{pmatrix} \alpha u_2 - \alpha v_2 \\ \alpha u_1 - \alpha v_1 \\ \det(\mathbf{u}, \mathbf{v}) \end{pmatrix}. \tag{4.11}$$

So, in addition to parallelism of $\mathbf{u}$ and $\mathbf{v}$, being parallel in space-time also implies equality of the original fields. In the non-degenerate case those structures are lines.

4.2.2 Sujudi and Haimes Criterion

According to Sujudi and Haimes [SH95b] there are two necessary condition for a point $\mathbf{x}$ within a vector field $\mathbf{u} : \mathbb{R}^3 \to \mathbb{R}^3$ to be part of a vortex core line:

1. The Jacobian $\mathbf{J_u}(\mathbf{x})$ evaluated at the point $\mathbf{x}$ has a pair of complex conjugate eigenvalues. The corresponding eigenvectors span the plane of local rotation.

2. The eigenvector $\mathbf{e}_R$ belonging to the remaining real eigenvalue λ_R fulfills:

$$\mathbf{u} - (\mathbf{u}^{\mathrm{T}}\mathbf{e}_R)\mathbf{e}_R = \mathbf{0}. \tag{4.12}$$

   Meaning, projecting the $\mathbf{u}$ onto the plane of swirling motion spanned by the eigenvectors corresponding to the complex conjugate pair of eigenvalues of $\mathbf{J_u}(\mathbf{x})$ is the zero vector, i.e., massless particles on the core line solely move along the core line and exhibit no rotation.

Note that for general velocity fields this criterion is not Galilean invariant due to the fact that the velocity itself is not Galilean invariant. However, applied in 2D space-time, the criterion yields Galilean invariant vortex cores. Moreover, this criterion can be described by the parallelism of $\mathbf{u}$ and the real eigenvector of its Jacobian

$$\mathbf{u} \parallel \mathbf{J_u}\mathbf{u}. \tag{4.13}$$

For steady flows, this means velocity is parallel to acceleration $\mathbf{a} = \mathbf{J_u}\mathbf{u}$ of $\mathbf{u}$. Thus, solutions can be found by means of the parallel vectors operator Section 4.2.1. However, the resulting loci need to be filtered by the first condition, i.e., the presence of two complex conjugate eigenvalues of $\mathbf{J_u}$. Figure 4.2a shows a straight core line with streamlines swirling around it.

Curved core lines pose a fundamental problem for the criteria of Sujudi and Haimes. Velocity tangentially follows the core line , but acceleration, due to the curvature of the core line, points toward the center. Therefore, the extracted line, where $\mathbf{u} \parallel \mathbf{J_u}\mathbf{u} = \mathbf{a}$, is shifted. Figure 4.2b depicts a curved vortex core line (ground truth pink) with streamlines swirling (grey) around it, and the extracted solution by the method of Sujudi and Haimes [SH95b] (blue). To show that the extracted line cannot be a core line, we seed streamlines (yellow) around the base of the extracted line, and observe that they converge toward the ground truth, compare Figure 4.2c. The helix vortex core line model is adapted from Jung et al. [Jun*17].

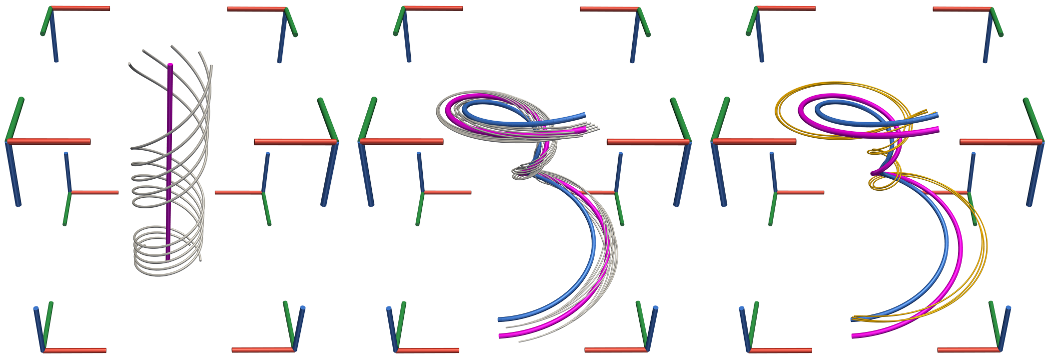

(a) Straight Vortex Core Line (b) Helix Vortex Core Line (c) $\mathbf{u} \parallel \mathbf{J_u u}$ Solution (blue)

Figure 4.2: Straight (a) and curved (b) core line (pink) and streamlines (grey) rotating around it. The Sujudi and Haimes solution coincides with the ground truth (pink). The solution extracted (blue) clearly deviates from the ground truth (pink) in the case of a curved vortex core line and streamlines (yellow) stray away toward the real solution (c).

5 Vector Field Topology

A commonly employed technique for vector field visualization is the extraction of features that separate the domain into regions of similar behavior. Here, we distinguish between techniques for autonomous and non-autonomous systems. Although in practice snapshots at a constant time of an unsteady field are often visualized using techniques from steady vector field analysis. Hence, we first introduce the classical steady vector field topology before moving on to the time-dependent case. (Steady) vector field topology is as feature based visualization techniques, i.e., its goal is to describe the flow by a set of areas with coherent behavior [HH91].

5.1 Steady Vector Field Topology

Steady vector field topology, for two and three dimensional vector fields, was first presented by Helman and Hesselink [HH89; HH91], and has since become a standard tool for steady vector field visualization [Asi93; Lar*07; Pob*11; Pos*03]. The extension to four dimensional vector fields was recently introduced by Hofmann et al. [HRS18]. These methods work in two basic steps

1. Extract special fixed points of the vector field, called critical points,
2. Outgoing from these critical points, compute invariant manifolds that act as separating structures, which take the form of streamlines in 2D and stream surfaces in 3D space.

The resulting topological skeleton is stable under small perturbations.

5.1.1 Critical Points

Critical points are isolated zeros of a vector field. Wwe consider first-order critical points, since higher-order critical points are not structurally stable [Sch*97; Wei*05].

Definition 5.1 (Critical Point)**.** Let $\mathbf{u} : \mathbb{R}^n \to \mathbb{R}^n$ be an n-dimensional vector field. Then an equilibrium (fixed) solution $\mathbf{x}$ is called critical point if its Jacobian has no zero eigenvalues, i.e., $\mathbf{u}(\mathbf{x}) = \mathbf{0}$ and $\det(\mathbf{J_u}(\mathbf{x})) \neq 0$.

The stable and unstable manifolds of the linearized system are determined by the eigenvalues and eigenvectors of the Jacobian. Hence, the eigenvalues are used to classify a critical point. The eigenvectors are an approximation of the global invariant manifolds, which may be obtained by integration. In two dimensions, critical points can be classified as follows. Let R_1 and R_2 be the real parts of the eigenvalues of $\mathbf{J}$, and I_1, I_2 are the imaginary parts. Note that complex eigenvalues can only occur in complex conjugate pairs since the Jacobian has only real entries. We distinguish the following combinations:

$$\begin{aligned} \text{repelling node:}\ & R_1, R_2 > 0 \quad I_1, I_2 = 0, \\ \text{attracting node:}\ & R_1, R_2 < 0 \quad I_1, I_2 = 0, \\ \\ \text{repelling focus:}\ & R_1, R_2 > 0 \quad I_1, I_2 \neq 0, \\ \text{attracting focus:}\ & R_1, R_2 < 0 \quad I_1, I_2 \neq 0, \\ \\ \text{saddle:}\ & R_1 \cdot R_2 < 0 \quad I_1, I_2 = 0. \end{aligned} \tag{5.1}$$

The real part characterizes the divergence behavior of a critical point, while the imaginary part corresponds to the rotation around the critical point. Therefore, it is common practice to characterize the strength of a saddle by its hyperbolicity, i.e., the product of its eigenvalues $h = \lambda_1 \cdot \lambda_2$. Nodes, on the one hand, are measured by $\lambda_{\max}$, the largest eigenvalue of $\mathbf{J}$, representing the divergence of a critical point. Foci, on the other hand, are often characterized by the strength of their rotation. Hence, the strength of a focus is measured as the Euclidean norm of any of the two imaginary parts $\|I_i\|_2$. Since the imaginary parts are complex conjugates, their Euclidean norm is equal. Repelling nodes and foci are often called sources, while their attracting counter parts are called sinks. Figures 5.1 and 5.2 illustrate the different types of critical points. In three or more dimensions there also exist spiraling types of critical points in various combinations with source and sink behavior. Hofmann et al. [HRS18] give a detailed classification.

All types of critical points mentioned up to this point are structurally stable, meaning small perturbations do not affect their qualitative behavior. However, there is an additional interesting case in 2D, the so-called center type critical point

$$\text{center:}\ R_1, R_2 = 0 \quad I_1, I_2 = 0.$$

Often times fluid simulations assume incompressibility, i.e., $\mathrm{div}(\mathbf{u}) = 0$. This means, neither attracting nor repelling foci and nodes exist. Center type critical points represent rotation in these types of vector fields.

5.1.2 Poincaré-Hopf Index

The Poincaré-Hopf index of a two-dimensional critical point is defined as the number of counterclockwise revolutions of the vector field, made while moving in counterclockwise direction along a closed curve around the critical point (containing no other critical points); clockwise revelations are denoted negatively. Tricoche et al.

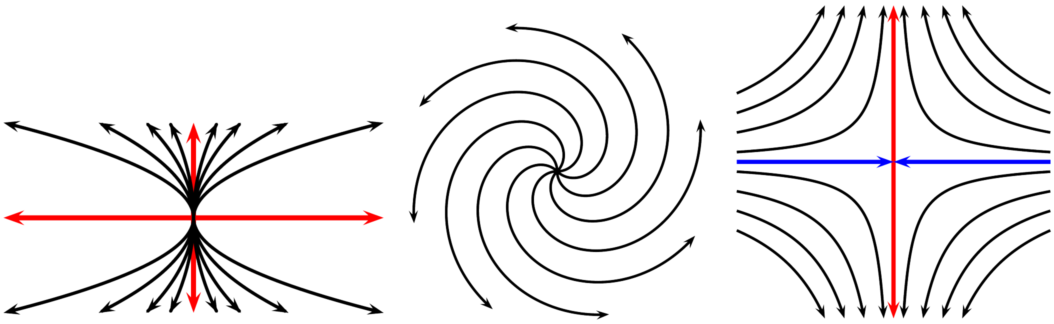

(a) Node (b) Focus (c) Saddle

Figure 5.1: Critical points in 2D vector fields. Eigenvectors corresponding to positive eigenvalues (red) and negative (blue), indicate repelling, and attracting behavior. Repelling node (a), repelling focus (b), saddle (c). Opposite cases are obtained by field inversion. Images from Sadlo [Sad10].

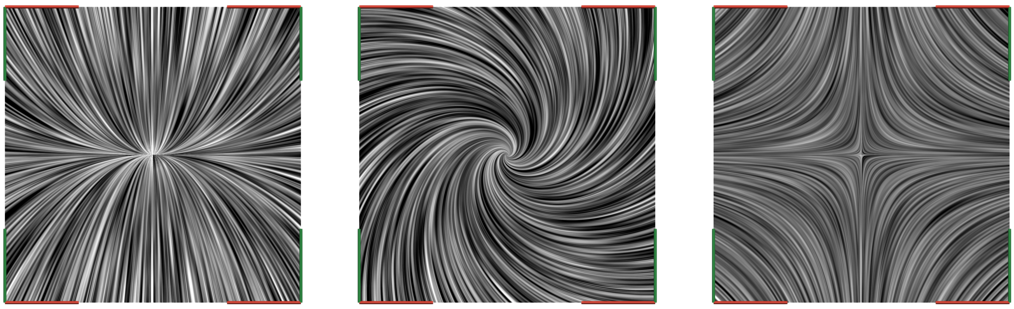

(a) Node (b) Focus (c) Saddle

Figure 5.2: Types of critical points in 2D vector fields. The behavior around the respective critical point is indicated by line integral convolutions (LIC) [CL93; SH95a].

give a more detailed definition [TSH01]. The Poincaré-Hopf indices of the previously mentioned first-order critical points are as follows:

- $+1$ for nodes and foci,
- -1 for saddles.

The important implication of the Poincaré–Hopf theorem is the fact that critical points are created in pairs of opposite index, i.e., saddle and node, or saddle and focus. This type of event is called fold bifurcation. There exist additional types of bifurcations, e.g., transcritical and pitchfork bifurcations, but we will focus on the simple case of fold bifurcations.

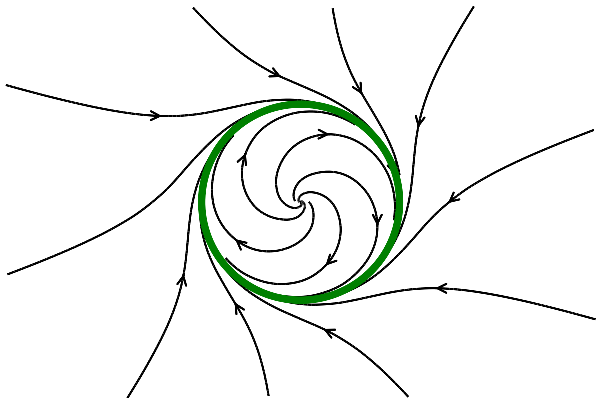

Figure 5.3: A limit cycle (green) with nearby trajectories converging towards it. [a]

[a]Adapted from Visualization of Periodic Orbits in Space and Time, page 16, 2017 from Lutz Hofmann, with permission from the author.

5.1.3 Limit Cycle

Another type of bifurcation is the so-called Andronov-Hopf bifurcation. During an Andronov-Hopf, or simply Hopf, bifurcation, a critical point changes stability, from stable to unstable or vice versa, via a pair of purely imaginary eigenvalues of its Jacobian. In the process, a stable or unstable limit cycle emerges. We discuss an example in Section 8.2.2. A limit cycle is a special type of periodic orbit, the mathematical foundation is given by Floquet theory, we refer to Verhulst [Ver06] for a detailed introduction. Periodic orbits of an autonomous systems are closed tangent curves $\mathcal{L}(s)$ (Figure 5.3), they map multiple values of s to the same point

$$\mathcal{L}(s) = \mathcal{L}(s') = \bar{\mathbf{x}}. \tag{5.2}$$

If $\mathbf{u}(\mathbf{x}) = \mathbf{0}$, the tangent degenerates to a single point. Otherwise ($\mathbf{u}(\mathbf{x}) \neq \mathbf{0}$) the tangent curve is a periodic orbit:

$$\begin{gathered}\mathcal{L}(s + k\,T) = \mathcal{L}(s) \\ \text{with } t, T \in \mathbb{R},\ k \in \mathbb{R}.\end{gathered} \tag{5.3}$$

Periodic orbits and limit cycles are analyzed by means of Poincaré maps [Asi93].

5.1.4 Computation of Invariant Manifolds

Solutions seeded within an invariant manifolds stay within it for all time. Hence, finding an initial solution on the invariant manifold suffices and the entire manifold is obtained by integration. We can exploit this fact to correct for any imprecision during the seeding and integration process. From Section 2.5 we know that the linearized invariant manifolds coincide with the global ones in close vicinity of the

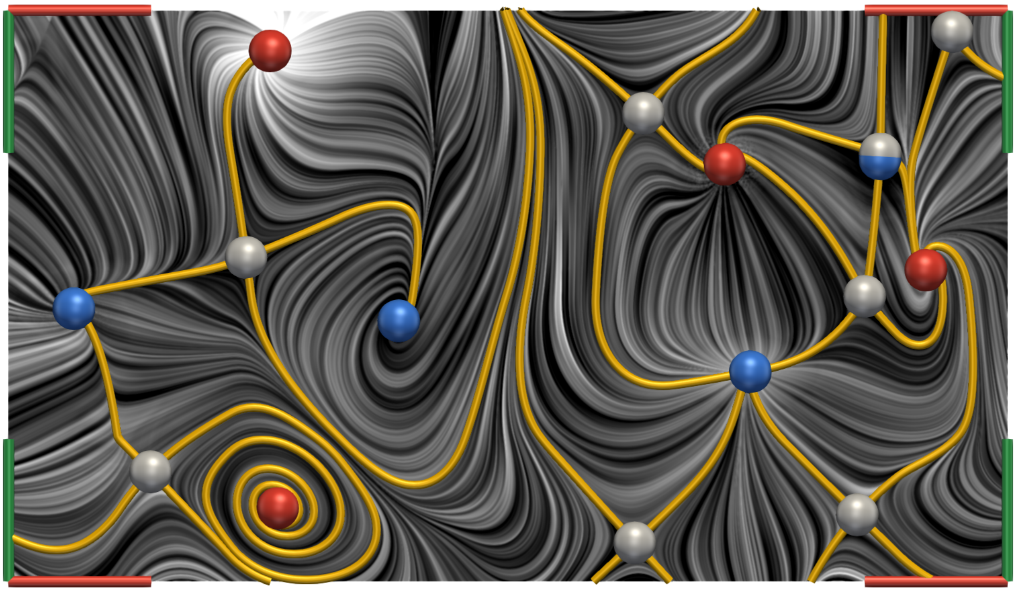

Figure 5.4: Topological skeleton of a 2D random vector field. Saddle (white), sink (blue) and source (red) type critical points. The corresponding invariant manifolds (yellow) seeded from the saddle-type critical points according to Section 5.1.4.

critical point. Thus, we may obtain seeds for the numerical integration from the eigenvectors of the Jacobian of saddle-type critical points. The following algorithm was first presented by Parker and Chua [PC12].

Let $\bar{\mathbf{x}}$ be a saddle-type critical point and λ^u an eigenvalue with positive real part $R_{\lambda^u} > 0$. Since the unstable manifold is going outward from the critical point it can be computed in forward time. In order to obtain the stable manifold, the process is repeated for eigenvectors with negative real part. Then a seed for the manifold is found by an offset in direction of the eigenvector $\mathbf{e}^u$,

$$\mathbf{x}_\alpha = \bar{\mathbf{x}} + \alpha \mathbf{e}^u, \tag{5.4}$$

and the second half may be obtained by inverting the sign of the eigenvector. An appropriate offset factor α can be found iteratively. With suiting seed offsets from the saddle-type critical point, the unstable manifold is obtained by forward integration and the stable manifold by backward integration, i.e., in reverse time.

With this we can construct the topological skeleton of a steady vector field. Figure 5.4 depicts the extracted topological skeleton of a steady random 2D field. Critical points, indicated by spheres with respective color for saddle (white), stable (blue), and unstable (red) type critical points. Separatrices computed from the saddle-type critical points are shown in yellow.

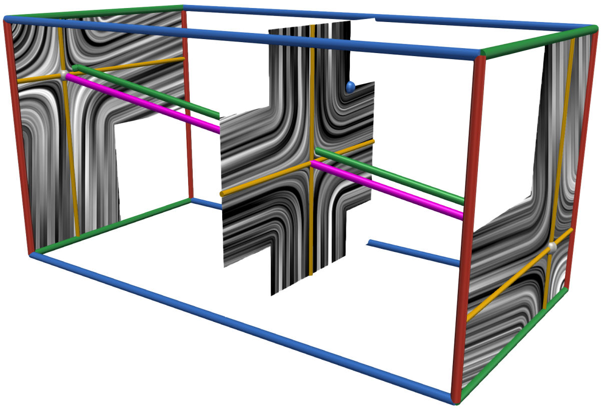

(a) Linear Gyre Saddle LIC

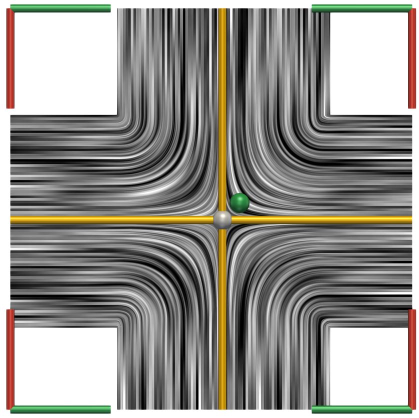

(b) Time-Slice at $t = 2.2$

Figure 5.5: Space-time view of the time-dependent linear moving gyre saddle model within the domain $[-1, 1]^2 \times [0, 4]$, where time increases from left to right (a). Steady vector field topology applied in three time steps at $t = 0, t = 2.2, t = 4$, based on saddle-type critical points (gray) and separatrices (yellow). The bifurcation line (green) extracted as proposed by Sadlo and Weiskopf [SW10] does not coincide with the trajectory of the instantaneous saddle point (b).

5.2 Streak-Based Vector Field Topology

We have seen in Section 2.7 that instantaneous stability analysis cannot generally be used to characterize the stability of time-dependent systems. With this in mind, it may seem natural to extend the steady vector field topology to the time-dependent case by employing pathlines instead of streamlines, i.e., invariant manifolds could be represented by special pathlines originating from saddle-type critical points. This type of time-dependent vector field topology was introduced by Theisel et al. [The*05b]. However, this approach segments the domain into regions of locally different behavior, which does not necessarily coincide with structures separating the physical flow of particles, called Lagrangian coherent structures (LCS), as introduced in Section 2.9. Therefore, another type of time-dependent vector field topology was presented by Sadlo and Weiskopf [SW10] that builds on streaklines, hyperbolic trajectories and LCS. Although Lagrangian coherent structures are by now widely used to analyze time-dependent flow fields, their extraction is still computationally costly. Therefore, it is desireable to have a framework, similar to steady vector field topology, that is based on certain types of characteristic curves (Section 2.2), that coincide with LCS. Streak-based vector field topology achieves exactly that. In this section we discuss the original proposal of Sadlo and Weiskopf [SW10], as well as the improvements from Machado et al. [Mac*16; MSE13]. We limit ourselves to the two dimensional case. However, an extension to the three dimensional case was introduced by Üffinger et al. [ÜSE13], and the techniques presented may therefore be extended in similar fashion.

The approach by Sadlo and Weiskopf is in accordance with the findings of Haller [Hal00]. The place of saddle-type/hyperbolic critical points in steady vector field topology are taken by hyperbolic trajectories in the time-dependent case. Figure 5.5 shows the gyre saddle model with a linearly moving saddle point in 2D space-time. The trajectory of the instantaneous saddle point (pink line) does not coincide with the hyperbolic trajectory (green line) extracted as bifurcation line. As we have seen in Section 2.11, hyperbolic trajectories give rise to stable and unstable manifolds. These manifolds can be viewed as stream surfaces in space-time or as generalized streaklines (see Section 2.2.3) where the seed curve is given by the hyperbolic trajectory. One difficulty associated with the time-dependent character of hyperbolic trajectories was overcome by the theoretical advances of Haller [Hal00; Hal01], who showed that in physical flows the instantaneous hyperbolicity along a trajectory is a necessary condition for the existence of a hyperbolic trajectory, which can be obtained from eigenvalues of the instantaneous Jacobian. Therefore, the computation of the streak-based vector field topology can be broken down into two steps:

1. Extract the hyperbolic trajectories,
2. Determine the seed structures for the invariant manifolds and compute them.

According to Haller (see Section 2.11) seeding points for the hyperbolic trajectories can be found by local maxima in the hyperbolicity time indicator field (Equation (2.36)). He argues that intersections of ridges in the forward and reverse FTLE field give more numerical stable results. This was confirmed by Sadlo and Weiskopf, who show that FTLE ridges outperform the hyperbolicity time approach. They further argue that the original approach using hyperbolicity time suffers from heavy aliasing and the conditions for uniform hyperbolicity are to restrictive to be employed on real-world data sets. Sadlo and Weiskopf directly use intersections of forward and backward FTLE ridges without additional filtering for uniform hyperbolicity.

A naive approach for the extraction of hyperbolic trajectories could be as follows: 1) Find local maxima of hyperbolicity time at some fixed time step, and 2) numerically integrate them forward and backward to extract the entire trajectory. Practice shows that this is an extremely difficult task, because of exponential growth of numerical errors due to the presence of an unstable manifold in both forward and reverse time. This issue could be addressed by obtaining the entire trajectory be FTLE intersections, i.e., the extracting of FTLE ridges over the entire space-time domain. It becomes immediately clear that this is a very costly computational task. These issues were addressed by Machado et al. [Mac*16; MSE13], who showed that hyperbolic trajectories may be extracted as bifurcations lines in 2D space-time.

5.2.1 Bifurcation Lines

Bifurcations lines of a steady 3D vector field, as first proposed by Perry and Chong [PC87], are streamlines that exhibit both, a stable and unstable manifold. One extraction method for these line features is based on an extension of Kenwright et al.

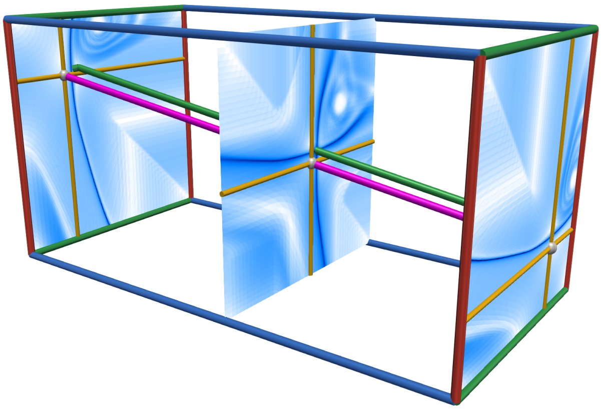

(a) Linear Saddle FTLE

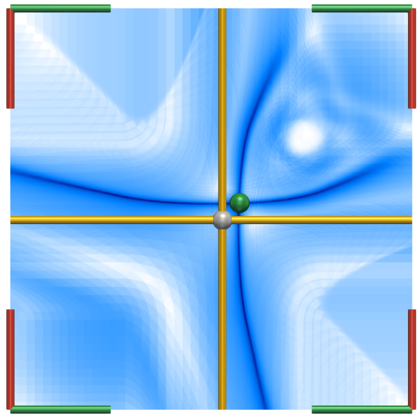

(b) Superimposed FTLE at $t = 2.2$

Figure 5.6: FTLE of the time-dependent linear moving gyre saddle in space-time at $t = 0, t = 2.2, t = 4$ (a). Forward FTLE with initial time t_0 and advection time $T = 4$ (left slice), Superimposed forward and backward FTLE with $t_0 = 2$ and $T = \pm 2$ (middle slice), and backward FTLE with $t_0 = 4$ and $T = -4$ (right slice). Superimposed forward and backward FTLE (b) reveals that the extracted bifurcation line (green) coincides with the hyperbolic trajectory.

[KHL99]. Roth [Rot00] showed that this is equivalent to the vortex core criterion from Sujudi and Haimes [SH95b], where instead of requiring local rotation one requires hyperbolicity, i.e., the existence of two real eigenvalues of the Jacobian with opposite signs. Although this also introduces the problems associated with curved feature lines as discussed in Section 4.2.2, other parallel vectors formulation may also be employed. Specifically, the higher-order method from Roth and Peikert [RP98], that is able to extract curved lines, but might fail entirely in other cases. Note however, that the loci extracted by the parallel vectors operator are generally not part of the same stream line in space-time. Therefore, further (iterative) optimizations are needed to decrease the angle between the tangent of the extracted line and the vector field. The goal of this step is to fit the extracted line locally to a streamline in space-time, since, as the name implies, hyperbolic trajectories are pathlines of the underlying unsteady 2D vector field. Machado et al. [Mac*16] presented an algorithm to fit raw solutions of the PV operator to nearby streamlines that exhibit low cross flux, thereby finding a bifurcation line. We refer to the unfitted solutions of the parallel vectors operator as "raw solutions". Figure 5.6 shows, that, in case of straight hyperbolic trajectories, the bifurcation line approach is able to confidently extract the correct solution, i.e., the extracted structure coincides with intersection points of forward and backward FTLE ridges. The depicted gyre saddle model is presented in great detail in Section 8.1.2, this includes various derived models that exhibit curved hyperbolic trajectories.

In all cases, the seeds for the invariant manifolds are computed by using the eigenvectors of the Jacobian at a number of discrete time steps, analogously to Sec-

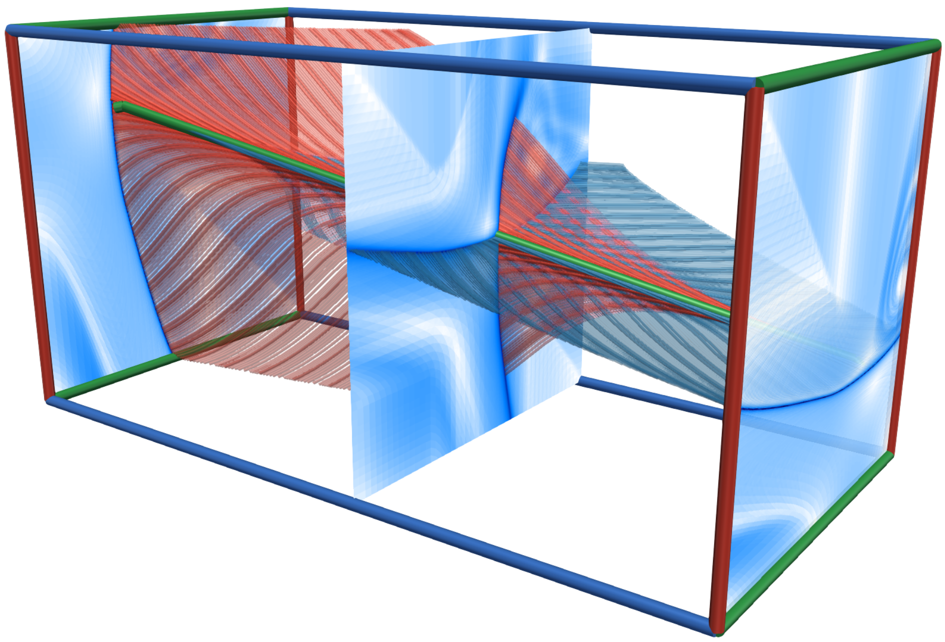

Figure 5.7: Gyre saddle model with linear moving saddle-type critical point, depicted in space-time with time increasing from left to right. Forward FTLE at time $t = 0$ with advection time $T = 4$, superimposed forward and backward FTLE at time $t = 2.2$ with $T = \pm 4$ and backward FTLE at $t = 4$ with $T = -4$. The stable (blue) and unstable (red) manifold of the bifurcation line coincide with the forward and backward FTLE ridges.

tion 5.1.4. From the resulting seed curves, one may compute generalized streaklines (Section 2.2.3) to obtain the invariant manifolds in space, i.e., use stream surfaces in the space-time domain. It is worthy to note that the numerical integration of the invariant manifolds is not subject to the same difficulties as the extraction of hyperbolic trajectories, since they are attracting in either forward or reverse time. Thus, numerical errors during integration and imprecisions when computing the offset of the seeds are compensated to some degree. In case of the linear gyre saddle model, Figure 5.7 shows that the streak manifolds align well with FTLE ridges in both forward and revers time.

6 Local Frames of Reference

Chapter 3 introduces the concept of frames of reference. There, the entire domain is seen through the eyes of one observer. This observer may be moving according to one of four classes of domain transformations, 1) Galilean, 2) rotation, 3) rigid body, and 4) affine transformations. Although not explicitly mentioned, this also means that the time-dependence of certain phenomena depend on the motion of this observer. Moreover, is it possible to find an observer such that the vector field appears steady? In quickly becomes clear that this is not generally possible as shown by Perry and Chong [PC87]. Consider multiple vortices moving relative to each other, compare Figure 6.1. In order to observe each vortex as steady, we would need to move alongside all of them at the same time. Thus, only vector fields that can be described in their entirety by one of the aforementioned transformations can be steadified in this manner. From this, we can directly conclude that local frames of reference are required to view an arbitrary vector field (locally) steady. In our example, we would at least require four such frames of reference. However, as Figure 6.1 indicates, when the vortices collide with the outer boundary, the flow becomes turbulent and the number of required observers increases. Figure 6.1d suggests that we may need an observer for each point in space in order to view it as steady. This means, the number of observers becomes unbounded.

A steady vector field, in general, carries less information than a time-dependent one. However, some feature extraction techniques, e.g., vortex indicators or vector field topology, work only very limited—if at all—on time-dependent vector fields. There are time-dependent counter parts, like streak-based vector field topology, but they are generally more expensive to compute, and for vortex detectors there only exist very few options [Wei*07b]. Hence, steady methods are also applied to the time-dependent case when the change of the vector field over time, i.e., its time derivative, is sufficiently small. However, as Section 2.7 shows, this leads to misinterpretations.

In order to remedy these problems, the following approaches aim to find a vector field that describes the motion of an (infinite) set of observers so that the change of the original vector field is minimal along world lines, i.e., along pathlines of the observer vector field. To be more specific, let $\mathbf{u} : \mathbb{R}^n \times \mathbb{R} \to \mathbb{R}^n$ be a time-dependent vector field, then the goal is the find a second time-dependent vector field $\mathbf{v} : \mathbb{R}^n \times \mathbb{R} \to \mathbb{R}^n$ so that the original field $\mathbf{u}$ can be transformed to a steady-as-possible field $\mathbf{w} : \mathbb{R}^n \times \mathbb{R} \to \mathbb{R}^n$. The precise meaning of as steady-as-possible of

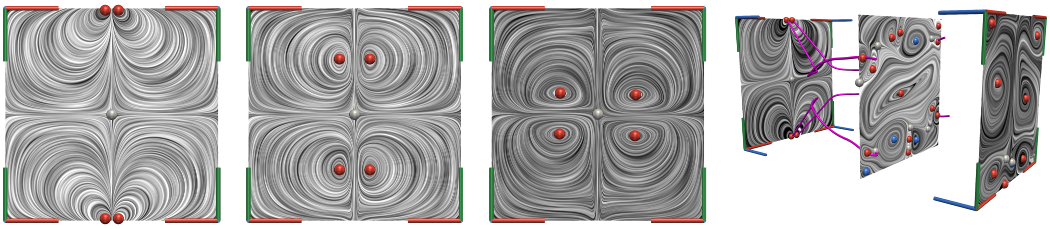

(a) Vortices at $t = 0$ (b) $t = 0.1$ (c) $t = 0.4$ (d) Space-Time View

Figure 6.1: Snapshots of the buoyant plumes dataset (Section 8.3.2) at times $t = 0$ (a), $t = 0.1$ (b) and $t = 0.2$ (c). Space-time view of the entire domain $[0, 1]^2 \times [0, 2]$ (d). Critical points, saddle (grey), repelling (red) and attracting vortices (blue) collide with the outer domain boundary and the flow becomes turbulent.

$\mathbf{w}$ takes two mathematical forms which will be introduced in the respective context. One may view this as a decomposition of the original field

$$\mathbf{u} = \mathbf{v} + \widetilde{\mathbf{w}}. \tag{6.1}$$

$\widetilde{\mathbf{w}}$ is still a time-dependent field but represents the steady field $\mathbf{w}$ in the original frame of reference. The steady-as-possible field $\mathbf{w}$ is obtained by translating $\widetilde{\mathbf{w}}$ into a new frame of reference according to Equation (3.3) from Section 3.1. If we can find such a field, analysis methods from the realm of steady vector fields can be transferred to the time-dependent case. Whether the application of these techniques to the transformed field yields the desired results is discussed in Chapter 8. The observer field is sometimes modeled as a mean flow velocity field and by subtracting it from the original field, the newly created field $\widetilde{\mathbf{w}}$ can be easier to analyze by traditional methods. Wiebel et al. [WSG04] proposed to use the harmonic part of the Helmholtz-Hodge decomposition (HHD), see Section 2.13.2. More detailed information is given by Bhatia et al. [Bha*13]. Bhatia et al. introduced their natural HHD in order to improve vortex detection. Bujack et al. [BHJ16] proposed to analyze vector fields in their internal frame, which they construct by extracting the harmonic part from the natural HHD [BPB14], a variant of the HHD that guarantees that the harmonic part captures all external influences.

For now, we present two methods that aim to find such an observer vector field along which the original vector field appears as steady-as-possible, while locally restricting the observer motion to one of the aforementioned domain transformation classes (Chapter 3). The idea of the two papers presented in this chapter is to view the vector field through the eyes of multiple observers. In the earlier example of relatively moving vortices, each vortex is seen through the eyes of an observer moving with the vortex and thereby observing a steady vector field. The main difference between the two techniques is that the first models observers that have a fixed neighborhood size, i.e., that view a small cutout of the vector field around them, while the second models this neighborhood as an infinitesimal patch, i.e., is based on derivatives of the original field.

6.1 Generic Objective Vortices

The technique described in this section is a summary of recent publications of Günther and Theisel and others. Over the years the authors addressed the extraction of vortices in different settings [GT14; Wei*07b]. In 2016 they introduced a framework that makes existing Galilean invariant vortex indicators rotation invariant [GST16], followed by a revised version that enabled existing vortex extractors to become objective [GGT17]. Recently, this approach was extended to the class of affine domain transformation (Section 3.2.4), which they called hyperobjective vortices [GT18a]. We will briefly discuss the methods concerning objectivity and hyperobjectivity, i.e., we restrict observer motion to rigid body motion and affine transformations:

$$\mathbf{g}(\mathbf{x}, t) = Q(t)\mathbf{x} + \mathbf{c}(t), \quad \mathbf{g}(\mathbf{x}, t) = R(t)\mathbf{x} + \mathbf{c}(t), \tag{6.2}$$

where $Q \in \mathrm{SO}(n)$ and R is a general invertible matrix. The authors estimate an optimal frame of reference locally for every point $(\mathbf{x}, t)$, where the local frame is described by $(Q, \mathbf{c})$. The local frame is than fitted so that the resulting field $\mathbf{w}$ becomes as steady-as-possible, which in this context means $\frac{\partial \mathbf{w}}{\partial t} \to \min$. This estimation is evaluated in a neighborhood U of each individual point $(\mathbf{x}, t)$ which includes the solution of the spatial and temporal derivatives, e.g., $\dot{Q} = \frac{\mathrm{d}Q}{\mathrm{d}t}, \ddot{Q}, \dot{\mathbf{c}} = \frac{\mathrm{d}\mathbf{c}}{\mathrm{d}t}, \ddot{\mathbf{c}}$. Since the solutions of all derivatives are fitted to the local reference frames, they can no longer be obtained via finite differences, i.e., they need to be provided with the resulting observer vector field $\mathbf{v}$ and the as steady-as-possible field $\mathbf{w}$. The authors avoid solving for $\dot{Q}, \ddot{Q}, \dot{\mathbf{c}}, \ddot{\mathbf{c}}$ directly by solving a suitable combination:

$$\mathbf{v}_t^* = Q(\mathbf{v}_t - M\mathbf{u}), \tag{6.3}$$

where M is an $n \times 4n$ matrix containing positions and derivatives of $\mathbf{w}$ that the reference frame $(Q, \mathbf{c})$. The derived form is minimized within the neighborhood U

$$\int_U \|\mathbf{v}_t^*\| \, \mathrm{d}V \to \min. \tag{6.4}$$

From the solution, the observer vector field $\mathbf{v}$ and the as steady-as-possible field $\mathbf{w}$ can be constructed. For details and a proof of the derivation we refer to the original papers [GGT17; GT18a]. Depending on the chosen class of permitted observer motion, rigid body motion or affine transformations, the form of M and the later derivation of the vector fields vary. For us it shall suffice that the resulting observer field yields an as steady-as-possible field, which in this case is measured by the time derivative of $\mathbf{w}$. We note that in the case of 2D time-dependent vector fields, one may use $\widetilde{\mathbf{w}}$ directly to extract features, by representing it in the space-time domain. This avoids computation of the flow map which in practice might not be trivial due to the existence of domain boundaries, see Section 3.3.1.

Feature extraction techniques based on the resulting vector fields and its derivative are objective and hyperobjective respectively. All that is required is substitution of the vector field and its derivative by the newly computed ones and this can be easily employed as a preprocessing step. However, a small drawback is the fact that measures based on higher order derivatives, which are not derived in the publication, need to be derived after the fact. Traditional derivation methods such as finite differences or least-squares estimation cannot be employed.

The existence of the discrete neighborhood U is undesirable, since this implies an direct connection between neighboring points. Although the resulting frame is a local frame, but not an infinitesimal local frame which we would expect in the general case. The authors address this issue by providing an option to collapse the neighborhood U to a single point [GGT17, App. C]. With this the approach becomes truly local. However, the construction of this truly local version requires the computation of third-order derivatives, which have limited numerical stability. The approach by Hadwiger et al. [Had*19], see Section 6.2, achieves objectivity with a truly locally computed frame based only on first-order derivatives.

The observer velocity fields of objective frames computed this way are divergence-free. This changes when moving to the hyperobjective case, i.e., affine domain transformations. The authors argue that this is due to the fact that in unsteady flows vortices can grow, thereby sucking more and more fluid into the vortex. Since this cannot occur in steady flows, the observer velocity field needs to account for this change. Hence, in order to be able to steadify growing or scaling vortices, the observer field cannot be divergence-free. Another typical phenomena described by affine transformations is that of shear. According to the authors, shear within the observer velocity field describes the difference of velocity of fluid patches next to each other. For example, consider a tube with fluid flowing through, where fluid near the boundary necessarily moves slower than fluid in the middle, since it is slowed down by friction of inner surface of the tube.

6.1.1 Feature Flow Field

The feature flow field (FFF) approach was presented earlier in 2003 by Theisel and Seidel [TS03]. The main idea is to find paths, not necessarily pathlines, along which a vector field is as steady as possible. In 2D time-dependent flow this achieved by the cross product of the two components

$$\mathbf{f}(\mathbf{u}) = \mathbf{f}\begin{pmatrix} u_1(\mathbf{x},t) \\ u_2(\mathbf{x},t) \end{pmatrix} = \nabla u_1 \times \nabla u_2 = \begin{pmatrix} \det(\mathbf{u}_{x_2}, \mathbf{u}_t) \\ \det(\mathbf{u}_t, \mathbf{u}_{x_1}) \\ \det(\mathbf{u}_{x_1}, \mathbf{u}_{x_2}) \end{pmatrix}. \tag{6.5}$$

According to the authors this is equivalent to $\mathbf{f} = \mathbf{J}_{\mathbf{u}}^{-1}\mathbf{u}_t$, which they used in there derivation of another Galilean invariant vortex core line criterion [Wei*07b]. Following their argumentation, this relates to the current objective observer technique [GGT17] in the sense that the observer velocity field $\mathbf{v}$ is equivalent to the feature flow field in the case of Galilean observer motion.

Feature flow fields were applied in a number of settings, including critical point and vortex core tracking [Wei*07a]. Divergence issues due to accumulation of numerical errors was later addressed by Weinkauf et al. [Wei*10] by extending the original approach to include an attracting field that steers numerical integration toward desired trajectories, see stable feature flow fields. However, for the application at hand, the original idea will suffice.

6.2 Approximate Observer Killing Fields

Hadwiger et al. [Had*19] present a technique that can serve as a framework for objective feature extraction for vector fields. In this case, only the objective case is presented, i.e., observers with approximate local rigid body motion. Similar to Günther and Theisel the approach by Hadwiger et al. [Had*19] uses a minimization formulation to estimate an observer field $\mathbf{v}$ along which the original field $\mathbf{u}$ is as steady-as-possible. In contrast to the method of Günther and Theisel [GT18a], the only output is the observer field and the resulting nearly steady field $\mathbf{w}$ without the need for a discrete local neighborhood or higher-order derivatives of the original field. Therefore, derivatives of the observer velocity field can be obtained by traditional methods like finite differences. In order to obtain this observer field they trade-off locally rigid body motion of the observer field and steadiness of the resulting field $\mathbf{w}$. The steadiness is captured by the autonomous Lie derivative of the two fields:

$$\begin{aligned} \mathscr{L}_{\mathbf{v}}\mathbf{u} &= \frac{\mathscr{D}}{\mathscr{D}\widetilde{\mathbf{w}}} = \frac{\mathscr{D}}{\mathscr{D}\mathbf{u}_{\mathbf{v}}} = \frac{\mathscr{D}}{\mathscr{D}(\mathbf{u}-\mathbf{v})} \\ &= \frac{\partial \mathbf{u}}{\partial t} - \frac{\partial \mathbf{v}}{\partial t} + (\nabla\mathbf{u})\mathbf{v} - (\nabla\mathbf{v})\mathbf{u}. \end{aligned} \tag{6.6}$$

Equation (6.6) represents the change of the original field $\mathbf{u}$ along tangent curves (pathlines) of the observer field $\mathbf{v}$. Consider an observer represented by a Galilean transformation, i.e., the observer field $\mathbf{v}$ has constant velocity and no local rotation. With that $\frac{\partial \mathbf{v}}{\partial t} = \mathbf{0}$ and $(\nabla\mathbf{v})\mathbf{u} = \mathbf{0}$, Equation (6.6) collapses to the time derivative

$$\frac{\mathscr{D}}{\mathscr{D}\mathbf{u}_{\mathbf{v}}} = \frac{\partial \mathbf{u}}{\partial t} + (\nabla\mathbf{u})\mathbf{v}. \tag{6.7}$$

Hadwiger et al. also proof this fact for rigid body observer motion [Had*19, App. D]. The second part, restricting observer motion to rigid body motion, is achieved by requiring that the observer field is locally an approximate Killing vector field [JJ08]. Killing vector fields are special in the sense that they preserve metrics, i.e., they are infinitesimal isometries. We note that in Euclidean space they corresponds to all rigid body motion and can thus, be nicely used as a necessary condition for the observer vector field. We will see shortly that approximate Killing fields, although they do not represent perfect rigid body motion, have the advantage to better fit to slightly non-rigid motion observers. For more detailed information on the use of Killing fields we refer to the original paper, general information on Killing fields is presented by Ben-Chen et al. [BC*10] and Kilian et al. [KMP07]. The authors measure the "Killingness" by the so-called Killing energy, which is twice the strain-rate tensor $\mathbf{S}$ of $\mathbf{v}$ (Section 2.13.1):

$$\begin{aligned} K\mathbf{v} &= \nabla\mathbf{v} + (\nabla\mathbf{v})^{\mathrm{T}} \\ &= \frac{\mathbf{J}+\mathbf{J}^{\mathrm{T}}}{2} + \frac{\mathbf{J}-\mathbf{J}^{\mathrm{T}}}{2} + \frac{\mathbf{J}^{\mathrm{T}}+\mathbf{J}}{2} + \frac{\mathbf{J}^{\mathrm{T}}-\mathbf{J}}{2} \\ &= 2\mathbf{S}. \end{aligned} \tag{6.8}$$

Hence, this Killing energy measures the pointwise deviance of $\mathbf{v}$ from being an exact Killing vector field. For Equation (6.8) to be zero, i.e., the observer field to be perfectly Killing, the trace of the Jacobian has to be zero $\mathrm{trace}(\mathbf{J_v}) = \mathrm{div}(\mathbf{v}) = \mathbf{0}$. This means the observer field needs to be divergence-free, which is what we would expect from a vector field describing the motion of infinitely many rigid body observers. The second required property is that the upper triangular part of the Jacobian needs to be the negative of the lower triangular part, which is characteristic for rotation matrices. Thus, the Killing energy is a suitable measure for the rigid body motion of the observer vector field. To ensure uniqueness of the solutions of the minimization problem, the authors add a third regularization term. This term captures the desire of a small steady field $\widetilde{\mathbf{w}}$, by favoring observer velocity fields $\mathbf{v}$ that are similar to the input vector field $\mathbf{u}$. Combining these three constraints, the authors formulate the final minimization problem [Had*19, Sec. 5.2]

$$\min_{\mathbf{u}} \int_{\tau,\xi} (E_K + \lambda D_t + \mu R)(\mathbf{u},\xi,\tau)\,\mathrm{d}\xi\,\mathrm{d}\tau, \tag{6.9}$$

where $\lambda, \mu \in \mathbb{R}$ are weights, controlling the trade-off between rigid body observer motion and steadiness of $\mathbf{w}$, and the influence of the regularization term. The different terms are derived from the Killing energy, Lie derivative and the regularization

$$\begin{aligned} E_K(\mathbf{u},\xi,\tau) &:= \frac{1}{2}\|K\mathbf{u}(\xi,\tau)\|_F^2, \\ D_t(\mathbf{u},\xi,\tau) &:= \frac{1}{2}\left\|\frac{\mathscr{D}}{\mathscr{D}t}\mathbf{v_u}(\xi,\tau)\right\|_2^2, \\ R(\mathbf{u},\xi,\tau) &:= \frac{1}{2}\|\mathbf{v_u}(\xi,\tau)\|_2^2, \end{aligned} \tag{6.10}$$

with the Frobenius norm $\|\cdot\|_F$ and the 2-norm $\|\cdot\|_2$. A discretized solution may be found by a conjugate gradients squared methods like the *cgs* routine from the MATLAB software suit [MAT18]. The optimization of the observer field, as defined by Equation (6.10), is global, i.e., considering the entire domain at once. The significant computation cost is discussed in Section 8.4;

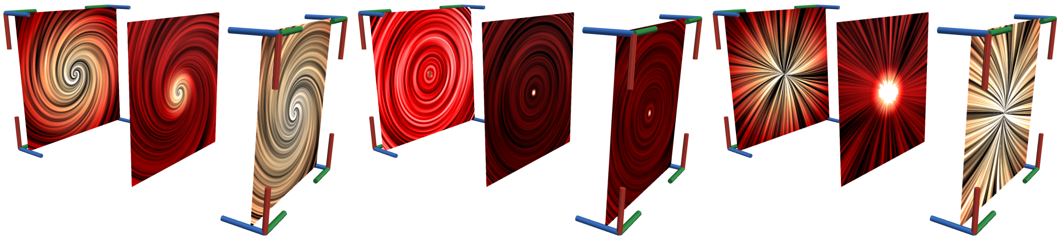

(a) Input $\mathbf{u}$ (b) $\mathrm{curl}(\mathbf{u})$ (c) $\mathrm{div}(\mathbf{u})$

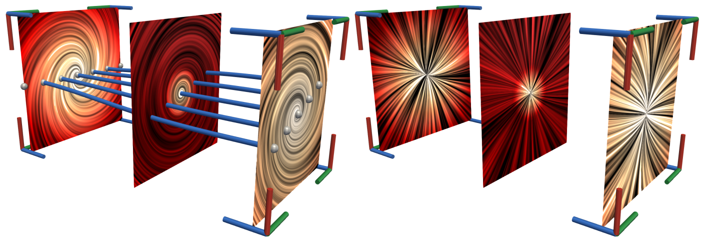

(d) $\mathbf{v}$ ([Had*19]) (e) $\mathbf{w}_r$ ([Had*19])

Figure 6.2: The original attracting vortex model within the space-time domain $D = [-1,1]^2 \times [0,4]$ (a). The steady-as-possible field as obtained by Hadwiger et al. [Had*19] (e). The remaining information is captured in the observer velocity field (d). Colored LIC of the respective fields at time steps $t = 0.1, 2.2, 3.9$ indicate velocity direction and magnitude. Observer world lines shown in blue.

6.3 Example: Attracting Vortex

Let us take a look at a simple example and see how these methods decompose the vector field into observer and steady-as-possible motion. To this end we construct a field that combines rigid body rotation and attracting behavior, i.e., rotating and diverging motion. From the construction of the methods from Hadwiger et al. [Had*19] and Günther et al. [GGT17] we expect the observer velocity field to capture the rotational motion and the steady-as-possible field to capture the diverging part. We define the model within the domain $D = [-1,1]^2 \times [0,4]$

$$\mathbf{u}(\mathbf{x}) = (t(1-d))(\cos(td)+1)\begin{pmatrix}\cos(\theta) & -\sin(\theta)\\ \sin(\theta) & \cos(\theta)\end{pmatrix}\begin{pmatrix}x\\ y\end{pmatrix}, \tag{6.11}$$

where the angle $\theta = \frac{\pi}{2}$, and $d = 0.9$. The first factor decreases the velocity magnitude of the vortex over time, and the second oscillates the magnitude. Figure 6.2 shows how the method of Hadwiger et al. decomposes the vector field.

7 Research Questions

Motivated by the recent developments in the field of frame-independent feature extraction we investigate the state-of-the-art techniques. 2017 Günther et al. [GGT17] presented a framework to enable existing vortex extraction techniques to become objective, i.e., invariant under rigid body motion of the observer. Shortly afterwards, in 2018 they introduced a revised version that includes invariance under affine observer transformations. Both methods build on a discrete neighborhood. Most recently, in 2019, Hadwiger et al. [Had*19] introduced a similar global technique without the need for a discrete neighborhood. We presented the techniques in Chapter 6.

The ability to view a time-dependent vector field in a steady frame, i.e., as time-independent, raises the question if we can extend steady vector field visualization techniques to the time-dependent case. In this chapter, we present a set of open research tasks that break this question down into two categories, which we answer in Chapter 8: 1) investigate the types of unsteady vector fields that can and cannot be steadified by these techniques (Questions Q.1 and Q.2), and 2) given a time-dependent field that can be seen as steady using one of the aforementioned approaches, evaluate and compare methods from steady and unsteady vector field visualization (Questions Q.3 and Q.4). Furthermore, we discuss theoretical limitations and describe the methodology used in Chapter 8 to investigate these tasks in practice. In the following chapters we distinguish the two frameworks, approximate observer Killing fields from Hadwiger et al. [Had*19] and the framework of Günther et al. [GGT17]. We further discern the framework of Günther et al., in the objective [GGT17] and the hyperobjective version [GT18a].

Q.1 Are the two frameworks of Hadwiger et al. [Had*19], and Günther et al. [GGT17; GT18a] able to compute frames of reference where general time-dependent vector fields appear steady?

Q.2 How do the two techniques of Hadwiger et al., and Günther et al. compare in:

 1 Quality of the computed steady frame,

 2 Physical interpretations,

 3 Computation times.

Q.3 Given a frame of reference in which an unsteady vector field appears steady:

 1 How do vortex region and vortex core line extraction methods translate from the steady frame to the time-dependent frame?

2 How does steady vector field topology in the steady frame compare to streak-based vector field topology in the time-dependent frame?

Q.4 How do the techniques of Hadwiger et al., and Günther et al. compare to other vector field decompositions, such as the Helmholtz-Hodge decomposition?

7.1 Steadification of General Vector Fields

This questions aims to assess the necessary properties that time-dependent vector fields have to have in order to be steadifiable by one of techniques from Hadwiger et al. [Had*19], and Günther et al. [GGT17; GT18a]. The approximate Killing vector fields approach [Had*19] and the objective version from Günther et al. [GGT17] limit observer motion to rigid body motion. They enforce this in different ways, i.e., the former trades similarity of nearby observers and steadiness of the resulting field, the latter strictly limits their local optimization by its construction. Finally, the hyperobjective framework from Günther and Theisel [GT18a], locally limits observer motion to affine transformations, including translation.

Generic Objective Vortices & Hyperobjective Vortices. As we discussed earlier in Section 6.1, the methods presented by Günther et al. [GGT17; GT18a] distinguish rigid body and affine observer motion. We exclude subclasses of rotation invariance and scaling invariance within their framework, because they are sufficiently included in the objective and hyperobjective proposals, respectively. According to Hadwiger et al. [Had*19] rigid body observer motion implies that the Jacobian of the observer velocity field has the form:

$$\mathbf{J_v} = \begin{pmatrix} 0 & x_{1,2} & \cdots & x_{1,n} \\ -x_{1,2} & 0 & x_{i,j} & x_{2,n} \\ \vdots & -x_{i,j} & 0 & \vdots \\ -x_{1,n} & -x_{2,n} & \cdots & 0 \end{pmatrix}. \tag{7.1}$$

This incorporates two properties of the observer field 1) it is locally divergence free, and 2) represents local rigid body rotations. In this case, we would expect that any field that can be decomposed into a time-dependent divergence free component and a steady component, can be steadified by this approach.

The extension to hyperobjective observers [GT18a] imposes even less restrictions on the observer velocity field, where the Jacobian is only required to be invertible. We thus expect this to be able to steadify most time-dependent vector fields.

Approximate Observer Vector Killing Fields. In their approach Hadwiger et al. balance locally rigid body motion of the observer field and steadiness of the observed field. The former is again captured in the Jacobian of the observer velocity field as in Equation (7.1). However, since the computation of the final observer velocity field $\mathbf{v}$ is a trade-off between these properties and the steadiness of the observed field $\mathbf{w}_r$, the resulting observer field does not need to exactly represent Equation (7.1). Therefore, similar to the technique of Günther et al. [GGT17], we expect this approach to be able to steadify fields that can be decomposed in a time-dependent divergence free component and a steady component. This method additionally provides us with the option to favor either property over the other one by adjusting the respective weights.

Methodology To evaluate our expectations, we test all three methods on analytical fields where we expect them to find a suiting frame of reference and on analytical fields where we expect them to fail. We have seen that all three techniques are able to steadify a field representing rigid body motion with added oscillating divergence, compare Section 6.3. For the second test, we use a saddle-node bifurcation, i.e., the birth of two critical points with opposite Poincaré-Hopf index (Section 5.1.2). In the case of the death of two critical points, the two points approach each other. Since moving critical points can be achieved by simply adding a constant to the vector field, it is evident that these techniques are able to counteract this approaching motion. However, in order to steadify a saddle-node bifurcation, the observer vector field needs to incorporate it. Locally, saddle-node bifurcation are highly non-linear which cannot be represented by (locally) rigid-body or affine motion. Remark that although all three techniques allow the observer vector field to be non-linear in time, the spatial neighborhood in all cases is linear. Hence, we expect neither of the three, to extract bifurcations from the original field, and they are thus present in the steady-as-possible field. An argument can be made for the framework of Hadwiger et al. [Had*19]: there we may manipulate the weights so that perceived steadiness has magnitudes more influence on the result than local rigid body motion. In order to use the steady-as-possible field for visualization we need it to carry most of the relevant information of the original field. Manipulating the weights in such a way, waive any interpretation of the observer field as the motion of observers and severely limits the conclusion we can draw from the steady-as-possible field. Let us consider a hypothetical technique that is able to extract saddle-node bifurcation while retaining the steadification properties of the aforementioned mentioned ones. In case of a saddle-node bifurcation this implies that either the steady-as-possible field has no critical points at all, or that two exist at all times. In both scenarios essential information of the original field is carried by the observer vector field and it may therefore not be disregarded in the visualization process, which defeats the goal of the techniques in question. In addition, we consider Hopf bifurcations, where a critical point changes stability via a pair of purely virtual eigenvalues of its Jacobian. During this process a limit cycle is born, expanding outward from the bifurcation location. Since the number of critical points does not change, and the fact that a limit cycle is represented by a periodic orbit, the reasoning from saddle-node bifurcations cannot be directly transferred. However, remarks concerning the loss of information in the case the limit cycle is represented in the observer field are equally valid here. The global

Bifurcation Type	No	Saddle-Node	Hopf
Hadwiger et al. [Had*19]	✓	×	(✓)
Günther et al. [GGT17]	✓	×	×
Günther and Theisel [GT18a]	✓	×	(×)

Table 7.1: Expected results for steady-as-possible field.

nature of the approach of Hadwiger et al. [Had*19] could allow the observer field to consume the limit cycle, because it only requires slight local deviation from strict rigid body motion. With decreasing weight of similar observers, a limit cycle can be integrated into the observer field. In case of the objective approach of Günther et al. [GGT17] this is not true. This is especially true because in order to represent global phenomena like limit cycles, the rigid body neighborhood size needs to adapt to the increasing size of the phenomenon, a contradiction to the construction of the method. The argument also holds for the hyperobjective version. However, small neighborhood sizes may allow the observer field in this case to approximate a limit cycle using shear flow. Table 7.1 summarizes these theoretical considerations.

We further evaluate these techniques on three real-world datasets. The first, a simulated von-Kármán vortex street, only exhibits isolated critical point bifurcations, while the latter two include turbulent fluid motion. Hence, all three approaches should work well on the first dataset. The latter two examples include fold and Hopf bifurcations, thus we expect none to prevail. Chapter 8 discusses results and influence of bifurcation on overall feature extraction in steady-as-possible fields.

7.2 Comparison of Local Frame of Reference Techniques

While the first questions addressed issues concerning the steadiness of the observed field, this question is mainly concerned with the comparison of the two frameworks. The key difference is the local character of the methods by Günther et al. [GGT17; GT18a] and the global optimization used by Hadwiger et al. [Had*19].

7.2.1 Quality of Computed Frame of Reference

This specifically focuses on the chosen size of neighborhood within the framework of Günther et al. As Hadwiger et al. [Had*19] showed in the original paper, the existence of a discrete neighborhood leads to distortions given oscillating magnitude of observer motion. Together with Question Q.3 we investigate how these distortions effect feature extraction in the observed field. We furthermore, evaluate smoothness and continuity of the observed field depending on the input vector field. While the analytical examples exhibit coherently sized features, the simulated datasets include features of varying sizes. Here, the global optimization of Hadwiger et al. [Had*19] is expected to yield superior results compared to the local approaches by Günther et al. [GGT17; GT18a]. For each dataset we use both methods with multiple neighborhood sizes and study the results.

7.2.2 Physical Interpretation

Each of the aforementioned approaches limits observer motion. The motivation behind this is to ensure the interpretability of the observer and the observed vector field. In case of the objective framework [GGT17], an observer is associated with each point in space. Every individual observer is limited to rigid body motion within its neighborhood, therefore, we can view this as a camera moving with the flow. However, since the connection between individual observers is waived, the observed field represents the combined view of the cameras suspended in the flow, which are not necessarily coherent. The size of the discrete neighborhood, corresponding to the field of view of the different observers, can serve as an indirect link between observers. Due to the weak nature of this tie, it is likely that turbulence in the flow dominate the form of the observed field. Furthermore, the premise of the size of the neighborhood is that the original vector fields behaves coherently within regions of this size. This requires a priori knowledge, e.g., the size of a vortex which is to be extracted. We will see that this is no trivial task given more complex real-world datasets (Sections 8.3.2 and 8.3.3).

The hyperobjective fr§amework suffers from the same issues concerning the discrete neighborhood. In addition, the interpretation of observer motion is waived almost completely, since the authors only require that no information is lost, i.e, the Jacobian of the observer field is invertible. Günther and Theisel [GT18a] argue that this step is necessary to allow adaption of the observer field to two phenomena 1) growing vortices, and 2) shear flow, e.g., at the boundary of a tube. Although both mentioned scenarios are valid, this approach does not allow any general interpretation of the observer motion. Instead, in each case the observer velocity field needs examination in order to interpret the results obtained using the observed field.

Concerning the interpretation of the method by Hadwiger et al., we know from Chapter 3 that a single global observer restricted to rigid body motion can be seen as a camera rotating and translating along observer world lines, i.e., pathlines of the observer field. The only information contained by such an observer are continuous rotation and translation of the entire domain. The approximate Killing vector field approach [Had*19] tries to incorporate this view and balances it against the steadiness of the observed field, i.e., neighboring observers represented by this technique are modeled as similar as possible. Depending on the distortions within the observer field, we may interpret this as seeing the time-dependent flow through a lens that is (slightly) distorted in certain local regions. However, we argued earlier that the weights allow us to balance rigid body observer motion and steadiness, thereby increasing distortions to allow for a less time-dependent observed field. Therefore, the deviation from a single global observer needs to be taken into account when the observed field is analyzed. In this sense, the approach by Hadwiger et al. is a good trade-off between these properties. Although it comes with a heavy increase in computation time since it requires a global optimization.

7.2.3 Computation Time

Question Q.2.2 mentions drawbacks of the local character of the method by Günther et al. However, compared to the global optimization required by Hadwiger et al. [Had*19], this limitation significantly improves computation times. Both teams have included a performance analysis in their original proposal. We build on these results and compare them side-by-side on all datasets used for the evaluation later on. The local approaches of Günther et al. [GGT17; GT18a] are easily parallelizable since the optimization for each point is independent. The memory requirements are moderate since only matrices containing the local neighborhood are needed at a time, of course increasing with the number of parallel nodes treated. Therefore, these approaches are mainly CPU bound. A parallel GPU implementation could improve computation times. However, matrix decompositions are known to be taxing for parallel GPU computation and do not offer large speedups as it is the case in other applications, i.g, FTLE computation. The complexity class depends on the matrix decomposition used, e.g, QR or Householder. For regular grids, linear complexity in the number of grid nodes may be achieved using summed area tables.

Hadwiger et al. [Had*19] require global optimization over the entire space-time domain. For the construction of the minimization problem, matrices of the size $3N \times 3N$, with N being the number of nodes in space-time, are needed. Even when using sparse matrices, the memory demand is considerable. The authors included a proof-of-concept implementation which uses only a single thread to optimize this large system. We have both implemented a parallelized CPU version and GPU version. This further raises memory requirements to the point that even moderate datasets cannot be computed in parallel. The issue is elevated on GPUs where the available memory, even on modern graphics cards, is very limited. Therefore, we found that none of the parallel implementation is suitable for large datasets.

7.3 Transfer of Methods from Steady to time-dependent Cases

In the following, we address the most prominent implications of these techniques. Given these methods can find a steady frame of reference for a specific vector field, are we able to transform methods from steady vector field visualization to the time-dependent case. As we argued in Chapter 6, the driving force behind these techniques was the search for vortex extraction methods, first for steady, later for time-dependent vector fields. Thus, we first evaluate the applicability of vortex core extraction in steady-as-possible field before we move on to vector field topology.

7.3.1 Time-Dependent Vortex Extraction

The authors of both frameworks [GGT17; GT18a; Had*19] evaluated their techniques using vortex core extraction for both analytical and simulated datasets. We confirm their findings and extend the analysis to fluid simulations including turbulent regions. It is of special interest how vortices of different sizes are captured by the techniques of Günther et al. [GGT17], depending on the neighborhood size.

7.3.2 Time-Dependent Vector Field Topology

The positive results for vortex core extraction raise the question what other techniques may be transferred to the time-dependent realm. When steady vector field topology was first proposed [HH91], the authors remarked that these techniques need to be applied in a suiting frame of reference. This begs the question if we may be able to apply steady vector field topology in the steady frame and infer topological structures for the original time-dependent field from there.

Hypothesis 7.1. Steady vector field visualization techniques applied to the steady-as-possible field transfer to the time-dependent case when the observed field is steady.

This captures our intuition about the frameworks of Hadwiger et al. [Had*19] and Günther et al. [GGT17; GT18a]. And as long as the observed field is steady we may directly employ Equation (3.14) to see that this holds. However, the more interesting question this raises is: How does this translate to cases with increasing time-derivative of the steady-as-possible field? To investigate, we compare vector field topology extracted using this approach and the current state-of-the-art approach, streak-based vector field topology to a variety of datasets in Chapter 8.

Hyperbolic Trajectories Streak-based vector field topology is based on the extraction of hyperbolic trajectories and their invariant manifolds. We have seen earlier (Section 5.2) that the extraction of hyperbolic trajectories using FTLE ridges associated with high computational cost, and the extraction using the parallel vectors operator requires fitting of the raw solutions to a bifurcation line. Haller [Hal00] proposed to define hyperbolic trajectories as trajectories that are, for locally the longest time, hyperbolic. We could also think of hyperbolic trajectories as the trajectories that locally exhibit strongest hyperbolicity. It is still an open research topic whether these two definitions coincide and how they compare to intersections of forward and backward LCS. Sadlo and Weiskopf [SW10] argued that saddle-type critical points in steady vector field topology should be replaced by hyperbolic trajectory when moving to the time-dependent case. Thus, a natural interpretation may suggest that these two coincide when viewing the time-dependent vector field in the steady frame. In this context it is unclear what saddle-type critical points in the steady-as-possible field reveal about the behavior of the original field, whether they coincide with any of the aforementioned definitions. We evaluate saddle-type critical points in the steady-as-possible field and their relation to LCS intersections as well as bifurcation lines and their raw solutions in space-time. In order to investigate the interplay of these definitions, we establish that straight hyperbolic trajectories may be extracted using saddle-type critical points in the steady frame. We further analyze curved hyperbolic trajectories, and compare the methods in general settings.

Hypothesis 7.2. Critical points in the steady-as-possible field coincide with PV of the original field and the observer velocity field.

Critical points in the steady-as-possible field imply that along the observer world line corresponding to this point, the original vector is the same as the observer vector. We prove this fact in Section 8.1.1 and use the result extract vortex cores lines and hyperbolic trajectories.

Hypothesis 7.3. The paths of objective critical point transformed to the original field, are not necessarily pathlines of the original field.

The argument for this is the same as for parallel vectors in general, where the parallelism $\mathbf{u} \parallel \mathbf{J_u u}$ does not imply that solutions are streamlines of $\mathbf{u}$. Furthermore, following the reasoning of Machado et al. [Mac*16], solutions obtained by PV need to be fitted to characteristic curves of the original vector field. Therefore, we propose to fit raw solutions for hyperbolic trajectories obtained by the trajectory of objective saddle-type critical points in the steady-as-possible field to nearby streamlines. This can be achieved by the algorithm presented by Machado et al. [Mac*16].

Separatrices and Lagragian Coherent Strucutres The invariant manifolds of a hyperbolic trajectory can be found by seeding generalized streak lines along it. Sadlo and Weiskopf [SW10] showed that these converge toward LCS in forward and backward time, and the authors exploit this fact to extract the separating structures of time-dependent flow fields. The extraction of invariant manifolds is not subject to the same difficulties than the extraction of hyperbolic trajectories, since the LCS are attracting in either forward or reverse time. Thus, generalized streak lines are a computationally cheap and accurate way to extract these structures, given a hyperbolic trajectory has been found previously. If saddle-type critical points in the steady frame indeed can be used to obtain hyperbolic trajectories, we would expect that separatrices can be used to find its invariant manifolds. However, there is a caveat related to the local fitting of reference frames. Namely, the local frame of reference that reveals the saddle-type critical point is only valid in the vicinity of this point, depending on the similarity of nearby observers. Meaning, the further we integrate separatrices in the steady frame the less an observer following the saddle-type critical points characterizes the separatrix.

Hypothesis 7.4. Separatrices from the steady-as-possible field translate to the original field when the frame transformation is the one of a single global observer.

If a global frame of reference exists that shows the vector field as steady, separatrices should coincide with LCS in the time-dependent frame. The stronger the observer velocity field deviates from the motion of a single global observer the less meaningful are separatrices in the steady frame for the time-dependent case. In general, the approach by Hadwiger et al. [Had*19] has an advantage since the authors explicitly searches for observers that are as similar-as-possible.

7.4 Relation to Vector Field Decompositions

This question is more of theoretical nature and will mainly be discussed in the following. Vector field decompositions have previously been used to characterize vector fields in different frames of reference [Bha*13; Bha*14; BHJ16; BPB14]. We discussed common decompositions, such as Helmholtz-Hodge (HHD), in Section 2.13. All three methods aim to essentially decompose the vector field into two components, a time-dependent part limited to rigid body or affine motion, and a steady-as-possible part including everything else. The construction used by Hadwiger et al. [Had*19], i.e., trade-off between local rigid body motion and steadiness and the existence of a regularization term, guarantees uniqueness of the solution. Where the regularization term forces the field to be as similar-as-possible to the original field. The first part of the optimization may be substituted by other restrictions modeling observer motion, e.g., a divergence or curl energy. However, the framework of Günther et al. [GGT17; GT18a] only balances these properties and no regularization term is present. Although the authors argue that they have not encountered any cases where this method did not provide a unique solution, in theory it is not unique.

8 Evaluation

In this chapter, we investigate our theoretical predictions from Chapter 7. We introduce analytical models for 2D time-dependent velocity fields, as well as datasets obtained by simulation. The different nature of the two main phenomena in question, vortex core lines and hyperbolic trajectories, require distinct examination on suiting vector field models. Hence, we split our analysis in two parts: 1) analysis on small analytical examples, 2) application to real-world datasets. The former validates our theoretical reasoning from Chapter 7. We then move on to discuss the impact of major flow events on the ability of the frameworks in question to compute locally steady frames of reference. With this, we turn to their effect on feature extraction in simulated datasets and provide context for the specific problems discussed earlier. Finally, we bring our observations from analytical and real-world datasets in context with our theoretical predictions from Chapter 7.

Notation We repeatedly refer to the different vector fields that occur in the frameworks of Hadwiger et al. [Had*19] and Günther et al. [GGT17; GT18a]. Therefore, we list common labels for each of them here. The original vector field $\mathbf{u}$ is the observed field with the so-called lab frame of reference. Sometimes referred to as the field in the time-dependent or unsteady frame. Secondly, when we introduce other observer we describe their relative motion to the lab frame by pathlines of the observer velocity field $\mathbf{v}$. Also called ambient flow. From these two fields we construct the field $\widetilde{\mathbf{w}} = \mathbf{u} - \mathbf{v}$, which represents the steady-as-possible field within the original frame of reference. This field is still time-dependent and loci within this field correspond directly to loci within the original field. Since it carries equivalent information as the steady-as-possible field $\mathbf{w}_r$, it is also called observed field. And lastly, the observed field $\mathbf{w}_r$ in the transformed frame of reference. It is obtained by transforming $\widetilde{\mathbf{w}}$ according to the observer motion described by the observer field $\mathbf{v}$. By references to the steady-as-possible, or just steady field, we mean the $\mathbf{w}_r$ field. Unless otherwise specified, we use the $\widetilde{\mathbf{w}}$ and $\mathbf{w}$ interchangeably.

8.1 Analytical Models

The following analytical models treat different phenomena discussed earlier (Chapter 7). Namely, vortex core/vortex region criteria and vector field topology. We further distinguish models using a single global observer and models that locally transform the original vector field. The former includes a vortex model seen through

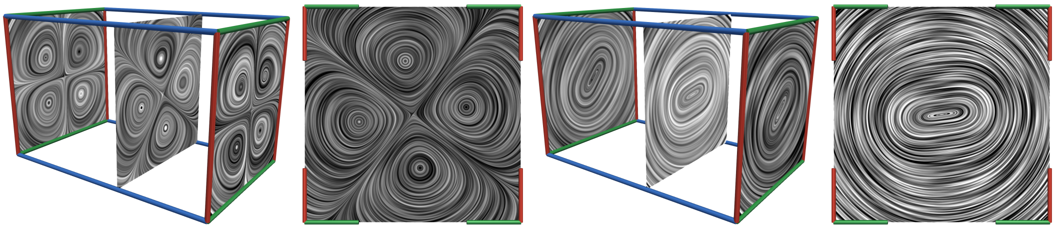

(a) SC Space-Time (b) SC (c) PC Space-Time (d) PC

Figure 8.1: The streamline (SC) and pathline (PC) core versions of the four centers model within the domain $D = [-2, 2]^2 \times [0, 2\pi]$. Both variants, SC (a) and PC (c), depicted in space-time with LIC at time steps $t = 0, \frac{6}{5}\pi, 2\pi$. Instantaneous versions at time $t = \frac{6}{5}\pi$ of both SC (b) and PC (d).

the eyes of a continuously rotating observer, a linearly moving and a rotating saddle-type critical point. The latter is illustrated by the quad gyre model [SLM05], where four gyres oscillate from left to right and introduce shear at the domain boundaries.

8.1.1 Four Rotating Centers

The four centers model [GST16] captures the fluid movement of four centers rotating around each other. There exist two different versions. The first exhibits four streamline cores (SC), i.e., slices in space-time reveal four stream line vortex cores. The second version, exhibits four pathlines cores (PC) and represents the SC model in a rotated frame. Figure 8.1 illustrate these differences. Note, that streamlines of the PC version do not reveal any vortex cores (Figure 8.1d).

Four Centers (SC) This model is constructed from the scalar field [GST16]

$$f(\mathbf{x}) = 3xy \cdot e^{-\mathbf{x}^2 - \mathbf{y}^2}, \tag{8.1}$$

where $\mathbf{x} = (x, y)^{\mathrm{T}} \in D \subset \mathbb{R}^2$, with $D = [-2, 2]^2$. The streamline (SC) version is then obtained by continuously rotating the scalar field, c.f. Figures 8.1a and 8.1b

$$\begin{aligned} \mathbf{u}(\mathbf{x}', t) &= \begin{pmatrix} \frac{\partial}{\partial y} f(x', y') \\ -\frac{\partial}{\partial x} f(x', y') \end{pmatrix}, \\ \text{where} \quad \begin{pmatrix} x' \\ y' \end{pmatrix} &= \begin{pmatrix} \cos(t) & \sin(t) \\ -\sin(t) & \cos(t) \end{pmatrix} \begin{pmatrix} x \\ y \end{pmatrix}. \end{aligned} \tag{8.2}$$

Four Centers (PC) The pathline (PC) version describes four pathline cores rotating around each other. They originate from the mutual cancellation of vortices

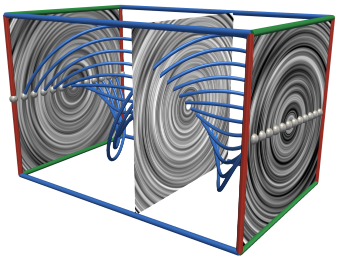

(a) Hadwiger et al.

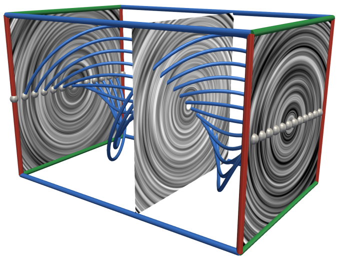

(b) Günther et al.

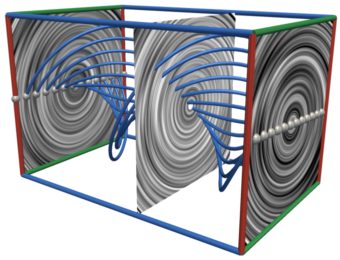

(c) Günther and Theisel

Figure 8.2: Observer velocity fields according to Hadwiger et al. [Had*19] (a), Günther et al. [GGT17] (b), and Günther and Theisel [GT18a] (c). Observer world lines of 13 observers with $r = 0$ in blue.

when rotating with the frame of references, i.e., following the path of the streamline vortices. Figures 8.1c and 8.1d illustrate.

$$\mathbf{u}(\mathbf{x}', t) = \begin{pmatrix} -x' \cdot e^{-x'^2 - y'^2}(2y'^2 - 1) \\ -y' \cdot e^{-x'^2 - y'^2}(2x'^2 - 1) \end{pmatrix}, \tag{8.3}$$

where (x', y') are obtained from the rotating coordinate frame, i.e., using Equation (3.3) and the rotation of the frame is given in Equation (8.2). This means, we expect the PC version in the objective frame of reference to resemble the streamline version of the model. For the visualization of the steady-as-possible field we will typically use the space-time view of the $\mathbf{u_v} = \mathbf{u} - \mathbf{v}$ field, since it carries equivalent information as the steady-as-possible field $\mathbf{w}_r$ but the domain is not transformed, and vortex cores, as well as other features, extracted in $\mathbf{u_v}$ need not be transformed back and may be used directly.

Using the observer motion depicted in Figure 8.2, we can transform the PC version back into the original frame of reference. Figure 8.3c shows that the observed field $\mathbf{u_v}$ indeed resembles the SC version of the model. The extracted vortices, depicted as blue and red spheres where color indicates stability, can be used to find vortex core lines in the original field. This can be achieved by a number of ways:

1. Parallel vectors operator of vortex detectors applied in space-time to the $\mathbf{u_v}$ field, e.g. the Sujudi and Haimes criterion $\mathbf{u} \parallel \mathbf{J_u u}$. Since the $\mathbf{u_v}$ field is objective, any vortex extractor applied here, yields objective vortex cores. However, possible issues with curved core lines (Section 4.2.2) persist. Note that the application of the PV operator in space-time implies not only parallelism of the two fields but requires them to be equal (Equation (4.11)).

2. View the field in the steady frame.
    a) Extract critical points of $\mathbf{w}_r$.
    b) Transform the locations back to the original frame using Equation (3.14).

3. Parallel vectors of the original field $\mathbf{u}$ and the observer velocity field $\mathbf{v}$.

Parallel vectors in steady 2D vector fields extract critical points. Hence, parallel vectors in $\widetilde{\mathbf{w}} = \mathbf{u}_{\mathbf{v}}$ coincide with critical points in $\mathbf{w}$ if $\mathbf{w}$ is steady. This implies the equivalence of methods (1) and (2). We can argue that methods (2) and (3) are equivalent. As we noted in Section 4.2.2, the application of the PV operator in space-time implies that both fields are not only parallel but equivalent. Then, there exists a critical point in $\mathbf{u}_{\mathbf{v}}$ where $\mathbf{u}'(\mathbf{x}, t) \parallel \mathbf{v}'(\mathbf{x}, t)$, and with that a critical point exists at the corresponding location in $\mathbf{w}_r(\mathbf{x}^*)$.

$$\mathbf{u}'(\mathbf{x}, t) \parallel \mathbf{v}'(\mathbf{x}, t) \Leftrightarrow \mathbf{u}(\mathbf{x}, t) = \mathbf{v}(\mathbf{x}, t) \Leftrightarrow \mathbf{u}_{\mathbf{v}}(\mathbf{x}, t) = \mathbf{0} \Leftrightarrow \mathbf{w}_r(\mathbf{x}^*) = \mathbf{0}. \tag{8.4}$$

Conversely, a critical point in $\mathbf{w}_r$ implies a critical point in $\mathbf{u}_{\mathbf{v}}$, where the original fields are equivalent $\mathbf{u} = \mathbf{v}$, and thus parallel in space-time. This proves Hypothesis 7.2. The large feature angle in Figure 8.3a shows that vortex core lines extracted from the original field are false positives, and indeed, streamlines seeded around these false positives diverge, c.f. Figure 8.3b. Vortex core lines in Figures 8.3c and 8.3e were obtained using PV of the original and the observer field (3). The angle between the feature tangent and the original vector field is small ($< 3°$), indicating that the core lines are streamlines of the original field. We can further analyze the quality of the core lines by seeding streamlines in the space-time domain offset from the extracted core line. Figures 8.3d and 8.3f show that streamlines stay close to the extracted core line. Note, the core lines in Figures 8.3d and 8.3f were obtained using critical points in the steady frame (2). Since the steady-as-possible field is indeed steady in this case, our argument from Equation (8.4) holds, and Figure 8.3 shows that the solutions are identical up to numerical precision.

Question Q.1: Steadification As expected (Hypothesis 7.1), the single global rotation of four centers PC version is accurately extracted by all three approaches. Figure 8.2 shows that the observer velocity fields of the three methods are almost identical, and Tables 8.3 and 8.4 show low residuals. Note, the residual in case of Hadwiger et al. [Had*19] is of global nature and in the case of Günther et al. Günther et al. [GGT17; GT18a] of local nature. Therefore, the two cannot be compared directly. Nonetheless, on their own, they indicate time-dependence of the respective steady-as-possible field sufficiently well.

Question Q.2: Comparison The depicted feature angles (Figures 8.3c and 8.3e) for the approaches of Hadwiger et al. [Had*19] and Günther and Theisel [GT18a] are within a similar range $< 3°$. However, the first and last frame of hyperobjective method shows slight distortions (Figures 8.3e and 8.3f). Additionally, the observed field $\mathbf{w}_r$ includes noise, revealed by additional critical points, compare Figure 8.3e. They arise near the boundary where the discrete neighborhood includes the domain boundary. Depending on the neighborhood size and employed method, computation

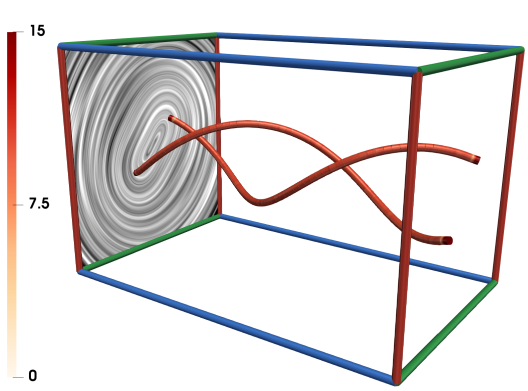

(a) Vortex Core Lines $\mathbf{u} \parallel \mathbf{a}$

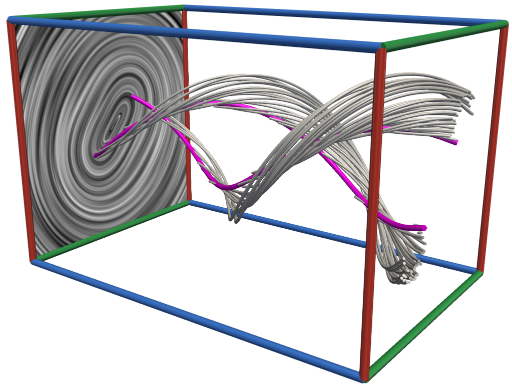

(b) Vortex Core Lines with Streamlines $\mathbf{u} \parallel \mathbf{a}$

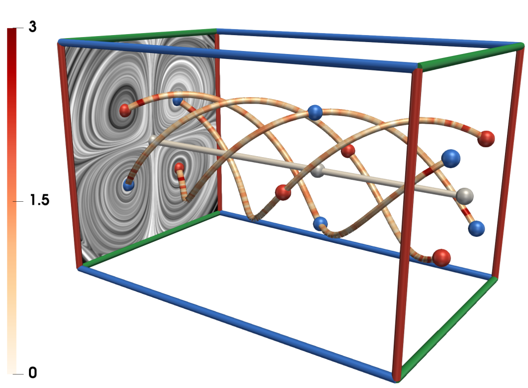

(c) Vortex Core Lines [Had*19]

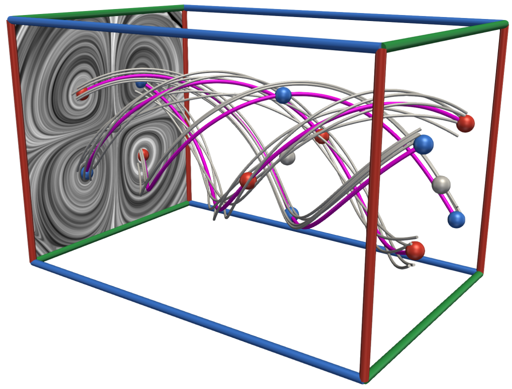

(d) Vortex Core Lines with Streamlines [Had*19]

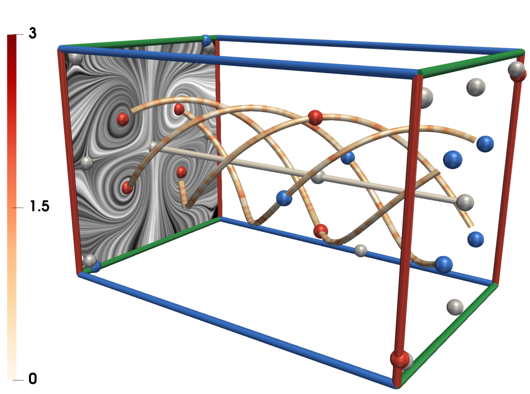

(e) Vortex Core Lines [GT18a]

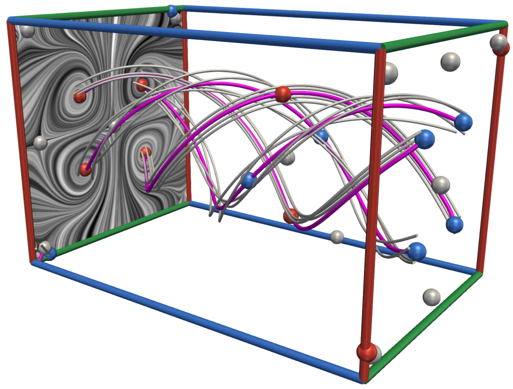

(f) Vortex Core Lines with Streamlines [GT18a]

Figure 8.3: Vortex core lines according to Sujudi and Haimes [SH95b] in the original field (a), and in the steady-as-possible field from Hadwiger et al. [Had*19] (c), and Günther and Theisel [GT18a] (e). Corresponding streamlines seeded along extracted core lines (b),(c), and (f). The feature angle between core line and vector field is color coded. LIC of the initial time-step shows slight distortions present in the first and last step in the steady field computed by Günther and Theisel [GT18a]. Additional detected critical points, stable (blue), unstable (red), saddle (grey), compared to the method of Hadwiger et al. [Had*19] are visible (f).

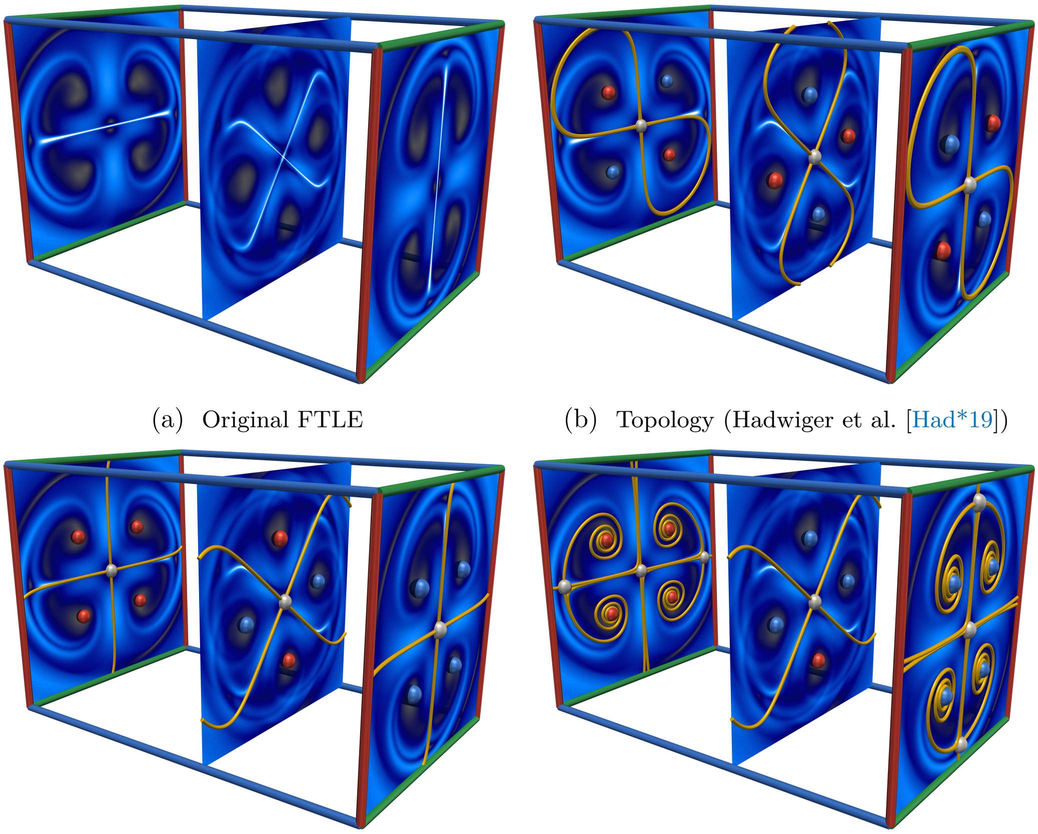

(a) Original FTLE

(b) Topology (Hadwiger et al. [Had*19])

(c) Topology (Günther et al. [GGT17])

(d) Topology (Günther and Theisel [GT18a])

Figure 8.4: Critical points (spheres) and FTLE of the original four centers PC model. Forward FTLE at $t = 0$ with advection time $T = 8$, superimposed forward and backward FTLE at $t = 3.789$ and $T = \pm 8$, and backward FTLE at $t = 4$ and $T = -8$. (a). Steady vector field topology applied in the steady frame of reference transformed back to the original domain: According to Hadwiger et al. (b), Günther et al. (c), and Günther and Theisel (d).

times of the discrete methods are a magnitude lower than the ones of the global approach (Tables 8.3 and 8.4).

Question Q.3: Transfer of Methods As Figure 8.3 illustrates, all three methods are able to accurately extract the four vortex core lines. The extracted core lines differ very slightly, but are overall in accordance with streamlines seeded around them. Application of steady vector field topology in the steady frames of reference computed by the different techniques reveal that the hyperbolic trajectory in the center is accurately extracted by all of them, c.f. Figure 8.4. The separatrices obtained by the method of Hadwiger et al. [Had*19] and the objective method of Günther and Theisel [GT18a] coincide in the vicinity of the hyperbolic trajectory

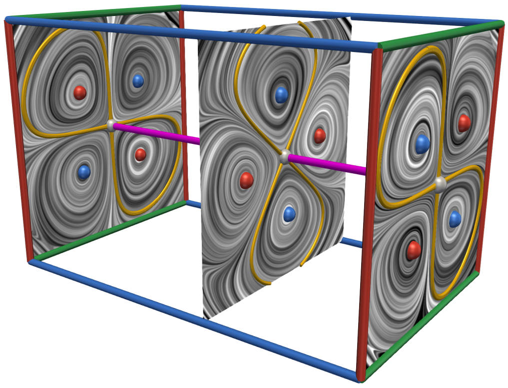

(a) Topology (Hadwiger et al. [Had*19])

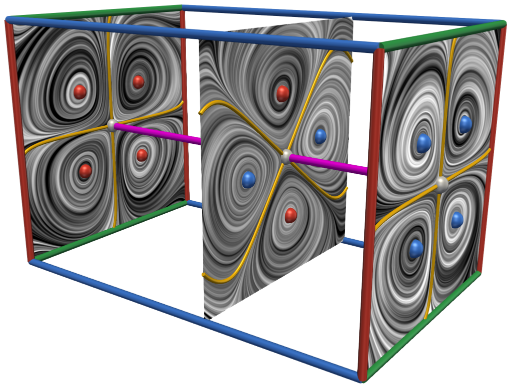

(b) Topology (Günther et al. [GGT17])

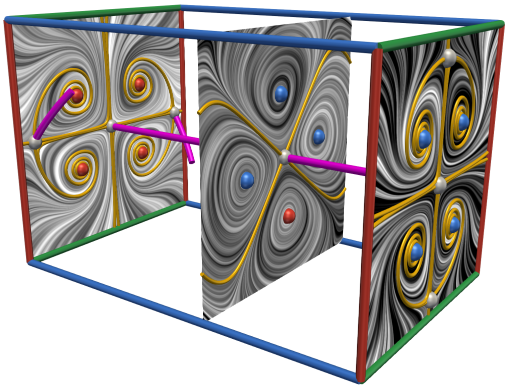

(c) Topology (Günther and Theisel [GT18a])

Figure 8.5: Corresponding observed fields $\mathbf{w}_r$ from Figure 8.4.

(Figure 8.5). Further away from the saddle-type critical point, they start to diverge and the FTLE ridges start to fade. Notice that the integration time of the FTLE is longer than the time domain of the dataset. However, since the model is time-periodic we may integrate longer by wrapping the time domain. Figure 8.6 shows forward FTLE at $t = 0.698$ with a longer advection time of $T = 16$. Trajectories seeded near the center (green) diverge and trajectories seeded further away (blue) do not diverge within the original time domain $[0, 4]$. This suggests, that separatrix integration in the steady reference frame need to stop when the respective time boundaries are hit. Keep in mind that the stable and unstable manifolds are computed in forward and reverse time, respectively. Machado et al. [Mac*16] suggested that FTLE ridges that are not sufficiently sharp could be false positives, which is what may be happening here as well.

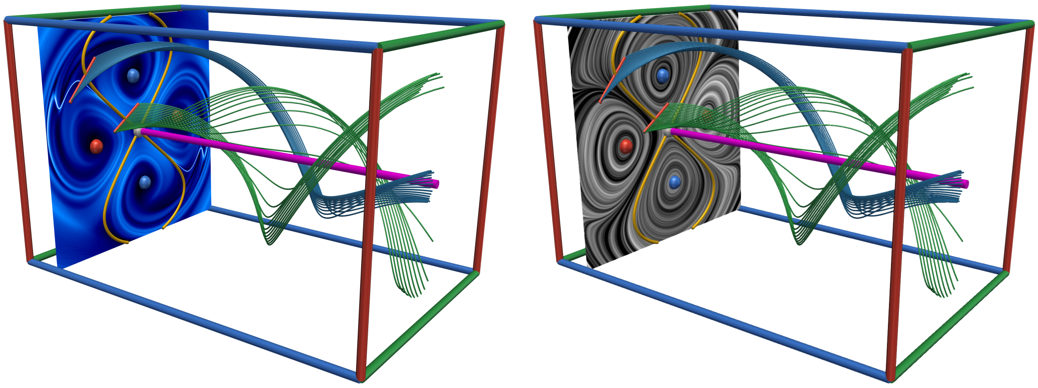

(a) Original FTLE (b) Topology (Hadwiger et al. [Had*19])

Figure 8.6: Forward FTLE at $t = 0.698$ with $T = 16$ and wrapped time boundaries to allow for longer advection times (a). Steady vector field topology computed by Hadwiger et al. [Had*19]. Pathlines of the original field (green and blue) seeded across FTLE ridges near the center are separated within the time domain $[0, 4]$. Pathlines seeded further outside are no longer separated.

8.1.2 Gyre Saddle Models

The gyre-saddle model was introduced by Sadlo and Weiskopf [SW10] with the objective to portrait a hyperbolic trajectory, which exhibits very sharp FTLE ridges, in various settings. We employ different versions to study hyperbolic trajectories and observer dependent extraction methods. The original example is defined as follows, let the vector field within the region $D = [-\frac{1}{2}, \frac{1}{2}]^2$ be

$$\mathbf{u}(\mathbf{x}) = \begin{pmatrix} -\sin(\pi x)\cos(\pi y) + a\sin(\pi y)\cos(\pi x) \\ \sin(\pi y)\cos(\pi x) - a\sin(\pi x)\cos(\pi y) \end{pmatrix}, \tag{8.5}$$

and outside this region

$$\mathbf{u}(\mathbf{x}) = \begin{pmatrix} kac(\pi x - a\pi(y - \frac{k}{2})) - lc(\pi y - a\pi(x - \frac{l}{2})) \\ kc(\pi x - a\pi(y - \frac{k}{2})) - lac(\pi y - a\pi(x - \frac{l}{2})) \end{pmatrix}, \tag{8.6}$$

where a controls the shear of the saddle and the functions

$$\begin{aligned} k =& \begin{cases} 1, & \text{if}((y \geq |x|) - (y \leq -|x|)(\\ 0, & \text{otherwise} \end{cases} \\ l =& \begin{cases} 1, & \text{if}(x > |y|) - (x < -|y|) \\ 0, & \text{otherwise} \end{cases} \\ c(x) =& \begin{cases} 1, & \text{if } -\frac{\pi}{2} \leq x \leq \frac{\pi}{2} \\ 0, & \text{otherwise} \end{cases} \end{aligned} \tag{8.7}$$

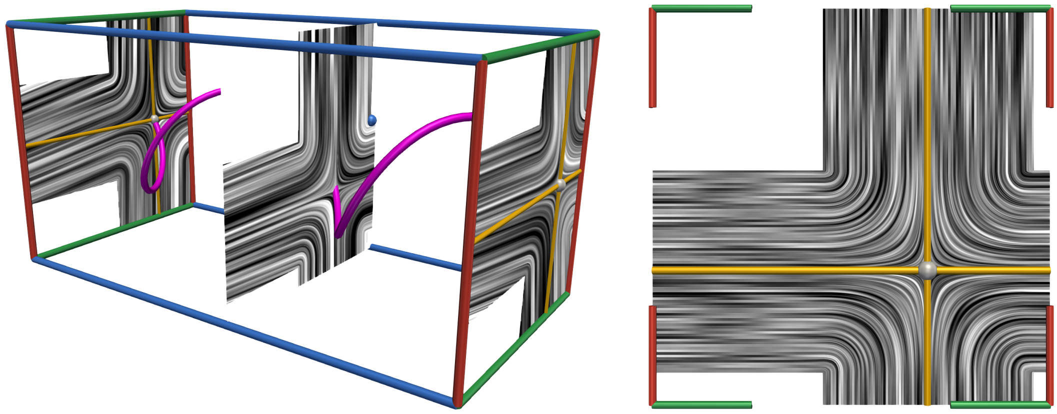

(a) Rotating Gyre Saddle LIC (b) Time-Slice at $t = 2.2$

Figure 8.7: Rotating gyre saddle within the domain $D = [-1, 1]^2 \times [0, 4]$, depicted in space time (a) together with three time-slices at times $t = 0, 2.2, 4$. The instantaneous vector field at these times is visualized as LIC. The curved trajectory of the saddle point (pink), is used to compute instantaneous invariant manifolds (yellow). Here, a single rotation is completed over a time of 2π, i.e., $\alpha = 1$. The time slice at $t = 2.2$ shows the saddle rotates over time, but otherwise retains its form (b).

Linear Saddle From the above model, we construct a linearly moving saddle-type critical point by continuously translating the domain

$$\mathbf{u}(\mathbf{x}') = \mathbf{u}(\mathbf{x} + (1 - t')\mathbf{d}), \tag{8.8}$$

where $\mathbf{d} = (0.5, 0.5)^{\mathrm{T}}$ is the direction of the translation and $t' = t\alpha$, where α controls the speed of the translation, compare Figure 8.9. The examples for streak-based topology from Section 5.2 and fig. 5.5 where computed on this linear version.

Rotating Saddle In addition, we construct another version exhibiting a curved hyperbolic trajectory by continuously rotating the saddle-type critical point.

$$\mathbf{u}(\mathbf{x}') = \mathbf{u}\begin{pmatrix} x + \sin(t')r \\ y + \cos(t')r \end{pmatrix}, \tag{8.9}$$

with the radius $r = 0.5$ and the speed of the rotation $t' = \pi t\alpha$, c.f. Figure 8.7.

Question Q.1: Steadification Both gyre saddle models are constructed by adding translation or rotation to the original. Thus, the extracted observer motion should represent a global observer transformation. The approximate Killing observer vector field approach [Had*19] extracts a uniform observer velocity field for the linear and rotating version, compare Figures 8.8a and 8.8c. The observers are very similar and approximately describe the motion of a single observer, compare Figure 8.8c. For the construction of the original model, patches in the corners of the vector

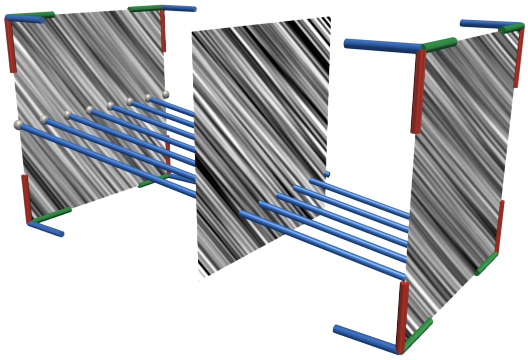

(a) Linear Gyre Saddle [Had*19]

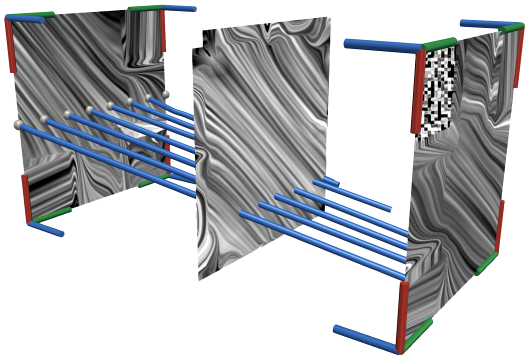

(b) Linear Gyre Saddle [GT18a]

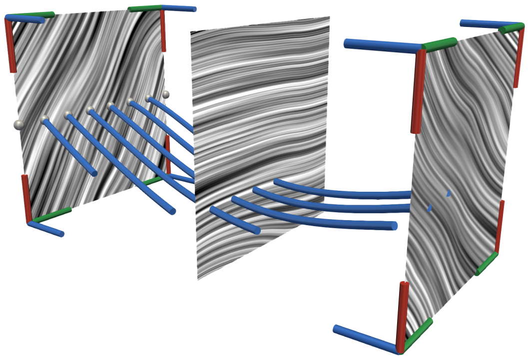

(c) Rotating Gyre Saddle [Had*19]

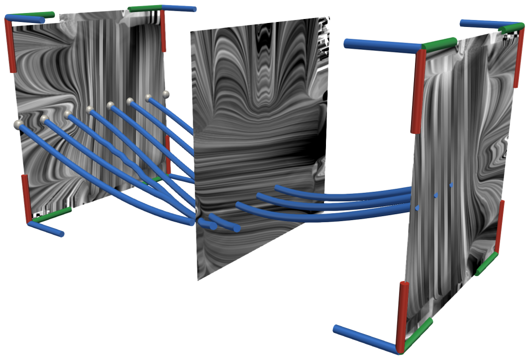

(d) Rotating Gyre Saddle [GT18a]

Figure 8.8: Corresponding observer fields for the linearly moving and rotating gyre saddle models from Figures 8.9 and 8.10. Observer world lines for $r = 0$ in blue.

field are zero. This presents a challenge for the discrete neighborhood used by Günther et al. [GGT17; GT18a]. Both methods, objective and hyperobjective, of their framework show distortions within the observer field, c.f. Figures 8.8b and 8.8d. The neighborhood size $U = 21$ limits the vicinity around the individual points that is taken into consideration during the optimization process. We can mitigate the problem related to the zero-patches by increasing U. However, this shows that a priori knowledge of the original vector field is required for fitting choices of the neighborhood U. Nevertheless, the residuals of both methods are in an acceptable range and the observed field $\mathbf{w}_r$ is steady enough.

Question Q.2: Comparison The distortions in the observer velocity field of the objective and hyperobjective approach of Günther et al. [GGT17; GT18a] carry over to the steady-as-possible field, compare Figures 8.12 and 8.13. However, since the distortions only occur at the boundary to the parts where the vector field is zero, the important features in the center are not affected. Nevertheless, the interpretation of both observer and observed field at these boundaries is highly problematic. Due to its global nature and the regularization term (Equation (6.10)), the approximate

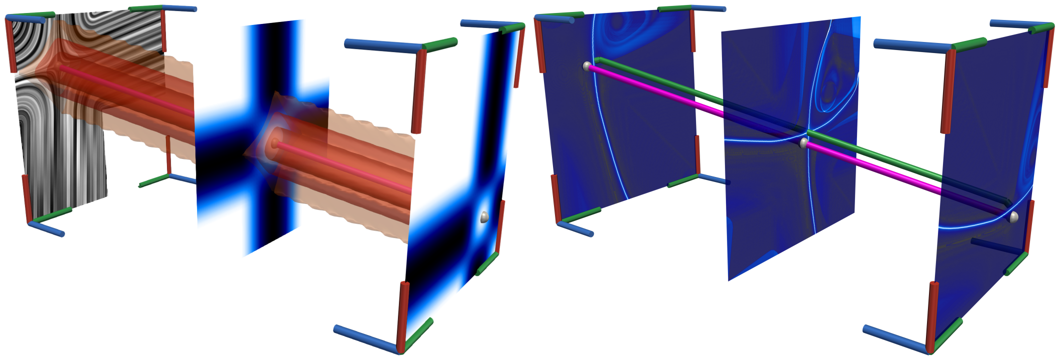

(a) Instantaneous Saddle Trajectory (b) Bifurcation Line

Figure 8.9: Instantaneous saddle trajectory (pink) with iso-surfaces of hyperbolicity ($h = \lambda_1 \cdot \lambda_2$) at $h = -0.1, -1, -2.4$ (a). Forward FTLE at $t = 0$ with advection time $T = 4$, backward FTLE at $t = 4$ and $T = -4$ and superimposed forward and backward FTLE at $t = 2.2$ with advection time $T = \pm 4$. The hyperbolic trajectory, extracted as bifurcation line in space-time (green), coincides with the intersection of forward and backward FTLE ridges at $t = 2.2$ (b).

Killing vector fields approach [Had*19] does not suffer from this problem. In the linear case the observer field can be seen as the motion of a single global observer. The contraction within the observer field (Figure 8.8c) in the rotating case suggests that local adaptation is required to steadify this field. However, their influence is limited and overall the observers behave very similar. Computation times for the respective methods adhere to our previous observations: the hyperobjective method is a magnitude faster and the objective method is two magnitude faster than the global optimization of Hadwiger et al. [Had*19].

Question Q.3: Transfer of Methods Motion of the saddle-type critical points induces vortices in the right upper corner of the dataset. Both methods find the vortex as focus-type critical point in the steady-as-possible field (Figures 8.12 and 8.13). However, for this dataset we are mostly interested in the hyperbolic trajectory that emerges close to the center. Figure 8.9 shows the linear gyre saddle, here the instantaneous saddle does not coincide with LCS extracted by FTLE ridge intersections, compare Figure 8.9b. The hyperbolic trajectory may be found as bifurcation line in space-time (Section 5.2), shown in green. This works well for straight hyperbolic trajectories, e.g., the linear gyre saddle, as Figure 8.11a illustrates. Problems related to curved parallel vector solutions become visible in the rotating gyre saddle dataset, compare Figure 8.10b. At time $t = 2.2$, superimposed backward and forward FTLE reveals that the extracted raw solutions of the bifurcation line deviates clearly from the LCS intersection, see Figure 8.11b. The fitted solution (red tube) coincides with the solutions of steady vector topology in the steady frame from both Hadwiger et al. [Had*19] and the hyperobjective method from Günther and Theisel [GT18a], shown as brown sphere. Separatrices extracted by the objective and hy-

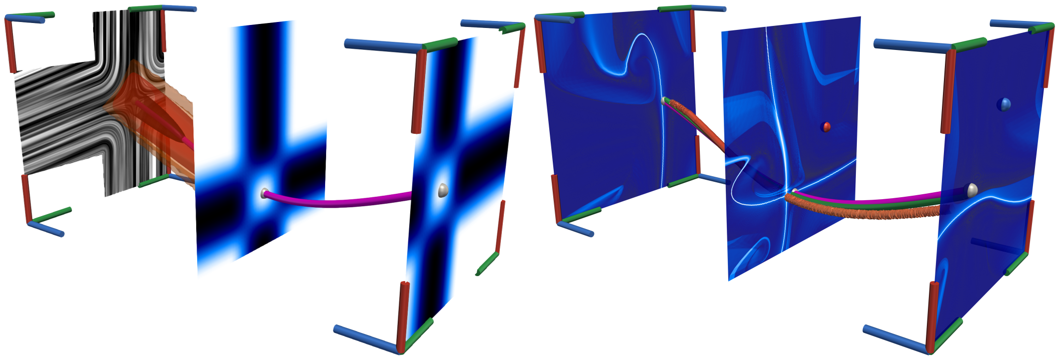

(a) Instantaneous Saddle Trajectory (b) Bifurcation Line

Figure 8.10: Slowly rotating gyre saddle model with $\alpha = r = 0.5$. Instantaneous saddle trajectory (pink), with iso-surfaces of hyperbolicity at $h = -0.1, -1, -2.5$ (a). Forward FTLE at $t = 0$, backward FTLE at $t = 4$ and superimposed forward and backward FTLE at $t = 2.2$, all with advection $T = \pm 4$. The extracted raw solutions for the bifurcation line (green) do not coincide with LCS intersections. The fitting to the true bifurcation line (orange) is able to correct this (b).

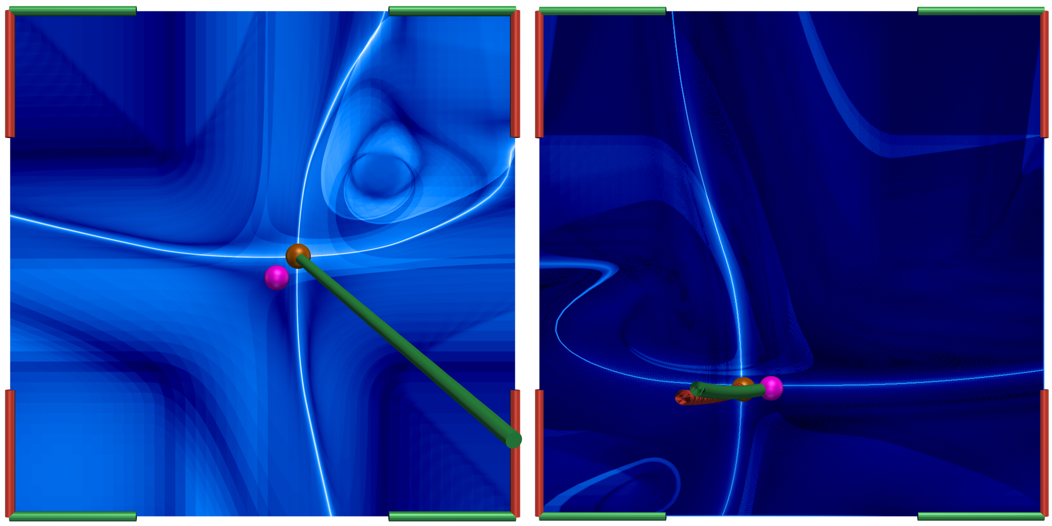

(a) Gyre Saddle Linear (b) Gyre Saddle Rotating

Figure 8.11: Superimposed backward and forward FTLE of the two gyre saddle models at $t = 2.2$ with advection time $T = \pm 4$. The trajectory of the instantaneous saddle in pink, raw solutions for the bifurcation line in green, fitted solutions in red, and objective saddle-type critical points in brown.

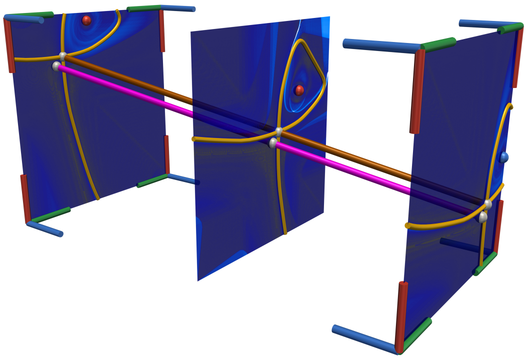

(a) Trajectory of Objective Saddle [Had*19]

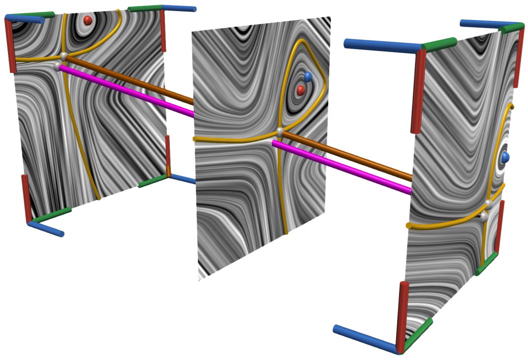

(b) Steady-as-Possible Field $\widetilde{\mathbf{w}}$ [Had*19]

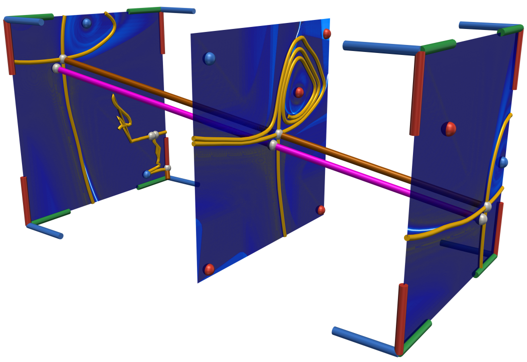

(c) Trajectory of Objective Saddle [GT18a]

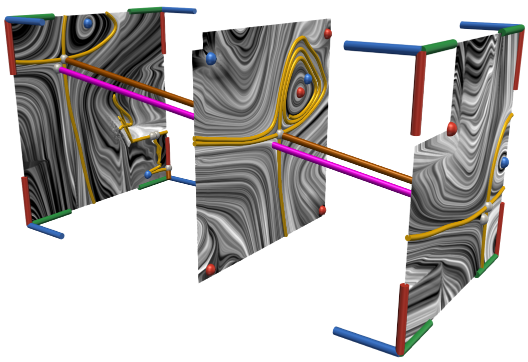

(d) Steady-as-Possible Field $\widetilde{\mathbf{w}}$ [GT18a]

Figure 8.12: FTLE images from Figure 8.9b with objective saddle trajectory (brown) and steady vector field topology in the objective frame, according to Hadwiger et al. [Had*19] (a) and Günther and Theisel [GT18a] (c). The objective fields $\mathbf{u_v}$ of the respective methods (b) and (d).

perobjective method [GGT17; GT18a] are subject to distortions seen earlier in the computed observer velocity field (Figure 8.8). This affects both gyre saddle models, see Figures 8.12 and 8.13. While they coincide with FTLE ridges in the linear case, they diverge quickly in the rotating case. The framework of Hadwiger et al. [Had*19] finds separatrices that align well in both cases. However, this is only true for the vicinity of the objective saddle, and the further separatrices are integrated the further they diverge from the LCS. Figure 8.14 shows separatrices of the steady field at time $t = 0.683$ with advection time $T = 3$, so well within the time domain of the dataset which is $[0, 4]$. Pathlines in space-time of the original field show that the FTLE ridge separates the flow and not the separatrix. To sum up, we have seen with the four centers and the two gyre saddle models that separatrix integration is not a valid way to extract invariant manifolds of the hyperobjective trajectory. This is most likely because of the difference in observers between the position of the saddle-type critical point and the locations of the integrated separatrices. We can support this by the observation that separatrices of the steady-as-possible field seem

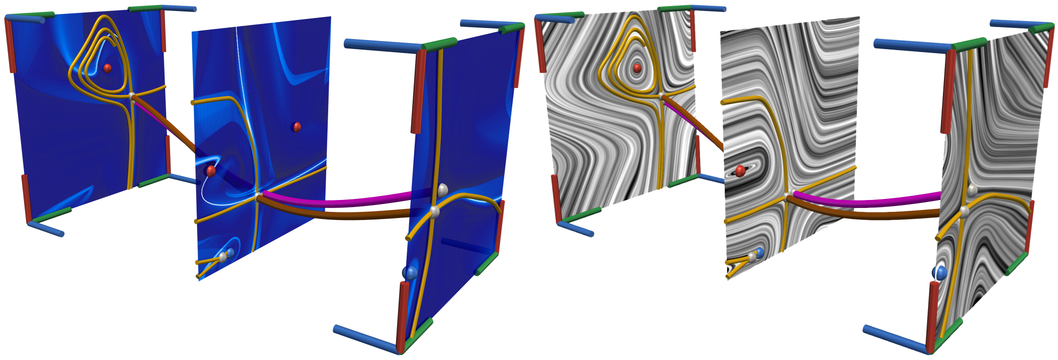

(a) Objective Saddle Trajectory [Had*19] (b) Steady-as-Possible Field $\widetilde{\mathbf{w}}$ [Had*19]

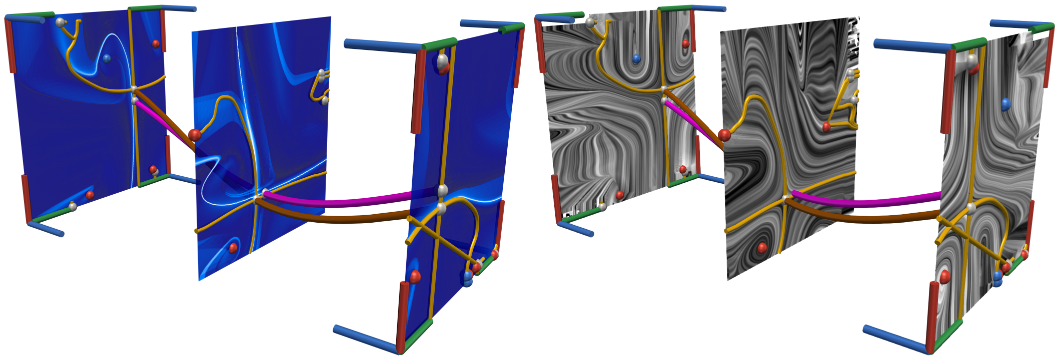

(c) Objective Saddle Trajectory [GT18a] (d) Steady-as-Possible Field $\widetilde{\mathbf{w}}$ [GT18a]

Figure 8.13: FTLE images of the rotating gyre saddle from Figure 8.10 with objective saddle trajectory (brown) and steady vector field topology in the objective frame, according to Hadwiger et al. (a) and Günther and Theisel (c). The objective fields $\mathbf{u_v}$ of the respective methods (b) and (d).

to fit more accurately with FTLE ridges of the original field the better the observer field describes the movement of a single global observer (Hypothesis 7.1). As demonstrated in Section 5.2, the main difficulty is the extraction of hyperbolic trajectories. Once found, the invariant manifolds may be computed by simple integration. Thus, there is no need to use separatrices from the steady-as-possible field.

Concerning the quality of solutions for the hyperbolic trajectory, we have seen in Figure 8.11b that both methods line up well with LCS intersection at time $t = 2.2$. The feature angle, i.e., the angle between extracted hyperbolic trajectory tangent and the vector field, reveals significant difference in the beginning. While the method by Hadwiger et al. [Had*19] fits well in the middle and diverges slowly in the beginning, the method by Günther and Theisel [GT18a] does not line up with the flow over the entire time domain. This suggests that the small distortions in the observer field have a high impact on transfer of steady vector field topology from the steady-as-possible field to the original time-dependent field. Hence, we focus mostly on its objective counterpart [GGT17] and the approach by Hadwiger et al. [Had*19].

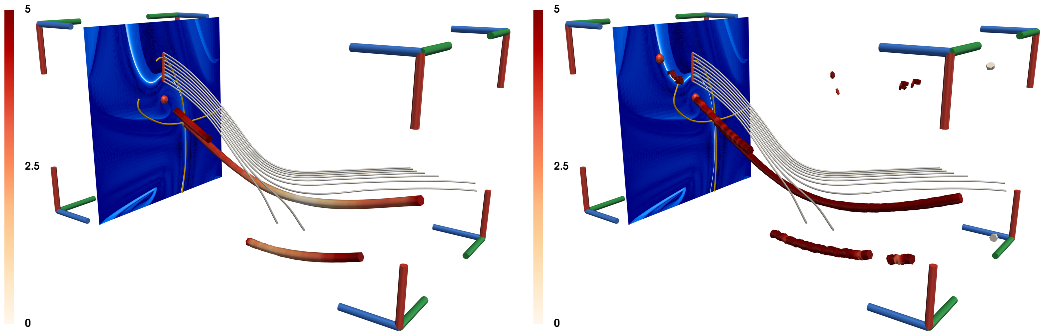

(a) Topology (Hadwiger et al. [Had*19]) (b) Topology (Günther and Theisel [GT18a])

Figure 8.14: Forward FTLE at time $t = 0.683$ with advection time $T = 4$ of the rotating gyre saddle model. Critical points (spheres) and separatrices of the steady-as-possible field (yellow tubes). The color coded feature angle of the extracted hyperbolic trajectory reveals that the solution of Hadwiger et al. [Had*19] (a) outperforms the one by Günther and Theisel [GT18a]. Pathlines (grey) of the original field seeded orthogonal to FTLE ridges and extracted show that the separation occurs at the FTLE ridge not at the separatrices.

Sadlo and Weiskopf [SW10] argued that raw solutions of parallel vectors in space-time do not need to coincide with a trajectory of the original vector field. Hence, they locally fit their PV solutions to streamlines close by. We can argue in similar fashion that the trajectories of saddle-type critical points in the steady-as-possible field do not need to be trajectories of the original field. We showed in Section 8.1.1 that the trajectory of these saddles coincide with parallel vector solutions of the observer velocity field and the original field. This only implies that along observer word lines, i.e., pathlines of the observer field, the original vector field changes as little as possible. There is no apparent reason for these locations to be part of the same trajectory. Accordingly, these solutions are just raw solutions and need further processing, i.e., fitting to the tangent of the vector field. However, in the cases we analyzed so far, the raw solutions obtained this way outperform raw parallel vectors solutions. Fitted solutions, i.e., true bifurcation lines seem to be exact.

8.1.3 Double-Gyre Model

The Double-Gyre model, introduced by Shadden et al. [SLM05], is a simplified description of the fluid motion often found in geophysical flows. It has since become a popular reference model to evaluate Lagrangian methods like the finite time Lyapunov exponent (FTLE). The original proposal used the domain $\mathbf{x} = (x, y)^{\mathrm{T}} \in [0, 2] \times [0, 1]$, and includes a scaling factor A. The distance of the two gyres is given by the parameter ϵ, this distance expands and contracts periodically in time with a period of $\omega/2\pi$. The velocity field is derived from the scalar field,

$$\begin{aligned} g(\mathbf{x},t) &= A\sin(\pi f(x,t))\sin(\pi y), \\ \text{with} \\ f(x,t) &= a(t)x^2 + b(t)x, \\ a(t) &= \epsilon\sin(\omega t) \\ b(t) &= 1-2\epsilon\sin(\omega t) \end{aligned} \tag{8.10}$$

and is then given by

$$\mathbf{u}(\mathbf{x},t) = \begin{pmatrix} u(\mathbf{x},t) \\ v(\mathbf{x},t) \end{pmatrix} = \begin{pmatrix} -\frac{\partial g}{\partial y} \\ \frac{\partial g}{\partial x} \end{pmatrix} = \begin{pmatrix} -\pi A\sin(\pi f(x,t))\cos(\pi y) \\ \pi A\cos(\pi f(x,t))\sin(\pi y)\frac{\mathrm{d}f}{\mathrm{d}x} \end{pmatrix}. \tag{8.11}$$

We saw a FTLE of the double gyre model earlier in Figure 2.9.

Quad Gyre For the analysis of hyperbolic trajectories, one may extent this model to become the so-called quad gyre, i.e, the new domain is $[0,2]^2$. Now, there exists a saddle-type critical point in the middle of the four gyres at $(1,1)^\mathrm{T}$, which oscillates horizontally. Figure 8.15a shows the quad gyre model with hyperbolicity contour surfaces at $h = -0.1, -1, -2.4$. Notice the oscillating motion of the instantaneous saddle. Raw solutions of the bifurcation lines in space-time exhibit large feature angles in between depicted time-steps, compare Figure 8.15b.

Question Q.1: Steadification Both frameworks are able to find frames of reference in which the observed field is nearly steady. Tables 8.3 and 8.4 show the corresponding average and global residuals.

Question Q.2: Comparison There is no noticeable difference in quality in the two stead-as-possible fields. The corresponding observer world lines (Figure 8.16) are in both cases spatially coherent and oscillate with the motion of the four gyres. This oscillation is more noticeable using the objective method of Günther et al. [GGT17]. However, both approximately describe the motion of a single global observer. Comparison of computation times (Tables 8.3 and 8.4) follow our observations from the last datasets, i.e., depending on the neighborhood size, the local approach by Günther et al. [GGT17] takes roughly a tenth the time the global optimization of Hadwiger et al. [Had*19] requires.

Question Q.3: Transfer of Methods We focus on hyperbolic trajectories for this dataset. Due to the oscillations of the hyperbolic trajectory in the center, the traditional extraction of raw solutions for bifurcation lines overshoot at the curved parts, compare Figure 8.15b. Further fitting is needed. Nevertheless, the feature

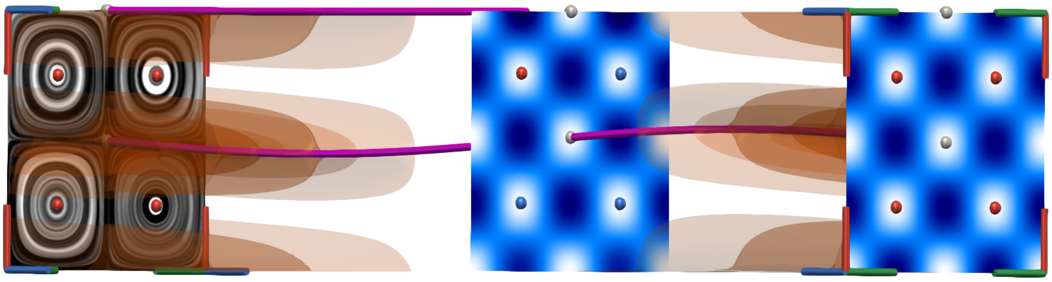

(a) Instantaneous Saddle Trajectory

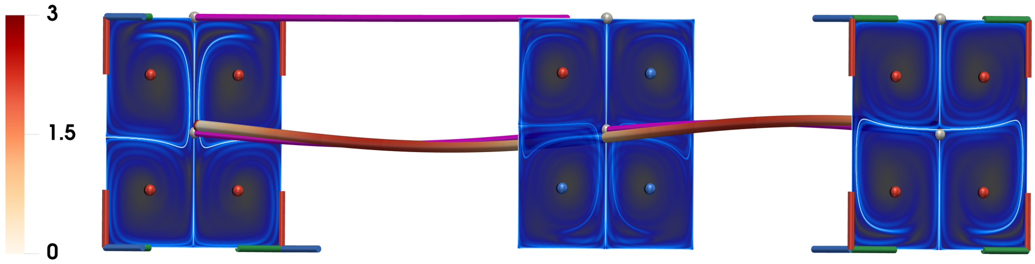

(b) Angle between Raw PV Solution and Velocity Vector

Figure 8.15: Quad-Gyre model: Instantaneous saddle trajectory in space-time with iso-surfaces of hyperbolicity at $h = -0.1, -1, -2.4$ (b). Stable (blue), unstable (red) and saddle-type (grey) critical points of the original field depicted as colored spheres. Forward FTLE at $t = 0$, backward FTLE at $t = 10$ and superimposed forward and backward FTLE at $t = 4.4$, all with advection time $T \pm 10$. The raw PV solution does coincide with FTLE ridge intersections within the time step in the middle. The color coded feature angle, between raw PV solution tangent and the velocity field, is higher in between time steps (b).

angle is in an acceptable range below 3°. The hyperbolic trajectories, extracted as saddle-type critical points of the steady-as-possible field by both the objective approaches of Hadwiger et al. [Had*19] and Günther et al. [GGT17], show similar feature angles (Figure 8.17). Notice that the feature angle varies in both cases similar to the solution extracted as bifurcation line, with a slight offset. This becomes clear when we look at LCS intersections (Figure 8.18). In the particular time-step depicted, the raw bifurcation line solution and the objective framework by Günther et al. [GGT17] give similar solutions, while the solution of Hadwiger et al. [Had*19] is slightly offset. However, this change depends on the individual time-step, since all three solutions vary in quality over the space-time domain. These findings support our hypothesis (Hypothesis 7.3), that solutions obtained as saddle-type critical points from the steady-as-possible field need to be fitted to pathlines in the same manner solutions obtained as PV do.

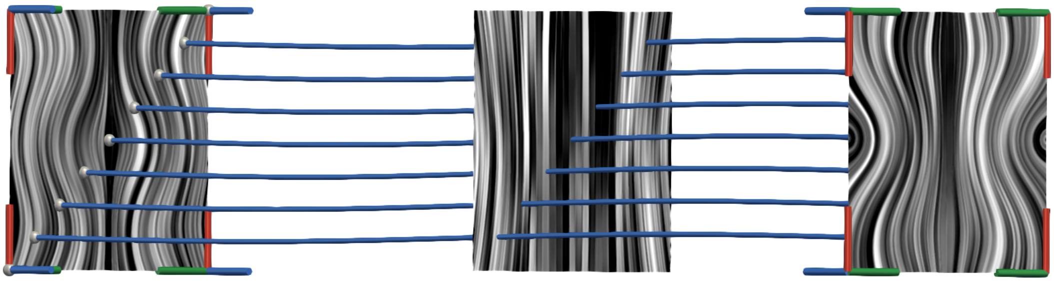

(a) Observer Velocity Field **v** [Had*19]

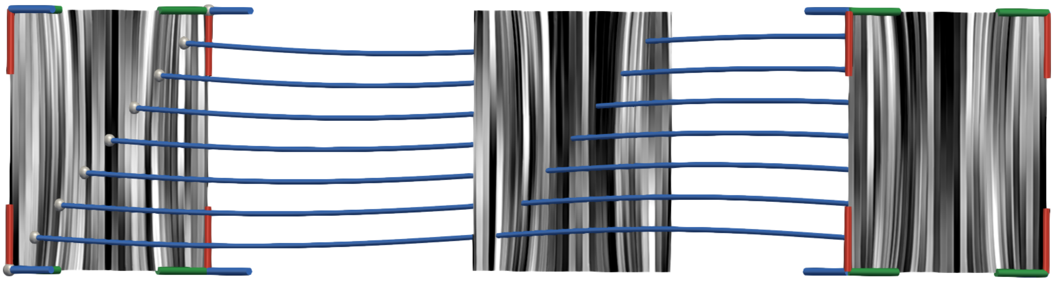

(b) Observer Velocity Field **v** [GGT17]

Figure 8.16: Observer velocity fields **v** of the quad gyre model and corresponding observer world lines for the method from Hadwiger et al. [Had*19] and the objective version of the framework from Günther et al. [GGT17]. Observers in both cases move coherently over the entire domain.

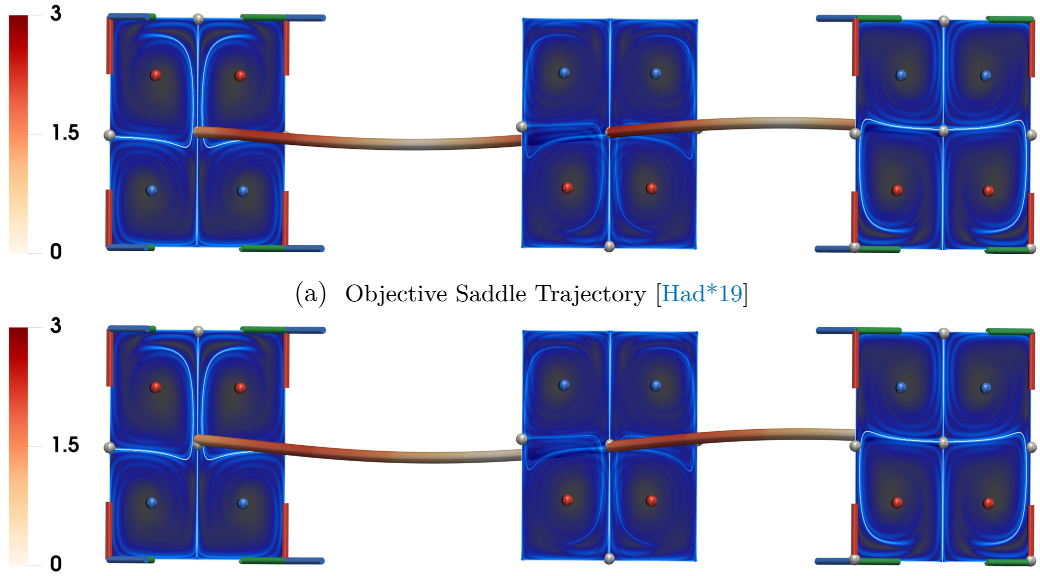

(a) Objective Saddle Trajectory [Had*19]

(b) Objective Saddle Trajectory [GGT17]

Figure 8.17: FTLE from Figure 8.15 and objective saddle trajectories of the methods from Hadwiger et al. [Had*19] (a) and Günther et al. [GGT17] (b) color coded according to their feature angles.

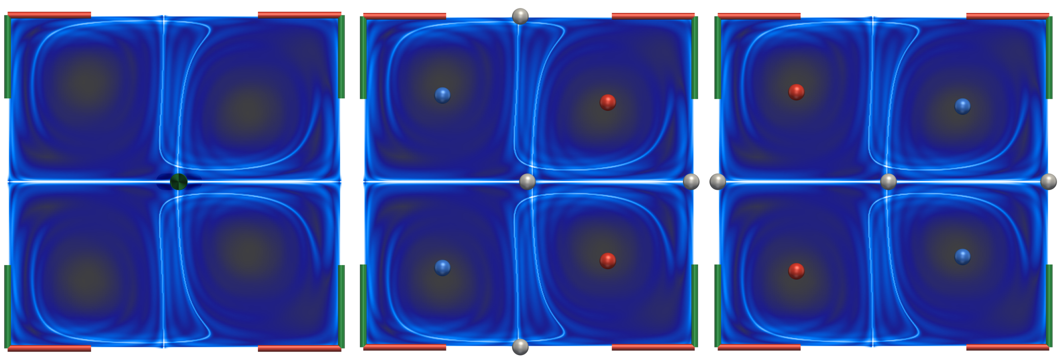

(a) Raw Bifurcation Line (b) Hadwiger et al. [Had*19] (c) Günther et al. [GGT17]

Figure 8.18: Superimposed forward and backward FTLE of the quad gyre model at $t = 4.4$ with advection time $T = \pm 10$. The extracted hyperbolic trajectory as raw bifurcation line (a) and as saddle in the objective frame from Hadwiger et al. [Had*19] (b) and Günther et al. [GGT17] (c).

8.2 Bifurcation Analysis

According to our reasoning in Chapter 7, all three frameworks are expected to (partially) fail when it comes to highly non-linear phenomena. Major flow events like critical point bifurcations, i.e., their birth and death or their change of stability, are such non-linear phenomena. In this chapter we investigate two types bifurcations introduced earlier in Section 5.1.2.

- Saddle-node bifurcation, where two critical points of opposite Poincare-Hopf index, i.e., a saddle together with either a focus or node, emerge or dissolve.
- Hopf bifurcation, where a critical point, focus or node, changes stability via a pair of purely imaginary eigenvalues of its Jacobian.

8.2.1 Saddle-Node Bifurcation

We create a saddle-node bifurcation from a vector field with varying parameter r.

$$\mathbf{u}(x,y,r) = \begin{pmatrix} rx - x^2 \\ y \end{pmatrix}. \tag{8.12}$$

The bifurcation occurs when r crosses zero, i.e., when $r < 0$ there exist no critical points, when $r = 0$ there is a saddle-node point and when $r > 0$ there exist two critical points, one saddle and one node-type. Note that the critical points move toward each other along the stable invariant manifolds of the saddle. We may also think of a saddle-focus bifurcation. There, the critical points approach each other between the stable and unstable invariant manifolds due to the rotation of the focus. From the one-parameter family of vector fields (Equation (8.12)) we construct a time-dependent vector field where $t = 1 - r$. Figure 8.19 illustrates this setup.

Question Q.1: Steadification At first glance, the residuals of all three methods (Tables 8.3 and 8.4) suggest that they are able to construct local frames in which no bifurcation occurs. However, the fact that the vector field has a low magnitude at the region around the bifurcation, indicates that these residuals are misleading. In fact, Figure 8.20 shows that in the objective $\widetilde{\mathbf{w}}$ field of each method, two critical points collide and dissolve. Figure 8.21b illustrates how the framework of Hadwiger et al. [Had*19] manages to steadify the field prior to the bifurcation. The horizontal trajectories of both critical points indicate that they do not move at first (Figure 8.21b). Nonetheless, when r approaches 0, the critical points collide rapidly, indicated by the almost vertical trajectories in space-time. Consider the corresponding observer world lines (Figure 8.21a), they show how the observers fold invert. With this case we prove, that vector fields that exhibit saddle-node bifurcations cannot be steadified by any of the techniques discussed. We have eluded in Chapter 7 that neither outcome for the saddle-node bifurcation is satisfactory: If the bifurcation is absorbed by the observer field we lose essential information about

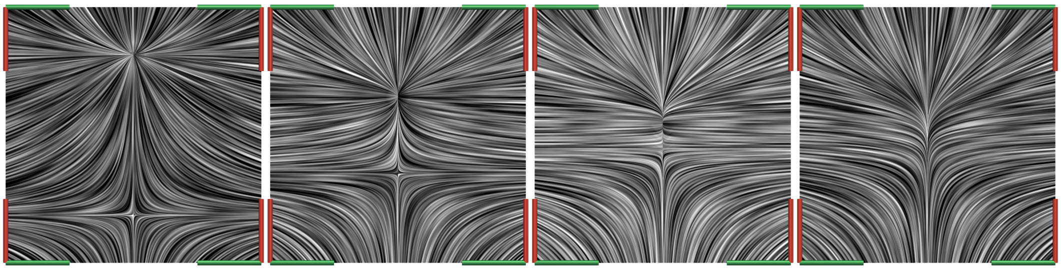

(a) $r = 0.25$ (b) $r = 0.1$ (c) $r = 0.025$ (d) $r = -0.025$

Figure 8.19: Saddle-node bifurcation with varying r parameter. Bifurcation occurs at $r = 0$.

the original field, i.e., the benefits of the steady-as-possible field is severely compromised. The affect on feature extraction in this steady-as-possible frame is explored on real-world datasets in Section 8.3. Questions Q.2 and Q.3 concerning saddle-node bifurcations are summarized together with findings from Hopf bifurcations.

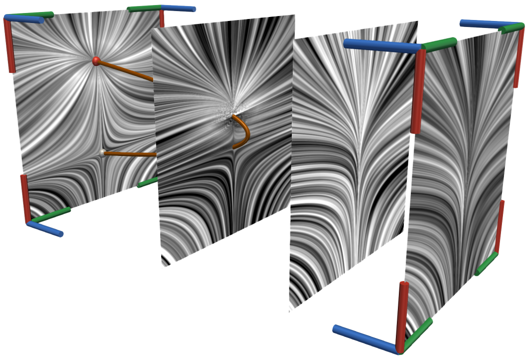

(a) Original Field $\mathbf{u}$

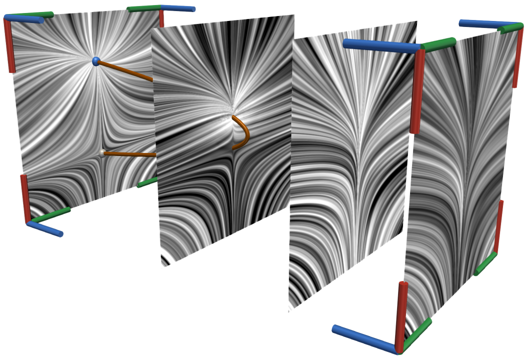

(b) Objective Frame $\widetilde{\mathbf{w}}$ [Had*19]

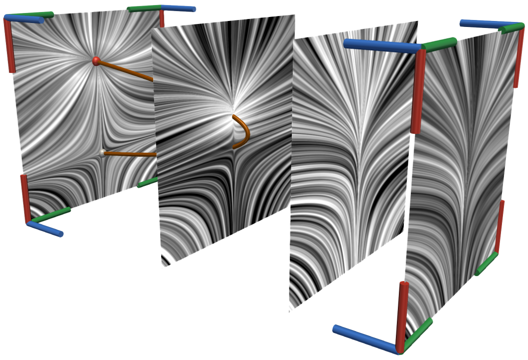

(c) Objective Frame $\widetilde{\mathbf{w}}$ [GGT17]

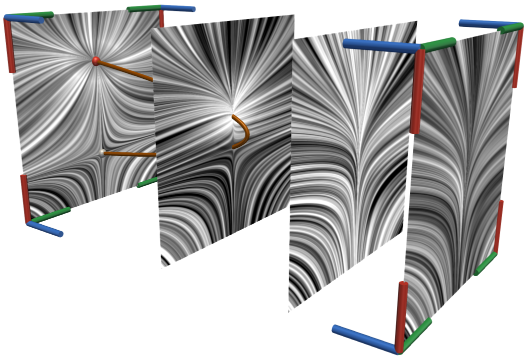

(d) Objective Frame $\widetilde{\mathbf{w}}$ [GT18a]

Figure 8.20: Space-time representation of a saddle-node bifurcation, with LIC at times $r = 0.25, 0.1, -0.1, -0.25$. Critical points (spheres) and their trajectories in the original field (a), in the objective frame $\widetilde{\mathbf{w}}$ by Hadwiger et al. [Had*19] (b), by Günther et al. [GGT17] (c) and by Günther and Theisel [GT18a] (d).

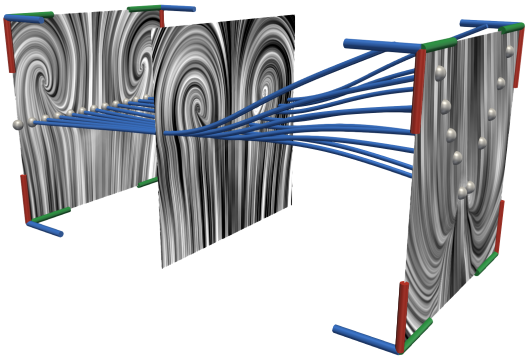

(a) Observer Velocity Field $\mathbf{v}$

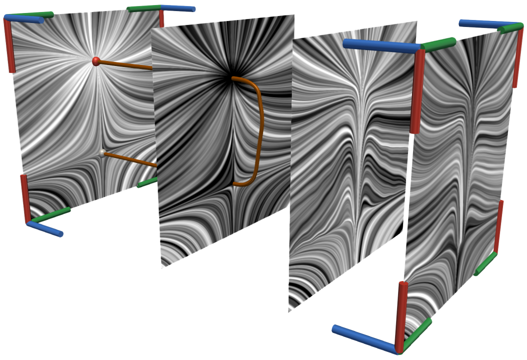

(b) Steady-as-Possible Field $\mathbf{w}_r$

Figure 8.21: Space-time representation of the observer velocity field according to Hadwiger et al. and corresponding observer world lines (a) Steady-as-Possible frame with critical points trajectories (b).

8.2.2 Hopf Bifurcation

During an Andronov-Hopf, or simply Hopf, bifurcation, a critical point changes stability, from stable to unstable or vice versa, via a pair of purely imaginary eigenvalues of its Jacobian. In this process a limit cycle emerges. This limit cycle is called supercritical if it is stable and subcritical if it is unstable, see Section 5.1.3. An example in 2D space is

$$\mathbf{u}(x, y, \mu) = \begin{pmatrix} \mu x - y + x - y^2 \\ x + \mu y + y^3 \end{pmatrix}. \tag{8.13}$$

Similar to Section 8.2.1 we construct a time-dependent vector field from Equation (8.13) with a Hopf bifurcation at $t = 1$ and an unstable limit cycle growing outward with increasing t.

Question Q.1: Steadification The original vector field (Figure 8.22a) exhibits a hopf bifurcation at $t = 1$ where the repelling focus-type critical points becomes attracting. A steady version of this phenomena is created by the method of Hadwiger et al. [Had*19], compare Figure 8.22b. Over the entire duration no hopf bifurcation occurs and the focus retains its repelling behavior. Figures 8.22c and 8.22d show how the limit cycle is represented within the observer field. To achieve this the observers start to wrap around the center. Both objective and hyperobjective frameworks from Günther et al. [GGT17; GT18a] are unable to incorporate the limit cycle into the their observer field. Figure 8.23 shows the focus in the $\widetilde{\mathbf{w}}$ field changes stability.

Question Q.2: Comparison The residual of the hyperobjective and objective method might suggest that a steady frame of reference was found, however, since the magnitude of the vector field around the event is low $|\mathbf{v}| << 1$, this is misleading. Due to the wrapping of observers around the center in case of the Hadwiger et al. [Had*19] framework, the interpretation is unclear. In addition, we lose information of the original field that is not represented in the steady-as-possible field. This supports our hypothesis that stability cannot be inferred from the steady-as-possible field. Table 8.3 shows that the overall residual of this method is high, it maybe further reduced by increasing iterations. However, considering that the Hopf bifurcation is already correctly represented in the observer field, this may not be necessary. Compared to the methods of Günther et al. [GGT17] the computational cost is high, but is justified by the significantly improved solution.

Question Q.3: Transfer of Methods Since non of the frameworks can find local frames such that saddle-node bifurcations appear steady, the application of methods from steady realm is limited. However, the time derivative of the new steady-as-possible field is considerable lower than the one of the original field, and as Figure 8.21b showed, up until the bifurcation occurs and right after it, the field appears steady. Thus, we can speculate that this only introduces local discontinuities

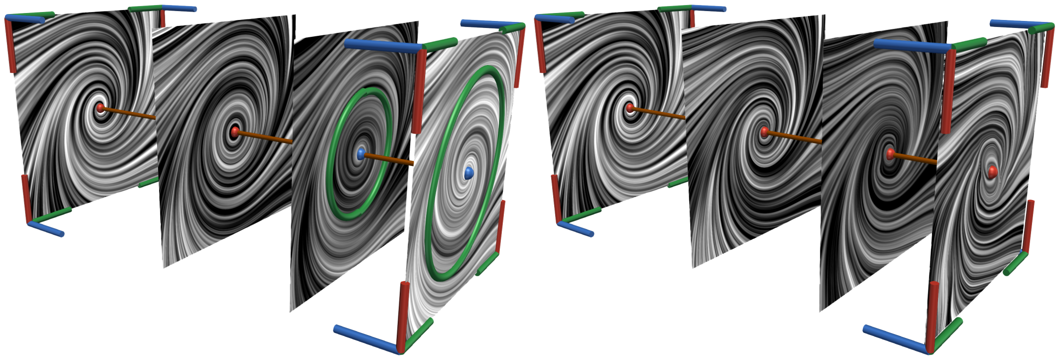

(a) Original Field **u** (b) Steady-as-Possible Field **w** [Had*19]

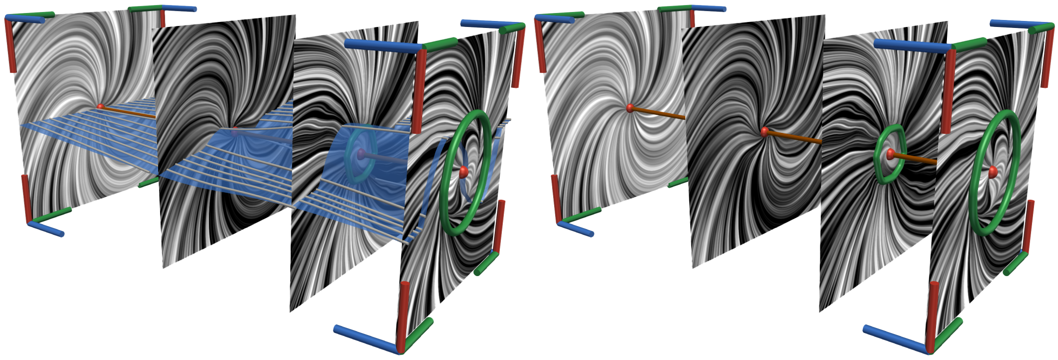

(c) Observer World Lines **v** [Had*19] (d) Observer Velocity Field **v** [Had*19]

Figure 8.22: Space-time view of a Hopf bifurcation with varying parameter $-1 \leq \mu \leq 1$ (a). Space-time views of the steady-as-possible field according to Hadwiger et al. [Had*19] (b) does not show a Hopf Bifurcation. The corresponding observer world lines (c) and observer velocity field (d) absorbs the Hopf bifurcation. The an unstable limit cycle grows from the middle time steps.

and we may be able to apply steady visualization techniques non the less. Of course this fact plays an important role when interpreting the visualization later on. In case of the Hopf bifurcation the argument is similar for the (hyper) objective frameworks of Günther et al. [GGT17; GT18a]. For the result of the method from Hadwiger et al. [Had*19] we established due to the information lost we cannot infer stability of trajectories in the original field from stability in the steady-as-possible field.

8.3 Simulated Datasets

Now that we evaluated our hypotheses on small analytical datasets that aim to single out certain aspects like bifurcations, we turn to real world datasets obtained by fluid simulation, to investigate these claims further and inspect their impact in more complex and realistic settings. We split these tests into three parts. The first is concerned with a von-Kármán vortex street that only exhibits very isolated

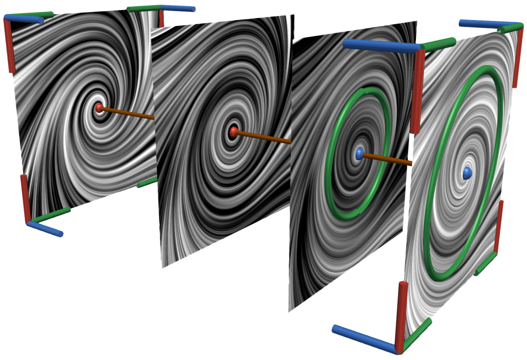

(a) Steady-as-Possible Field **w** [GGT17]

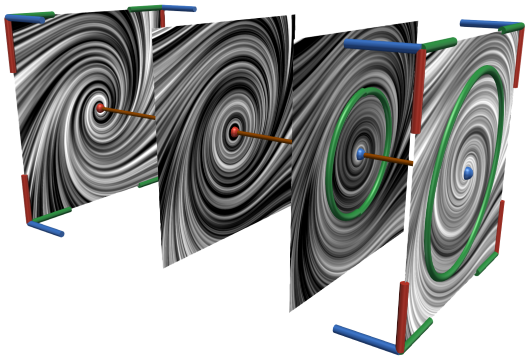

(b) Steady-as-Possible Field **w** [GT18a]

Figure 8.23: Steady-as-possible field according to Günther et al. [GGT17] (a) and Günther and Theisel [GT18a] (b) show a Hopf bifurcation, which is not absorbed by the respective observer fields.

critical point bifurcations and otherwise is a prime example of a Galilean observer. Our second simulated dataset is comprised of four moving vortices that transcend into turbulence. Finally, we introduce the hotroom dataset that regularly exhibits saddle-node bifurcations on which we further review our findings from Section 8.2.

8.3.1 Von-Kármán Vortex Street

This dataset was obtained by a numerical simulation of an incompressible fluid behind an obstacle. The fluid enters from the left with constant velocity and leaves the domain on the right. The top and bottom boundaries are simulated as no-slip boundaries, i.e., velocity directly at the edge is zero. The simulated fluid has a Reynolds number of $\Re = 160$. The Reynolds number captures the laminar and turbulent characteristics of a flow

$$\Re = \frac{uL}{\nu}, \tag{8.14}$$

where u is the relative velocity (m/s), L is a characteristic dimension (m), and ν is the kinematic viscosity of the fluid (m^2/s). Thus, the numerator captures inertial forces and the denominator captures viscous forces. A low Reynolds number ($\Re < 2.3 \cdot 10^3$) corresponds to laminar dominated flow, i.e., streamlines nearly parallel, and a high Reynolds number ($\Re > 4 \cdot 10^3$) corresponds to turbulent fluid flow. After 12 seconds vortices start to form behind the obstacle, which are not directly visible within the velocity field (Figure 8.24a). These vortices are advected with the flow with approximately the same constant velocity. Hence, von-Kármán vortex streets behind obstacles have become a classic example for Galilean invariance.

Question Q.1: Steadification Compared to earlier examples the residuals of all methods are significantly higher. However, the observer fields and steady-as-

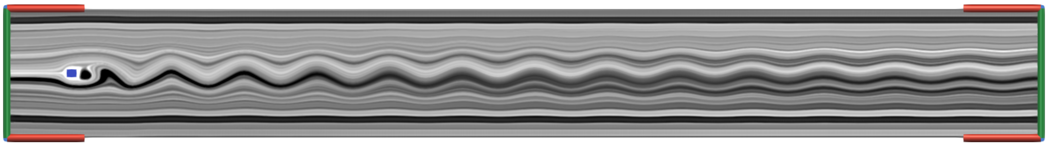

(a) Original Velocity Field $\mathbf{u}$

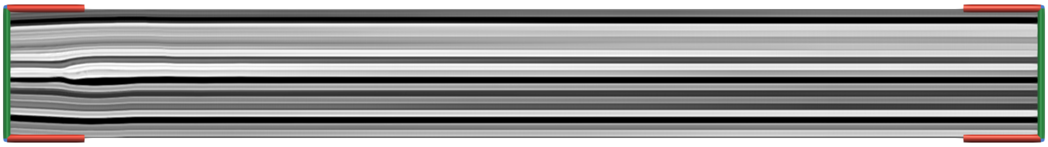

(b) Observer Velocity Field $\mathbf{v}$ [Had*19]

(c) Observer Velocity Field $\mathbf{v}$ [GGT17]

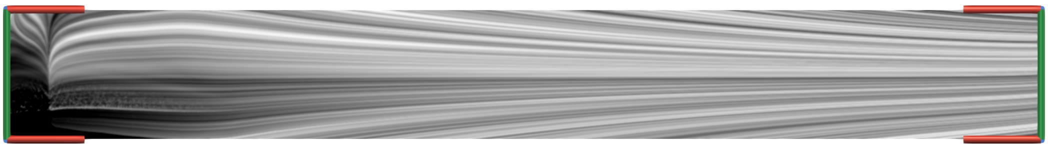

(d) Observer Velocity Field $\mathbf{v}$ [GT18a]

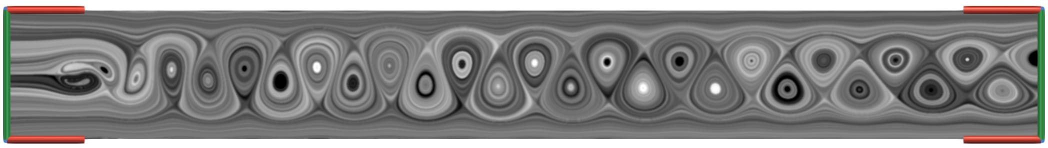

(e) Field in Objective Frame $\widetilde{\mathbf{w}}$ [Had*19]

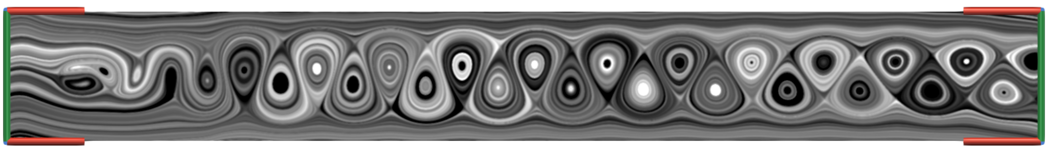

(f) Field in Objective Frame $\widetilde{\mathbf{w}}$ [GGT17]

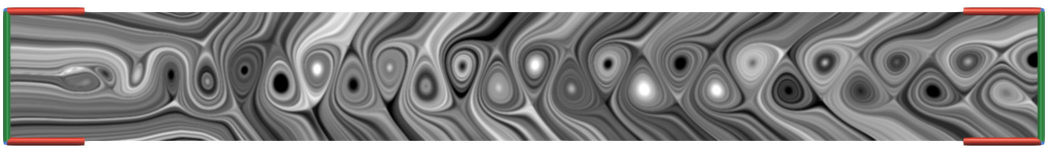

(g) Field in Objective Frame $\widetilde{\mathbf{w}}$ [GT18a]

Figure 8.24: LIC of original von-Kármán vortex street behind a cylinder at $t = 15s$ (a). The observer fields ((b),(c),(d)) and steady-as-possible fields by the respective frameworks ((e), (f), and (g)).

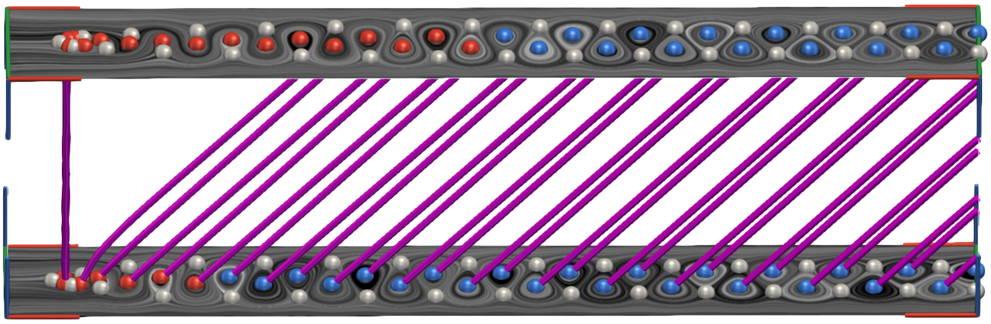

(a) Vortex Core Lines [Had*19]

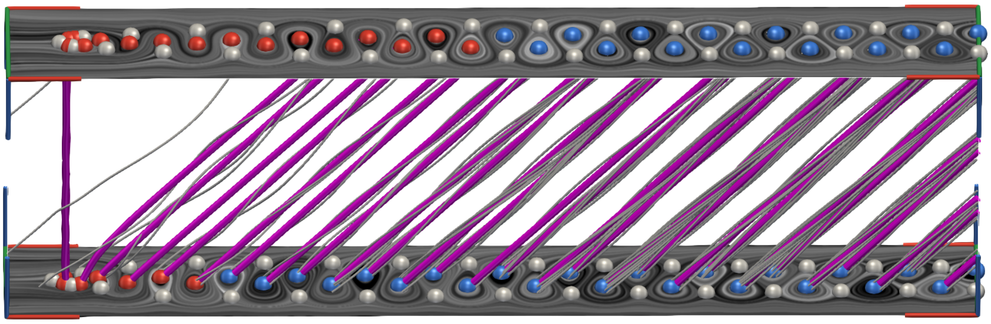

(b) Vortex Core Lines with Streamlines [Had*19]

Figure 8.25: A von-Kármán behind a cylinder in space-time for $15s \leq t \leq 17.4s$. Attracting (blue), repelling (red) and saddle-type (grey) critical points of the instantaneous vector fields at $t = 15s$ and $t = 17.4s$. The vortex core lines (pink) are trajectories of these attracting and repelling critical points (a). Streamlines seeded near the vortex core lines reveal rotating behavior (b).

possible fields (Figure 8.24) reveal that this is predominantly due to turbulence directly behind the cylinder. Otherwise all three techniques compute a sufficiently steady observer velocity field $\mathbf{w}_r$, with $r = 15s$.

Question Q.2: Comparison Computed steady-as-possible fields vary significantly, compare Figures 8.24e to 8.24g. Figure 8.24 shows that the method by Hadwiger et al. [Had*19] produces the cleanest result, including the far right of the domain. The objective method by Günther et al. [GGT17] shows very similar results but the resulting steady-as-possible field is distorted near the inlet and outlet, c.f. Figure 8.24f. Corresponding observer fields (Figures 8.24b and 8.24c) describe uniform motion for the majority of the domain. The global optimization [Had*19] shows only very slight changes around the obstacle, while the local objective approach of Günther et al. [GGT17] fails to compute globally coherent observers. Moving on to hyperobjective observers [GT18a], we see that the observer field has a discontinuity near the inlet on the left and starts to collapse toward the middle of the dataset. This leads to significant distortions around the vortices in the centers, i.e., the field

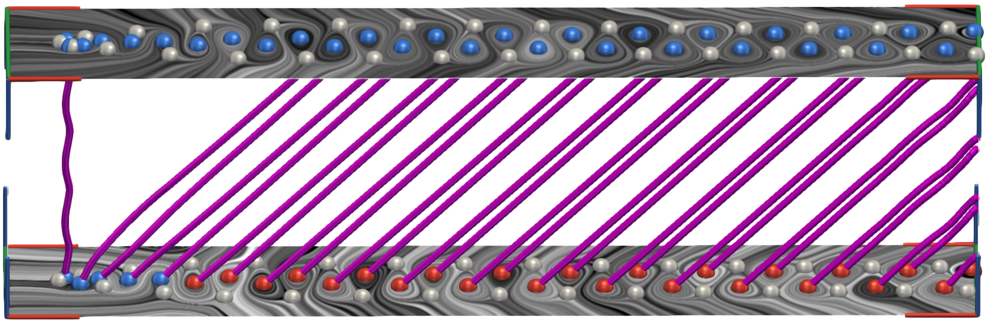

(a) Vortex Core Lines [GT18a]

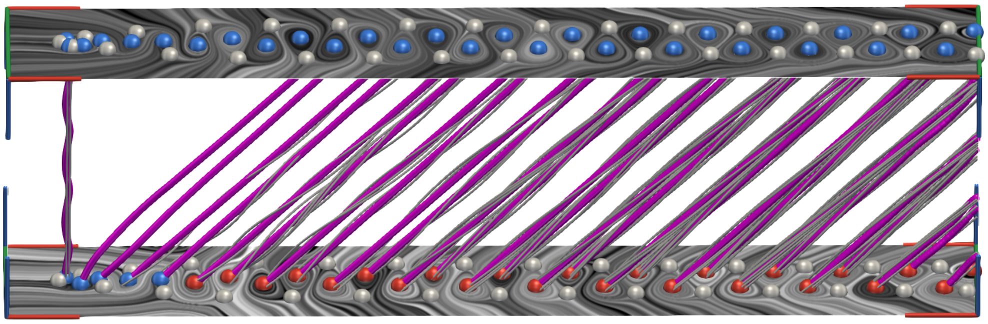

(b) Vortex Core Lines with Streamlines [GT18a]

Figure 8.26: Same as Figure 8.25, vortex cores according to Günther and Theisel [GT18a].

is not tangential to the no-slip boundaries on the top and bottom of the dataset. Although this has no apparent effect on the loci of extracted core lines, we will see that this does not accurately reflect the behavior of the original velocity field when we look at hyperbolic trajectories.

Question Q.3: Transfer of Methods Figures 8.25 and 8.26 show the extracted vortices from seconds $15 - 17.4$, computed by the methods of Hadwiger et al. [Had*19] and hyperobjective method of Günther and Theisel [GT18a] respectively. The vortices in the first and last time-step are detected as critical points in the steady-as-possible field. Red and blue spheres correspond to repelling and attracting vortices, and grey spheres indicate saddle-type critical points. We note that the vortices within the von-Kármán street have only very limited attracting and repelling properties, thus, they are sometimes detected as repelling and other times as attracting depending on the current time-step. The paths of the vortices (pink) are obtained as pathlines of critical points in the steady-as-possible field $\mathbf{w}_r$ and then transformed back to the original domain. In both cases, pathlines seeded in the vicinity of the detected vortices stay close to the detected solutions. Analysis of the angle of the tangent of the vortex core lines and the velocity field are below a threshold of 3°. Thus, both methods are able to accurately find vortex core lines in this example. Figure 8.27 shows forward and backward FTLE of the dataset, as well as steady vector field topology in the observed field $\mathbf{w}_r$. As we argued earlier, separatrices in the steady-as-possible field are not accurately able to describe LCS of the original velocity field. While separatrices extracted by the global approximate Killing vector fields approach [Had*19] and the objective local approach [GGT17] mostly coincide with FTLE ridges, the hyperobjective local approach [GT18a] yields separatrices that are not relatable to the original field. This is caused by the divergence present in the observer velocity field (Figure 8.24d).

In any of the three cases, saddle-type critical points from the steady-as-possible frames do not align properly with the FTLE ridge intersections. However, we note that the ridges of the forward FTLE are not very sharp, and as Machado et al. [Mac*16] have suggested this may be false positives. Figure 8.28 shows superimposed FTLE in forward and reverse time within a subset of the original datasets. There, it is clearly visible that neither intersections of FTLE ridges that are not sharp and saddle-type critical points in the steady-as-possible field imply separating behavior of pathlines in the original field. At least within this time-range no exponential separation, as typically indicated by FTLE, is visible. Nonetheless, Figure 8.28b illustrates the low feature angles of the objective saddle trajectories.

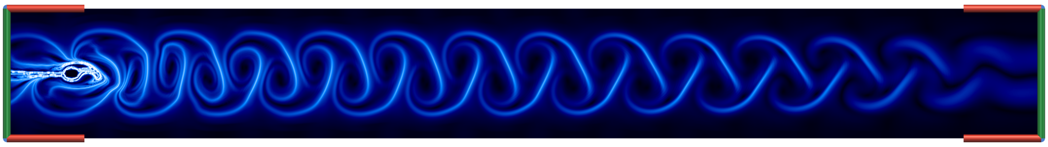

(a) Forward FTLE at $t = 16.2s$ with $T = 1.2s$

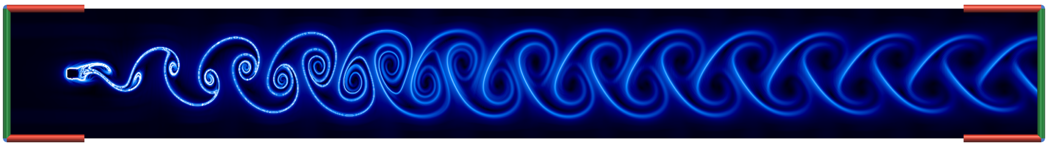

(b) Backward FTLE at $t = 16.2s$ with $T = -1.2s$

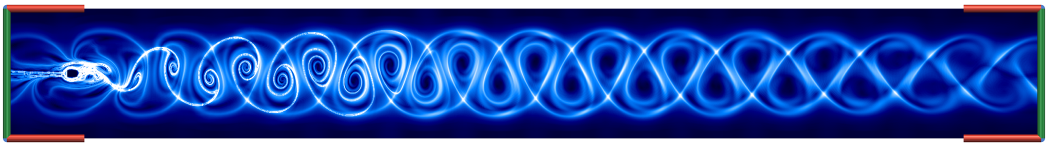

(c) Superimposed Forward and Backward FTLE at $t = 15s$ with $T = -2.4s$

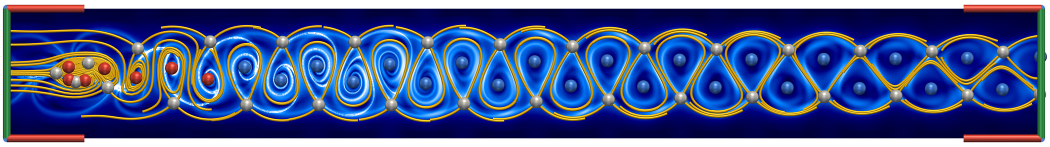

(d) Vector Field Topology in Objective Frame [Had*19]

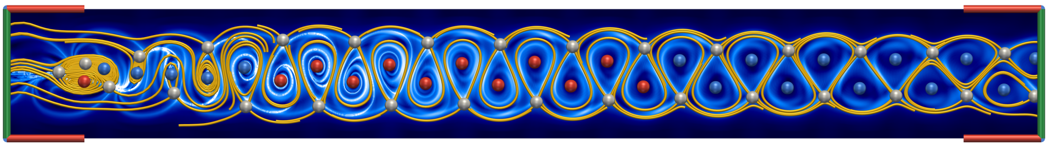

(e) Vector Field Topology in Objective Frame [GGT17]

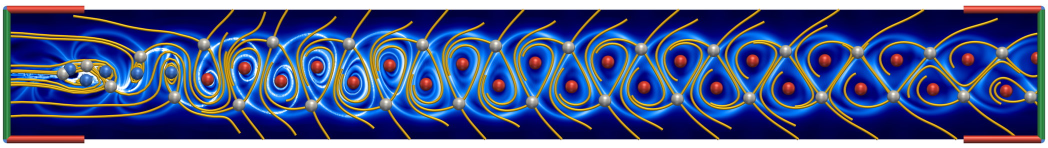

(f) Vector Field Topology in Hyperobjective Frame [GT18a]

Figure 8.27: Forward (a), backward (b), and superimposed FTLE (c) of a von-Kármán vortex street. Steady vector field topology in the steady-as-possible frame of the respective methods ((d),(e), and (f)).

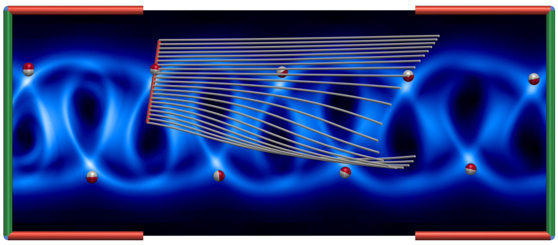

(a) Top View

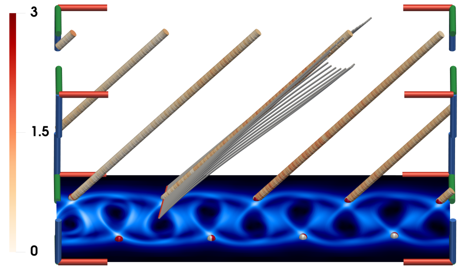

(b) Side View

Figure 8.28: Superimposed forward and backward FTLE at time $t = 16.2s$ with advection time $T = -1.2s$. Saddle-type critical points according to the framework of Hadwiger et al. [Had*19] (grey spheres) and according to the hyperobjective framework of Günther and Theisel [GT18a] (red spheres). Top view with pathlines seeded across FTLE ridges (a). Side view with trajectories of saddle-type critical points with color coded feature angle (b).

8.3.2 Buoyant Plumes

Similar to the von-Kármán vortex street, the buoyant plumes dataset is obtained by numerical simulation of a fluid. It represents the buoyant flow within a closed container. A small region in the center of the bottom plate is heated and a small region on the top plate is cooled. The fluid velocity is initially zero within the entire domain. All boundaries are no-slip boundaries. At first, two plumes, a cold one dropping and a hot one rising, form at the top and bottom. When they meet in the middle, both get deflected and travel horizontally to the side. The flow becomes turbulent when the plumes are reflected from the vertical walls on the left and right, and hot and cold fluid starts to mix. We analyze this field between $0s$ and $2s$.

Question Q.1: Steadification Although the residual of all three methods is comparatively high $\sim 10^1$, this is mostly due to the onset of turbulence when the two plumes hit the side walls. Figure 8.29 shows the dataset in space-time as well as the respective steady-as-possible fields $\widetilde{\mathbf{w}}$. In all cases the paths of the plumes (pink tubes) are accurately represented. We note that the version computed using the method of Hadwiger et al. [Had*19], the foci in the center of the plumes are stable not unstable compared to the original field and the other steady-as-possible fields from the (hyper-) objective frameworks of Günther et al. [GGT17; GT18a]. However, this is only due to the fact that in incompressible flow repelling and attracting foci and nodes cannot not exist, and because of numerical computation of the eigenvalues of the Jacobian these points get classified as attracting or repelling critical points.

Question Q.2: Comparison Overall, vortices may be extracted from any of the aforementioned steady-as-possible fields. Observer world lines of the method by Hadwiger et al. [Had*19] show that observers locally follow the fluid, compare Figure 8.30a. This represents different local observers for smaller coherent regions.

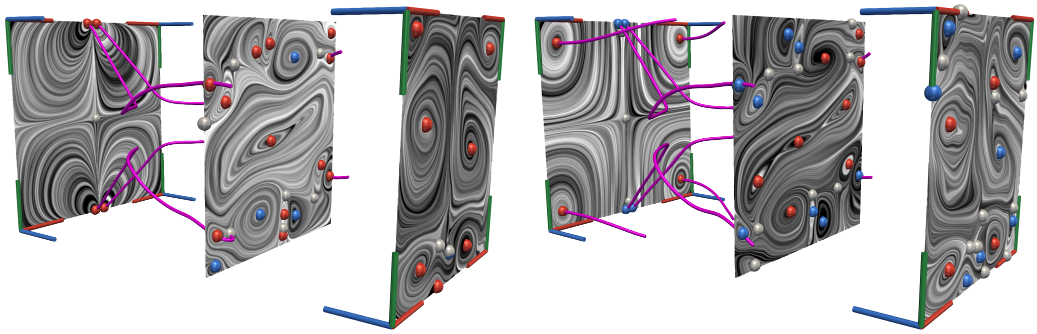

(a) Original Field $\mathbf{u}$ (b) Steady-as-possible field $\widetilde{\mathbf{w}}$ [Had*19]

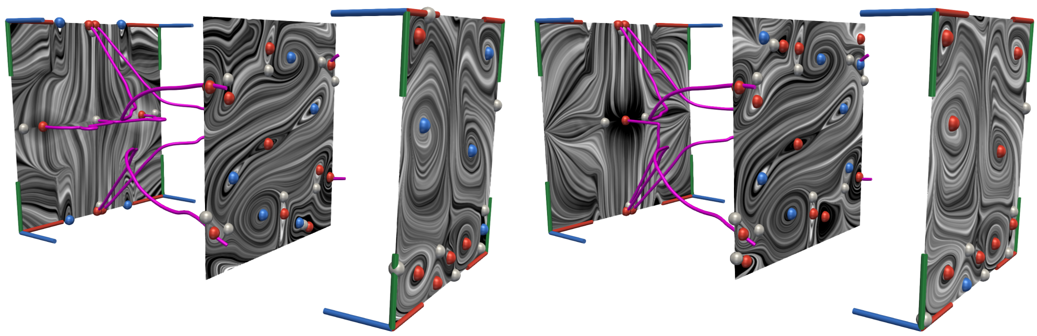

(c) Steady-as-possible field $\widetilde{\mathbf{w}}$ [GGT17] (d) Steady-as-possible field $\widetilde{\mathbf{w}}$ [GT18a]

Figure 8.29: Buoyant plumes dataset space-time with LICs at $t = 0s, 1s, 2s$. Spheres represent critical points colored according to their stability of the respective field. Pink tubes are the paths of the four vortices as pink tubes in the respective frames of reference.

Interpretations of those is harder, but they generally follow local rigid body motion, i.e., at least locally they represent rigid body observers. Computation times are consistent with earlier observations, that the local hyperobjective method [GT18a] is a magnitude faster, and the objective method [GGT17] two magnitudes faster than the approach by Hadwiger et al. [Had*19].

Question Q.3: Transfer of Methods Figure 8.30 illustrates that there exist false positive vortex core line detections in all of the three frameworks. We could find reasonably long vortex core lines with high feature angles $> 15°$. Pathlines seeded around these show that the fluid does not rotate around the found solutions. The original authors have shown similar datasets where vortex core lines where extracted correctly. It is fact, that most detected vortex core lines are indeed common axis of fluid rotation. However, as Figure 8.30 shows, there exist false positive nonetheless. This supports our claim from Chapter 7 that solutions obtained within these frameworks do need to be filtered as well. The smoothing effect of the local

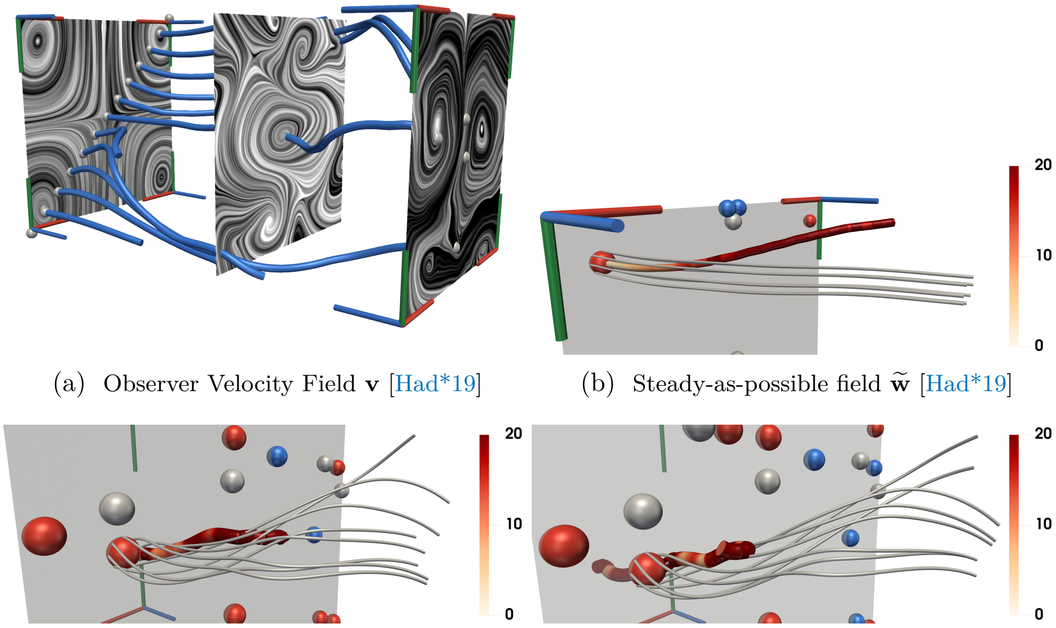

(a) Observer Velocity Field $\mathbf{v}$ [Had*19]   (b) Steady-as-possible field $\widetilde{\mathbf{w}}$ [Had*19]

(c) Steady-as-possible field $\widetilde{\mathbf{w}}$ [GGT17]   (d) Steady-as-possible field $\widetilde{\mathbf{w}}$ [GT18a]

Figure 8.30: The observer field computed by Hadwiger et al. [Had*19] with corresponding observer world lines in blue (a). Critical points of the respective objective fields (spheres). Vortex core lines extracted by Sujudi and Haimes [SH95b] in the objective field $\widetilde{\mathbf{w}}$ [Had*19] colored with their angle to the original field. Pathlines of the original field seeded around the extracted vortex cores, reveal that the flow rotates around neither.

neighborhood of both methods from Günther et al. [GGT17] only helps to eliminate small false positive. During the initial phase, where the two plumes move distinctively, extracted hyperbolic trajectories coincide with LCS intersections, compare Figure 8.31a. After the onset of turbulence, where multiple saddle-node bifurcation take place, the objective saddle points in the steady-as-possible field $\widetilde{\mathbf{w}}$ do not coincide with LCS intersections extracted as FTLE ridges, compare Figure 8.31b. These observations support our hypothesis that as soon as the steady-as-possible field is not sufficiently time-independent, methods from steady vector field visualization can no longer be used to infer properties of the original field (Hypothesis 7.1). This is not only true for hyperbolic trajectories but also for vortex cores. Conversely, we may still apply these methods in the corresponding space-time field of the steady-as-possible field, meaning both $\widetilde{\mathbf{w}}$ and $\mathbf{w}$, because the time-derivative of these fields is still significantly lower than the one of the original field $\mathbf{u}$.

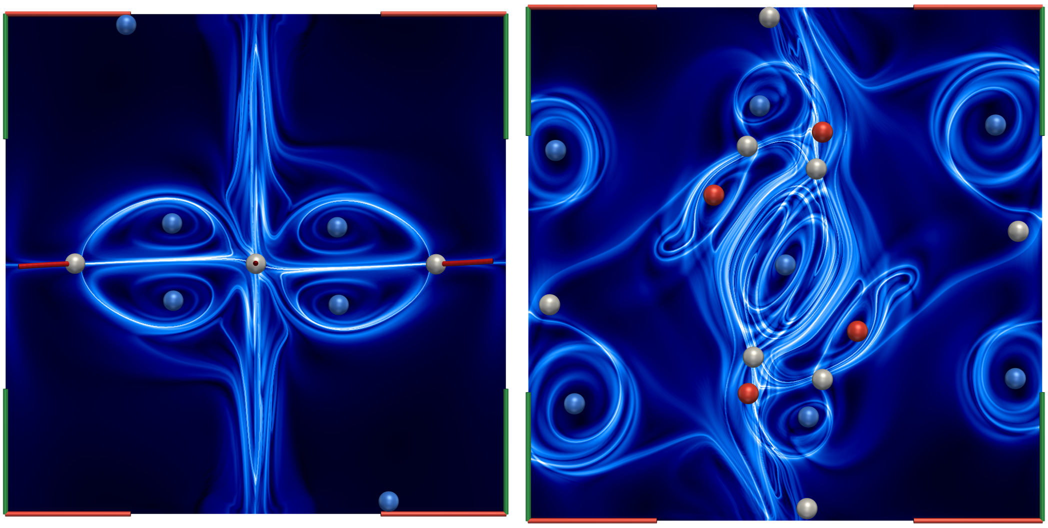

(a) $t = 0.5s$ (b) $t = 1.5s$

Figure 8.31: Buoyant plumes dataset: Superimposed forward and backward FTLE at $t = 0.5s$ (a) and at $t = 1.5s$ with advection time $T = \pm .5s$. Hyperbolic trajectories extracted as bifurcation lines (red tubes) and objective saddle-type critical points in the steady-as-possible field ([Had*19]).

8.3.3 Hotroom

The hotroom dataset is a 2D fluid simulation of a container with two obstacles, shown in blue in Figure 8.32a, The container is rotated 90° to the right. In the original setting, the top plate is cooled and the bottom plate is heated, i.e., corresponding to the right and left plates in Figure 8.32. The resulting turbulent motion within the container generates a number of critical point bifurcations. Thus, this is a prime example for to further investigate our findings from Section 8.2.

Question Q.1: Steadification Similar to the results from Section 8.3.2, due to a high number of fold bifurcations, none of the three methods is able to find frames of reference in which the original field appears steady. However, we know from Section 8.2 that these only introduce short-lived distortions. For example, the method of Hadwiger et al. [Had*19] is able to find steady frames up until the bifurcation occurs and right after it occurs. Thus, the impact in the resulting field steady-as-possible field is limited in time. We found correctly detected hyperbolic trajectories, see Figure 8.34, and false positive, see Figure 8.33. As discussed earlier, since this dataset simulates an incompressible fluid, the original field is divergence free, rotating motion is captured by center type critical points. Numerically, these are detected as attracting or repelling depending on the time-step. Hence, no real Hopf bifurcation occur in this case.

Question Q.3: Transfer of Methods Figure 8.33 shows hyperbolic trajectories extracted by the methods in question. Although we have seen that none of the frameworks is able to steadify a vector field that contains saddle-node bifurcations, hyperbolic trajectories can be extracted with these techniques to a varying degree of accuracy. The reference extraction as raw bifurcation line in space-time (Figure 8.34a) indeed separates the flow. However, the angle between feature and flow shows high local deviation, which are likely caused by the curved nature of the feature line at these locations. All three frameworks are able to find a similar hyperbolic trajectory. The quality of which is comparable between the hyperobjective and objective method of Günther et al. [GGT17; GT18a], see Figures 8.34c and 8.34d. In relation to the raw PV solution for the bifurcation line, large parts of the extracted line have a high feature angle. Nevertheless, pathlines are separated by this solution. Qualitatively high results are found by the framework of Hadwiger et al. [Had*19]. Compared to the other three methods, including the extraction as raw PV solution for bifurcation lines, this solutions separates the original flow, while exhibiting the lowest derivation in terms of feature angles, compare Figure 8.34b. Finally, we note that all solutions obtained require further fitting to a pathline, as indicated by the presence of (locally) high feature angles $> 5°$. The fact that the steady-as-possible field contains critical point bifurcations, and thus, is locally not steady, questions the applicability of extraction techniques from the steady realm. Figure 8.33 shows that all three frameworks detect saddle-type critical points that do not correspond to hyperbolic trajectories in the original field. This is shown by the absence of a FTLE ridges near the extracted points and by the pathlines of the original field that are not separated by the respective points. In the depicted cases, the objective saddle and node-type critical point are shortly before dissolving. Thus, fold bifurcations in real world datasets also introduce false detections in the steady-as-possible field. Therefore, visualization techniques for steady vector field cannot, or only very limited, be used to extract information from the steady-as-possible field.

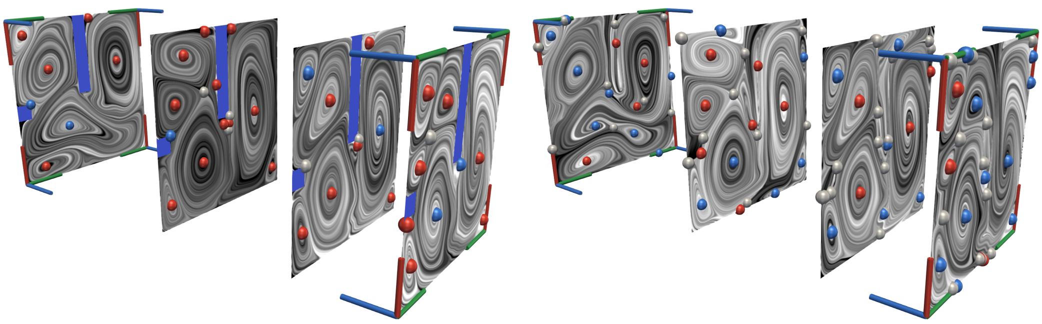

(a) Original Field $\mathbf{u}$ (b) Steady-as-possible field $\widetilde{\mathbf{w}}$ [Had*19]

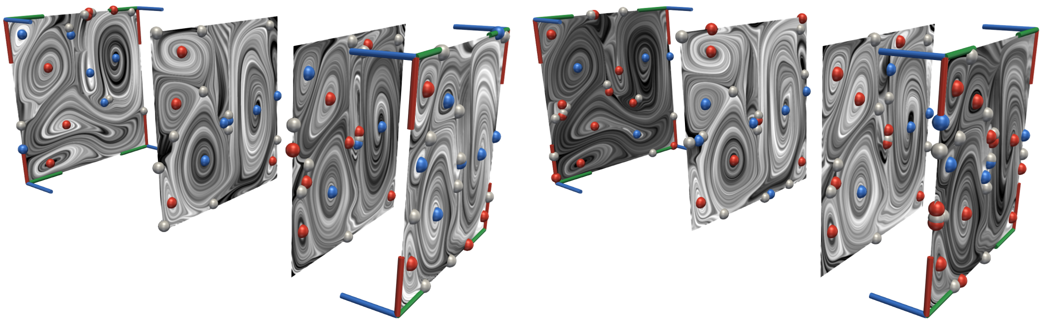

(c) Steady-as-possible field $\widetilde{\mathbf{w}}$ [GGT17] (d) Steady-as-possible field $\widetilde{\mathbf{w}}$ [GT18a]

Figure 8.32: The hotroom dataset in space-time with LICs at $t = 0s, 7s, 14s, 20s$ of the original field $\mathbf{u}$ and respective observed fields $\widetilde{\mathbf{w}}$. Critical points are shown as spheres with color coded stability.

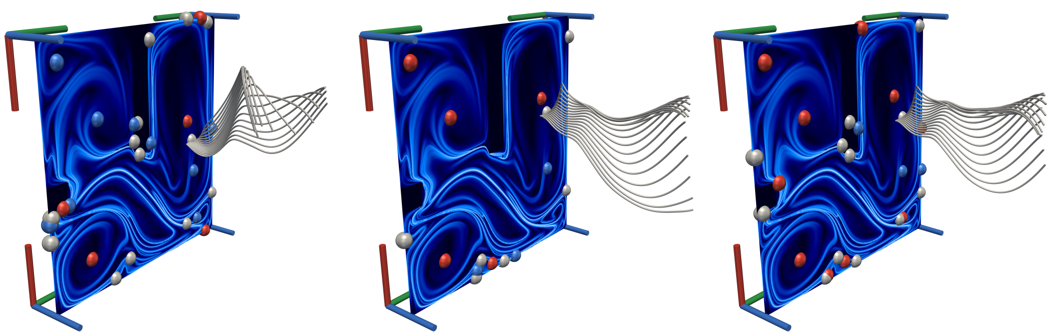

(a) Hadwiger et al. (b) Günther et al. (c) Günther and Theisel

Figure 8.33: Hotroom dataset: Superimposed forward backward FTLE at $t = 0.5s$ with advection time $T = \pm 0.5s$. Saddle-type critical points in the respective steady-as-possible fields shortly before a saddle-node bifurcation with an unstable critical point occurs. Pathlines of the original field show that none on these points separate in forward time.

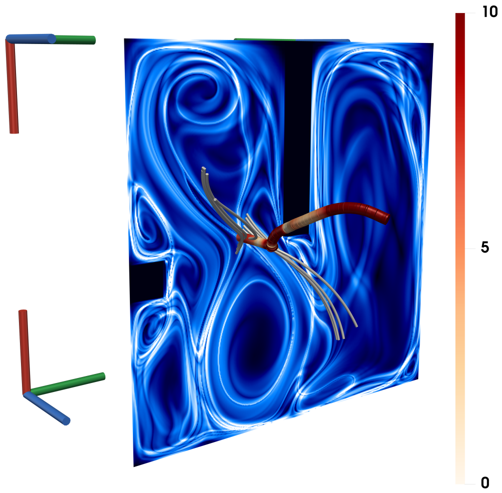

(a) Raw Bifurcation Line

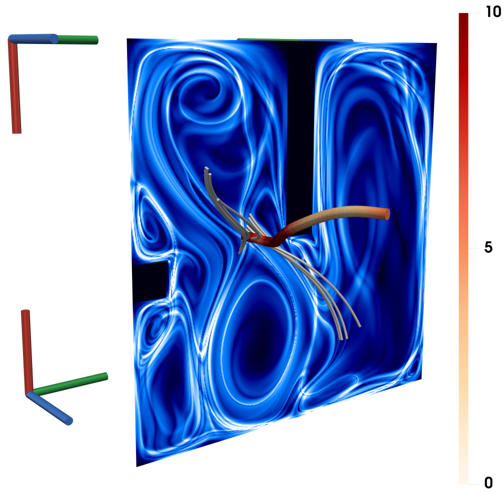

(b) Objective Saddle [Had*19]

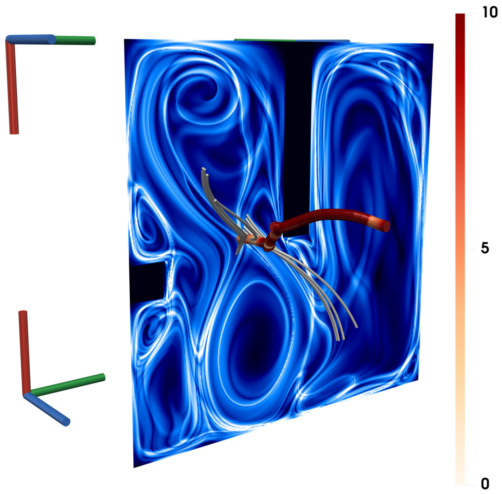

(c) Objective Saddle [GGT17]

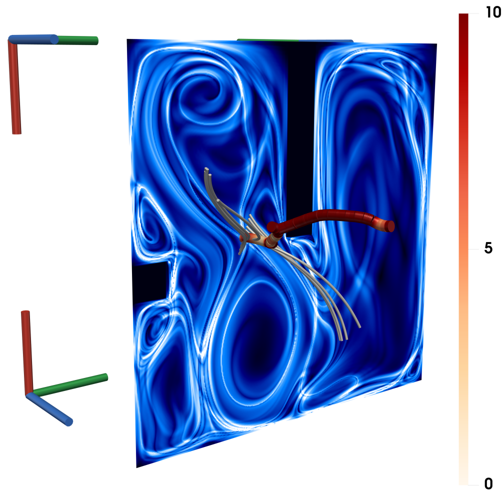

(d) Objective Saddle [GT18a]

Figure 8.34: Superimposed forward and backward FTLE of the hotroom dataset at $t = 2s$ with advection time $T = \pm 1s$. A hyperbolic trajectory extracted as raw bifurcation line (a) and as objective saddle by the respective methods (b),(c) and (d). All trajectories separate the original flow as indicated by pathlines in space-time (grey tubes). Corresponding feature angles are color mapped, where the framework of Hadwiger et al. [Had*19] (b) performs best.

8.4 Discussion

We evaluated the two frameworks of Hadwiger et al. [Had*19] and Günther et al. [GGT17; GT18a] on analytical (Section 8.1) as well as on real-world datasets (Section 8.3). In this section we summarize our findings and show how they relate to our initial hypotheses from Chapter 7.

We have argued in Chapter 7 that the frameworks can only find (local) frame of reference in which the original vector field appears steady if this field can be decomposed into a time-dependent component consisting of rigid body motion, or affine motion in case of the hyperobjective method [GT18a], and a time-independent part that captures other flow phenomena. By our choice of analytical and simulated datasets we showed that this vector fields containing fold bifurcations cannot be decomposed in this way. Furthermore, we showed that only the framework of Hadwiger et al. [Had*19] is able to compute such frames of reference for datasets containing Hopf bifurcations. However, this implies that essential information of the original vector field is carried by the observer velocity field. Therefore, in cases where the dataset contains Hopf bifurcation, the observer velocity fields needs to be considered during the visualization process. With this we can answer Question Q.1, concerning the ability to find frames of reference in which general vector fields appear steady. Table 8.1 gives an overview of the steadiness of the steady-as-possible fields for the analytical datasets tested. The three frameworks are all able to extract the motion of a single global observer, as it is the case for the four centers model, the two gyre saddle models and he quad gyre model. Hopf bifurcation can be absorbed by the method by Hadwiger et al. [Had*19] but neither the objective nor the hyperobjective method of Günther et al. [GGT17; GT18a] achieves this. Finally, as soon as a dataset exhibits saddle-node bifurcations, all methods fail. Table 8.2 shows this for the buoyant plumes and the hotroom dataset. In case of the von-Kármán vortex street all three methods find a suiting frame of reference, if we ignore bifurcations directly behind the obstacle. In our analytical test, we showed that if a single global observer can be extracted, all methods are able to compute such a frame of reference. A possible strategy to mitigate the problems associated with fold bifurcations in this context, could be to split the time-domain of a vector field into parts where no bifurcation occurs, and compute the optimal frames in between these events. Our implementation of this technique showed. however, this introduces discontinuities in the observer velocity field, i.e., the steady-as-possible field is C^0 continuous at boundaries between different segments. An C^0 continuous steady-as-possible field resulted unsatisfactory results in our test cases.

With such a steady frame of reference, Hypothesis 7.1 holds, and visualization techniques from steady vector field visualization can be translated to the time-dependent case. However, for features like separatrices this only holds as long as the observer motion described by the observer vector fields is the one of a single global observer (Hypothesis 7.4). Hence, Question Q.3, can be answered for both vortex core lines and hyperbolic trajectories. We may use critical points of the steady-as-possible field, given it is sufficiently time-independent, to extract these features.

Dataset	Four Centers	Gyre Saddle	Quad Gyre	Saddle-Node	Hopf
[Had*19]	✓	✓	✓	×	✓
[GGT17]	✓	✓	✓	×	×
[GT18a]	✓	✓	✓	×	×

Table 8.1: Steadification results for analytical models.

Dataset	Von-Kármán Vortex Street	Buoyant Plumes	Hotroom
[Had*19]	(✓)	×	×
[GGT17]	(✓)	×	×
[GT18a]	(✓)	×	×

Table 8.2: Steadification results for simulated datasets.

Concerning, Hypothesis 7.2, we proved in Section 8.1.1 that critical points in the steady-as-possible field correspond to loci where the original field and the observer field are parallel $\mathbf{u} \parallel \mathbf{v} \Leftrightarrow \mathbf{w} = \mathbf{0}$. We have seen in both analytical and simulated datasets, that solutions obtained as objective critical points or as PV or the original and the observer field, are not necessarily tangent curves of the original field. Therefore, we propose (Hypothesis 7.3), that these solutions require fitting similar to raw PV solutions for bifurcation lines [Mac*16].

Another important realization is that even if the observed field $\mathbf{w}_r$ is not time-independent, we may apply vortex core or bifurcation line extraction in the space-time variant of $\mathbf{w}_r$. This has two important advantages:

- The observer field $\mathbf{w}_r$ is (hyper) objective, regardless of its time-dependence.
- Curved core lines or bifurcation lines may appear less curved or even straight in the observed field $\mathbf{w}_r$. Thus, underestimation of the curvature of the core line can be mitigated by applying the respective PV techniques in the objective frame of reference and later transform the solutions back to the lab frame.

8.4.1 Extension to Three Dimensions

All three methods discussed, were originally presented for both two and three dimensional time-dependent vector fields. Hence, the research tasks formulated in Chapter 7 carry over to the three-dimensional case. Definitions for vortex core/region criteria [Wei*07b], as well as for streak-based vector field topology [ÜSE13] and hyperbolic trajectories exist. Their extraction requires parallel vectors solutions in 4D space. Weinkauf et al. [Wei*07b] presented their coplanar vectors operator that works on 3D space-time data by reducing the problem back to three dimensions.

Concerning the steadification of general 3D vector fields, we can follow our argumentation from the two dimensional case. Saddle-node bifurcations can also be found in higher-dimensional dynamical systems [Kuz06]. Subsequently, it is to expect that neither of the aforementioned techniques is able to find a frame of reference in which such phenomena appear steady. This directly shows, methods from 3D steady vector field visualization can not be transferred to the time-dependent case when fold bifurcations occur within the dataset. Our earlier argument, that, parallel (coplanar) vectors may be applied in the space-time version of the steady-as-possible field, i.e., in 4D, still holds, and indeed such methods become objective with this procedure. For the 2D time-dependent case we showed in Equation (4.11) that the application of parallel vectors in space-time implies equality of the two vector fields involved. We proved this using the 3D cross product $\mathbf{u} \parallel \mathbf{v} \Leftrightarrow \mathbf{u} \times \mathbf{v} = \mathbf{0}$. A possible proof of this in 3D space-time, would require the extension of the cross product to higher dimensions. The wedge product could serve as this extension. Thus, the proof does not directly translate to the 3D time-dependent case. Since our reasoning for Equation (8.4) builds on the implied equality of the previous result, we currently cannot confirm that parallel (coplanar) vector of the original and observer field are equivalent to critical points in the steady-as-possible field.

Nevertheless, our findings regarding the quality of steady-as-possible fields from Hadwiger et al. [Had*19] and Günther et al. [GGT17; GT18a] can follow our reasoning. Meaning, the global approach of Hadwiger et al. directly optimizes for similar-as-possible observers, while the two local approaches [GGT17; GT18a] suffer from a missing direct link between neighboring observers. This suggests that the problems concerning the physical interpretation of these methods persist. Computation times, on the other hand, are in both cases dependent on the number of nodes n. In case of regular grids, we can employ summed area tables for the framework of Günther et al. and the time complexity is $\mathcal{O}(n)$. For the framework of Hadwiger et al., the complexity analysis is more complex since it depends on the condition number of matrix A constructed from the Killing energy, the Lie derive and the regularization term of the original vector field. From our previous tests, we can infer that the global optimization is memory bound and with an increase in dimension, this poses a serious obstacle. In addition, reported timings in Table 8.3 suggest that the computation times increase significantly with an increase in dimension.

8.4.2 Performance Analysis

We have seen that the framework of Hadwiger et al. [Had*19] provides the best results in our test cases. It is the only method that is able to steadify Hopf bifurcations, and, generally provides higher flexibility by allowing the user to manipulate the weights that trade-off local rigid body motion and steadiness of the observed field. Nonetheless, a direct comparison of the measured residual is not possible, since the residuals of Hadwiger et al. [Had*19] are of global nature and the ones from Günther et al. depend on the neighborhood and cannot easily be translated to a global residual. The better results of Hadwiger et al. [Had*19] are achieved by the use of a global optimization over the entire space-time domain, making it computationally expensive. Both approaches of Günther et al. [GGT17; GT18a] use local neighborhoods where they find optimal frames of reference. This waives the direct connection between neighboring points and, thus, global phenomena, such as limit cycles, cannot be represented. Regarding the quality of the steady-as-possible field (Question Q.2.1) the global optimization of Hadwiger et al. [Had*19] results in coherent observer fields, while the local approaches introduce distortions. This is especially true for the hyperobjective method. Therefore, Question Q.2.2 favors the observer field from Hadwiger et al. [Had*19], which can be interpreted as a global observer that introduces (slight) local distortions but in general follows the original field. The lack of a direct connection between observers in case of the (hyper) objective methods [GGT17; GT18a], makes the interpretation dependent on the specific case. For the hyperobjective method this goes even further, where hardly any interpretation is possible without inspecting the individual case.

These drawbacks are partially compensated by the improvement in computation times (Question Q.2.3). Tables 8.3 and 8.4 show that the objective method [GGT17] is roughly two magnitudes faster than the global optimization by Hadwiger et al. [Had*19], and the hyperobjective method [GT18a] is still a magnitude faster. Either methods can be employed as preprocessing, but depending on the size of the dataset, only the local framework [GGT17; GT18a] can be used interactively. For regular grids, the computation times of the two local approaches may be further reduced to a complexity of $\mathcal{O}(n)$ by the use of summed area tables (see Section 6.1).

Concerning the neighborhood size of the local framework, we discussed that a priori knowledge is required for the correct extraction of certain phenomena, although their extracted location only varies slightly. The steadiness of the observed field is also dependent on this parameter. Generally, smaller neighborhood sizes correspond to a smaller time-derivative of the observed field. Smaller neighborhood size further decrease similarity between neighboring observers, i.e., this trades steadiness for smoothness of the steady-as-possible field. Table 8.4 shows the results for all datasets used with various neighborhood sizes. Günther et al. [GGT17; GT18a] propose a method to collapse the neighborhood size to a single point. This method of computation the observer velocity field has the advantage that it does no long depend on the discrete neighborhood. but requires third-order derivatives of the original field, which are less numerically stable. The approach of Hadwiger et al. [Had*19] has no discrete neighborhood, and only requires first-order derivatives of the original field, making it more numerically stable. We note that both frameworks suffer from boundary issues when constructing the steady-as-possible field $\mathbf{w}_r$ as discussed in Section 3.3.1. Neither Hadwiger et al. [Had*19] nor Günther et al. [GGT17; GT18a] discuss these problems in their original proposals. Our proposal addresses these issues with easily implementable boundary treatments.

Data Set	Figure	Grid $D \times T$	Hadwiger et al.			Time	Residual
			λ, μ	Tolerance	Iterations		
Rigid Vortex	6.2	$50^2 \times 100$	$1, 0.01$	1.0×10^{-10}	1.5×10^5	$59.21s$	2.219×10^{-5}
Four Centers (PC)	8.3 to 8.6	$64^2 \times 64$	$1, 0.01$	1.0×10^{-6}	1.0×10^5	$72.47s$	3.152×10^{-1}
von-Kármán Vortex Street	8.24 to 8.28	$400 \times 50 \times 301$	$1, 0.01$	1.0×10^{-6}	1.0×10^5	$1953.55s$	1.834×10^2
Gyre Saddle Linear	8.8 to 8.12	$50^2 \times 100$	$1, 0.01$	1.0×10^{-10}	1.5×10^5	$38.1s$	1.116×10^{-4}
Gyre Saddle Rotating	8.7 to 8.14	$50^2 \times 200$	$1, 0.01$	1.0×10^{-10}	1.5×10^5	$82.99s$	3.381×10^{-4}
Quad Gyre	8.15 to 8.18	$50^2 \times 200$	$1, 0.01$	1.0×10^{-8}	1.0×10^5	$191.04s$	5.322×10^{-6}
Saddle-Node Bifurcation	8.19 to 8.21	$20^2 \times 100$	$1, 0.01$	1.0×10^{-10}	1.5×10^5	$80.89s$	2.945×10^{-1}
Hopf Bifurcation	8.22 and 8.23	$20^2 \times 100$	$1, 0.01$	1.0×10^{-10}	1.5×10^5	$196.54s$	3.045×10^{-2}
		$50^2 \times 100$	$1, 0.01$	1.0×10^{-10}	1.5×10^5	$1250.19s$	3.766×10^3
Buoyant Plumes	8.29 to 8.31	$98^2 \times 371$	$1, 0.01$	1.0×10^{-8}	1.0×10^5	$1257.6s$	3.353×10^0
Hotroom	8.32 to 8.34	$100^2 \times 251$	$1, 0.01$	1.0×10^{-8}	1.5×10^5	$925.75s$	2.994×10^1

Table 8.3: Datasets and computation times for the approximate killing vector fields method by Hadwiger et al. [Had*19].

Data Set	Figure	Grid $D \times T$	Günther et al. Mode	Günther et al. U	Time	Avg. Residual
Rigid Vortex	6.2	$50^2 \times 100$	objective	21	$1.69s$	9.968×10^{-2}
			objective	41	$5.04s$	2.333×10^{-2}
			affine	21	$9.18s$	7.371×10^{-11}
			affine	41	$30.01s$	9.565×10^{-11}
Four Centers (PC)	8.3 to 8.6	$64^2 \times 64$	objective	21	$2.25s$	2.229×10^{-3}
			objective	41	$8.59s$	2.396×10^{-3}
			affine	21	$12.74s$	1.930×10^{-3}
			affine	41	$45.16s$	2.130×10^{-3}
von-Kármán Vortex Street	8.24 to 8.28	$400 \times 50 \times 301$	objective	21	$53.67s$	9.279×10^{-2}
			objective	41	$741.74s$	1.173×10^{-1}
			affine	21	$658.56s$	8.274×10^{-2}
			affine	41	$1330.68s$	9.391×10^{-2}
Gyre Saddle Linear	8.8 to 8.12	$50^2 \times 100$	objective	21	$1.14s$	2.579×10^{-2}
			affine	21	$10.14s$	2.769×10^{-2}
Gyre Saddle Rotating	8.7 to 8.14	$50^2 \times 200$	objective	21	$1.87s$	7.241×10^{-2}
			affine	21	$10.29s$	2.271×10^{-2}
Quad Gyre	8.15 to 8.18	$50^2 \times 200$	objective	21	$4.02s$	1.103×10^{-2}
			affine	21	$20.96s$	7.096×10^{-3}
Bifurcation Saddle-Node	8.19 to 8.21	$20^2 \times 100$	objective	21	$1.78s$	3.446×10^{-11}
			objective	41	$5.48s$	8.299×10^{-11}
			affine	21	$9.39s$	5.025×10^{-10}
			affine	41	$30.98s$	5.973×10^{-10}
Bifurcation Hopf	8.22 and 8.23	$20^2 \times 100$	objective	21	$1.55s$	1.058×10^{1}
			objective	10	$0.75s$	3.766×10^{0}
			objective	5	$0.35s$	1.769×10^{0}
		$50^2 \times 100$	objective	21	$3.75s$	2.701×10^{0}
			objective	10	$2.35s$	9.437×10^{-1}
			objective	5	$1.37s$	3.792×10^{-1}
			affine	21	$9.27s$	8.493×10^{-8}
			affine	10	$4.32s$	3.187×10^{-7}
			affine	5	$2.96s$	4.136×10^{-7}
Buoyant Plumes	8.29 to 8.31	$98^2 \times 371$	objective	21	$34.41s$	6.702×10^{0}
			affine	21	$214.32s$	5.637×10^{0}
Hotroom	8.32 to 8.34	$100^2 \times 251$	objective	21	$24.58s$	1.845×10^{0}
			affine	21	$151.19s$	1.516×10^{0}

Table 8.4: Datasets and computation times for Günther et al. [GGT17; GT18a].

9 Conclusion

In this thesis, we primarily focused on the frame (in)dependence of feature extraction techniques. We reviewed the mathematical basis of steady vector field topology, Lagrangian coherent structures (LCS), the finite-time Lyapunov exponent (FTLE), hyperbolic trajectories and finally vector field decompositions. Our study of the mathematical foundations of frames of reference proved useful when we evaluated recently proposed techniques that aim to make any feature extraction techniques invariant under certain observer motion.

The dependence of these feature extraction methods on the frame of reference has recently gained traction in literature with the introduction of the frameworks by Hadwiger et al. in 2019, and Günther et al. in 2017/18. We found that these techniques are not limited to vortex core/region criteria, but may be used to extract hyperbolic trajectories. Moreover, we proposed to apply parallel vectors in the steady-as-possible field, and showed that this mitigates problems related to curved PV solutions. We compared this to the traditional extraction method as bifurcation lines in space-time. This led us to the study of streak-based vector field topology, i.e., time-dependent vector field topology, in the context of the aforementioned frameworks that claim to find (local) frames of reference in which time-dependent vector fields appear steady. The investigation of these claims revealed that fold bifurcations, i.e., the birth and death of critical points, pose a fundamental problem for the steadification of vector fields. We showed that these problems cannot be mitigated by splitting the time-domain in pieces where no fold bifurcations occur. Further, we explored the application of these methods to Hopf bifurcations, i.e., events where a limit cycle emerges, and determined that they present a similar obstacle as fold bifurcations, that is overcome only by the approach of Hadwiger et al. Thereby we proved that, neither of the three methods is able to provide such steady frames of reference in general. We further argued that the absorbed limit cycle in the observer field from the technique of Hadwiger et al. contains essential information that is now present in the observer field and not in the steady-as-possible field. Therefore, we assert that the observer field may no longer be discarded during feature extraction and visualization. This significantly impacts the extraction of hyperbolic trajectories as critical points in the steady-as-possible field. In addition, we found that even when a steady frame of reference is found, separatrices can only be transformed into the original frame when the observer motion is uniform, i.e., describes the motion of a single global observer. In cases where the steady-as-possible field exhibits significant change over time, our results illustrate that the objective steady-as-possible frame still improves the extraction of vortices and hyperbolic trajectories by traditional methods. We discussed that these findings translate analogously to the three-dimensional case by the use of the coplanar vectors operator from Weinkauf et al. For the two-dimensional case we proved two equivalences of techniques: 1) Critical points in the steady-as-possible field coincide with parallel vector solutions of the original field and the observer field. 2) Parallel vectors according to Sujudi and Haimes in the steady-as-possible field coincide with critical points.

We compared the frameworks of Hadwiger et al., and Günther et al. in terms of the quality of the resulting steady-as-possible vector field, the physical interpretation of the observer velocity field and their computation times. In summary, the approach of Hadwiger et al. produces qualitatively better results but comes with a computational expensive global optimization. The significantly lower computational costs of Günther et al. yield a high price in quality and smoothness of the results, as well as a notable decrease in interpretability. Moreover, with our GPU implementation we illustrated that the method of Hadwiger et al. is mostly memory bound, and thus, cannot be parallelized easily in this way.

In both cases we showed that issues arise when domain boundaries, as it is the case with real-world datasets, exist and propose easy to implement boundary treatments. Finally, we put these methods in context to other vector field decompositions like the Helmholtz-Hodge decomposition. The framework of Hadwiger et al. uniquely identifies such a decomposition, while the other methods of Günther et al. do not.

9.1 Future Work

Based on our finding that the observer velocity field needs to be considered when interpreting the results of these methods, we suggest to include visualization techniques for the observer velocity field. An idea could be representing the domain as a glass lense and distort it according to the shear and other influences present in the observer field. Further, visualization of physical properties, e.g., different types of energies of the observer fields, could provide additional insight into their physical interpretation. Future work could include a quantification of time-dependence of the steady-as-possible field which could function as an error estimation of features extracted. For a complete extension to three dimensions of the insights gained from this work, the implications of parallel (coplanar) vectors in 3D space-time need to be studied. However, if it turns out that parallel vectors in 3D space-time imply equality of the vectors analogously to the 2D case, the findings concerning PV of the observer and steady-as-possible field translate directly. We have discussed that splitting the time domain when using the technique of Hadwiger et al. results in unsatisfactory results. A different approach could be splitting the space-domain, and compare this to the techniques of Günther et al. with similar neighborhood size. Our implementation of raw PV solutions currently only use the original proposal of Machado et al. to find bifurcation lines in space-time. They suggested to use the higher-order method from Roth and Peikert, which could be considered in this case as well. A mathematically vigorous argumentation of the relation between critical points in the steady-as-possible field and parallel vector loci in the original field could be addressed. Since FTLE is not invariant under these local frames of reference transformations, an investigation into relation between the FTLE of the original field and the steady-as-possible field could be of interest.

A Algorithms

A.1 Discretization Aspects

Vector and scalar fields from simulations or measurements are typically provided as discretized data. In these cases, a representation containing values for a set of underlying points, i.e., a spatial discretization into a grid, is a common approach. Most common grid types are constructed out of geometric primitives: triangles, or quads in 2D, tetrahedra, pyramids, prisms, and hexahedra, and other, in 3D. We distinguish two major types of grids: unstructured grids, where the topology has to be explicitly provided, and structured grids, where the topology is given implicitly. A structured 2D grid consists of a set of nodes $N_{x_0,y_0}, \cdots, N_{x_n,y_m}$, and cells, where each cell C is formed by four nodes $(N_{x_i,y_j}, N_{x_{i+1},y_j}, N_{x_i,y_{j+1}}, N_{x_{i+1},y_{j+1}})$. Each node corresponds to a position $\mathbf{x}$ in space. Consequently, the data vector $\mathbf{w}$ (often $\mathbf{w} \in \mathbb{R}^p, p \in \{1,2,3\}$) can be stored per node (node-based), or cell (cell-based).

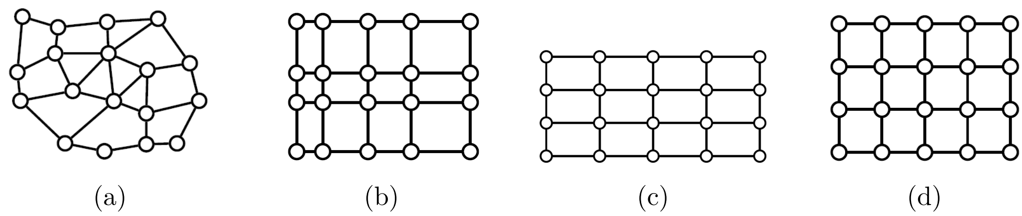

Figure A.1: Grid types. Unstructured grid (a). Rectilinear grid (b). Uniform grid (c). Cartesian grid (d). Images from Sadlo [Sad10].

A.1.1 Numerical Integration of Differential Equations

In order to numerically compute tangent curves of a vector field, we have to solve the corresponding initial value problem (IVP) of an ordinary or partial differential equation (ODE/PDE). This is done by numerical integration, which yields an approximation of the solution to a given differential equation. However, this is only an approximation of the analytical solution. The choice of the numerical integration scheme and the step size influences the accuracy of the resulting curve. Given an autonomous dynamical system

$$\dot{\mathbf{x}}(t) = \mathbf{u}(\mathbf{x}), \quad \mathbf{x}(t_0) = \mathbf{x}_0. \tag{A.1}$$

Although the following examples only cover autonomous dynamical systems, they integration schemes also work for non-autonomous systems. For schemes using intermediate steps, the intermediate steps need to be computed in space and time. The explicit Euler scheme offers a simple integration of the aforementioned IVP:

$$\mathbf{x}(t+\Delta t) = \mathbf{x}(t) + \Delta t \mathbf{u}(\mathbf{x}, t). \tag{A.2}$$

With the solution becoming more accurate with a smaller step size Δt. However, explicit euler scheme is a first-order method:

$$\mathbf{x}(t+\Delta t) = \mathbf{x}(t) + \Delta t \dot{\mathbf{x}}(t) + O(\Delta t^2). \tag{A.3}$$

To increase accuracy, higher-order methods are employed. We use a Runge–Kutta 4/5, also known as Runge–Kutta–Fehlberg scheme, which is of 4th-order and with 5th-order error estimator:

$$\begin{aligned}
\mathbf{k_1} &= \Delta t \mathbf{u}(\mathbf{x}, t) \\
\mathbf{k_2} &= \Delta t \mathbf{u}(\mathbf{x} + \frac{\mathbf{k_1}}{4}, t + \frac{1}{4}\Delta t) \\
\mathbf{k_3} &= \Delta t \mathbf{u}(\mathbf{x} + \frac{3}{32}\mathbf{k_1} + \frac{9}{32}\mathbf{k_2}, t + \frac{3}{8}\Delta t) \\
\mathbf{k_4} &= \Delta t \mathbf{u}(\mathbf{x} + \frac{1932}{2197}\mathbf{k_1} + \frac{-7200}{2197}\mathbf{k_2} + \frac{7296}{2197}\mathbf{k_3}, t + \frac{12}{13}\Delta t) \\
\mathbf{k_5} &= \Delta t \mathbf{u}(\mathbf{x} + \frac{439}{216}\mathbf{k_1} + \frac{-8}{1}\mathbf{k_2} + \frac{3680}{513}\mathbf{k_3} + \frac{-845}{4104}\mathbf{k_4}, t + \frac{1}{1}\Delta t) \\
\mathbf{k_6} &= \Delta t \mathbf{u}(\mathbf{x} + \frac{-8}{27}\mathbf{k_1} + \frac{2}{1}\mathbf{k_2} + \frac{-3544}{2565}\mathbf{k_3} + \frac{1859}{4104}\mathbf{k_4} + \frac{-11}{40}\mathbf{k_5}, t + \frac{1}{2}\Delta t) \\
\\
\mathbf{x_{RK4}}(t+\Delta t) &= \mathbf{x} + \frac{25}{216}\mathbf{k_1} + \frac{1408}{2565}\mathbf{k_3} + \frac{2197}{4104}\mathbf{k_4} + \frac{-1}{5}\mathbf{k_5} + O(\Delta t^5) \\
\mathbf{x_{RK5}}(t+\Delta t) &= \mathbf{x} + \frac{16}{135}\mathbf{k_1} + \frac{6656}{12825}\mathbf{k_3} + \frac{28561}{56430}\mathbf{k_4} + \frac{-9}{50}\mathbf{k_5} + \frac{2}{55}\mathbf{k_6} + O(\Delta t^6).
\end{aligned} \tag{A.4}$$

The **RK4** and **RK5** are of 4th and 5th order, respectively. To adapt the step size, the error indicator

$$\Delta_e = \|\mathbf{x_{RK5}} - \mathbf{x_{RK4}}\| \tag{A.5}$$

is introduced, and the new step size is computed as:

$$\Delta t' = \begin{cases} \Delta t \rho \sqrt[5]{\frac{\tau}{\Delta_e}} & \text{if } \tau \geq \Delta \\ \Delta t \rho \sqrt[4]{\frac{\tau}{\Delta_e}} & \text{if } \tau \leq \Delta, \end{cases} \tag{A.6}$$

with ρ being the safety factor and τ the desired error tolerance.

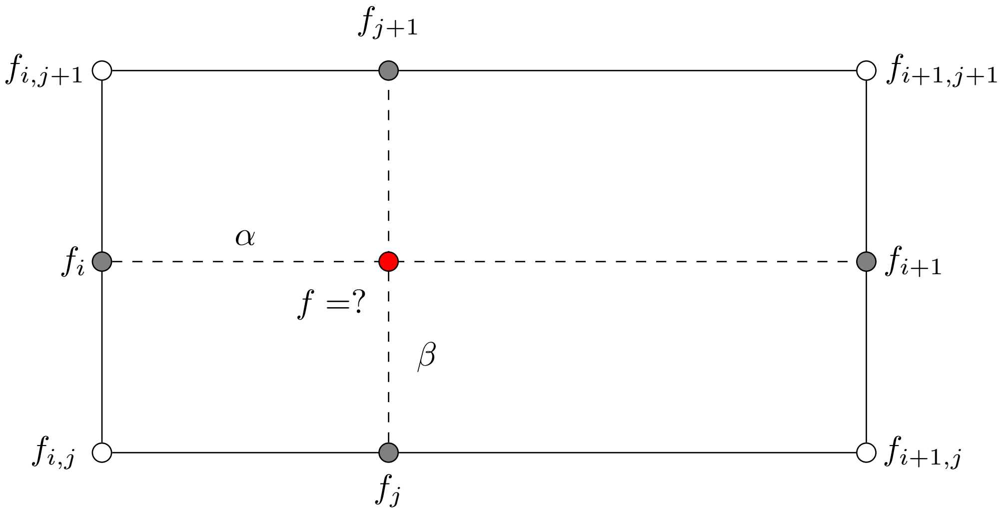

Figure A.2: Illustration of bilinear interpolation within a rectangle.

A.2 Interpolation

As mentioned before, datasets are often stored on a discrete grid, only providing values for each node. Hence, we use interpolation to retrieve a continuous data representation for each cell. For quad-based grids in 2D and hexahedron based grids in 3D we use bilinear interpolation for two-dimensional and trilinear interpolation for three-dimensional grids. Barycentric interpolation can be used for triangle based grids. The following interpolation schemes are only presented for scalar functions $f : \mathbb{R}^n \to \mathbb{R}$ but generalize directly to vector valued functions $\mathbf{g} : \mathbb{R}^n \to \mathbb{R}^m$.

A.2.1 Bilinear Interpolation

Given a rectangle based cell with vertices $\mathbf{x}_{i,j}, \mathbf{x}_{i+1,j}, \mathbf{x}_{i,j+1}, \mathbf{x}_{i+1,j+1}$, corresponding data values $f_{i,j}, f_{i+1,j}, f_{i,j+1}, f_{i+1,j+1}$, and a point $p = (x, y)$ inside the cell, the bilinear interpolated value $f(p) = f(x, y)$ is determined by:

$$\begin{aligned} f(x,y) &= (1-\alpha)(1-\beta)f_{i,j} + \alpha(1-\beta)f_{i+1,j} + (1-\alpha)\beta f_{i,j+1} + \alpha\beta f_{i+1,j+1} \\ &= (1-\beta)[(1-\alpha)f_{i,j} + \alpha f_{i+1,j}] + \beta[(1-\alpha)f_{i,j+1} + \alpha f_{i+1,j+1}] \\ &\text{with } \alpha = \frac{x - x_i}{x_{i+1} - x_i}, \quad \beta = \frac{y - y_j}{y_{j+1} - y_j}. \end{aligned} \tag{A.7}$$

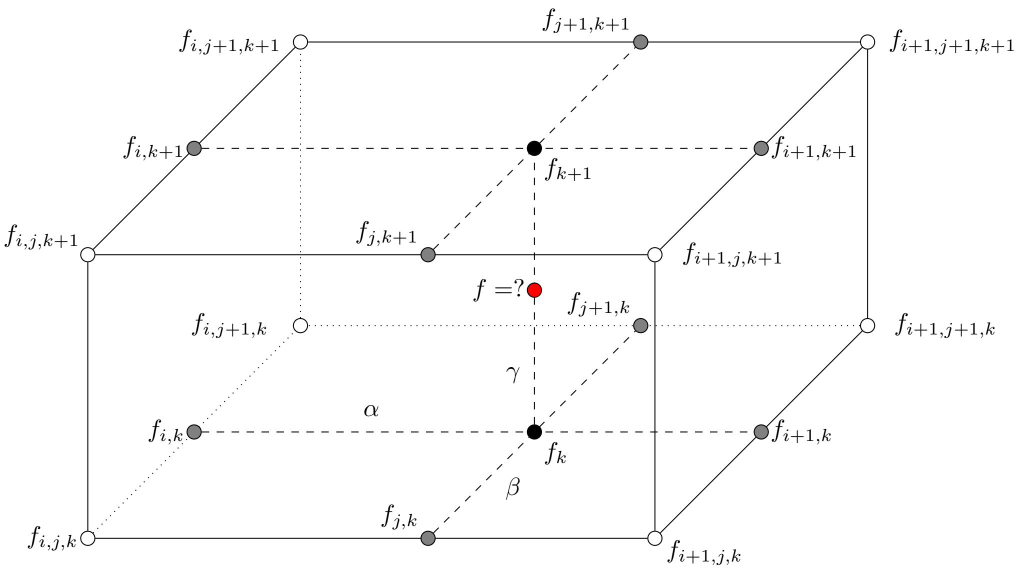

Figure A.3: Illustration of a trilinear interpolation within a rectangular cuboid.

α and β are in local coordinates, meaning, if the cell is not rectangular and axis aligned, we first have to compute f_j, f_{j+1} and f_i, f_{i+1} as:

$$\begin{aligned} f_j &= (1-\alpha)f_{i,j} + \alpha f_{i+1,j} \\ f_{j+1} &= (1-\alpha)f_{i,j+1} + \alpha f_{i+1,j+1} \\ f_i &= (1-\alpha)f_{i,j} + \alpha f_{i,j+1} \\ f_{i+1} &= (1-\alpha)f_{i+1,j} + \alpha f_{i+1,j+1}, \end{aligned} \tag{A.8}$$

and compute α and β from there:

$$\begin{aligned} \alpha &= \frac{\|\mathbf{x}_j - \mathbf{x}_{i,j}\|_2}{\|\mathbf{x}_{i+1,j} - \mathbf{x}_{i,j}\|_2}, \\ \beta &= \frac{\|\mathbf{x}_i - \mathbf{x}_{i,j}\|_2}{\|\mathbf{x}_{i,j+1} - \mathbf{x}_{i,j}\|_2}. \end{aligned} \tag{A.9}$$

Note that bilinear interpolation is quadratic, not linear.

A.2.2 Trilinear Interpolation

Similar to bilinear interpolation on a rectangular based cell, we can use trilinear interpolation inside a rectangular cuboid based cell to get a analytical representation

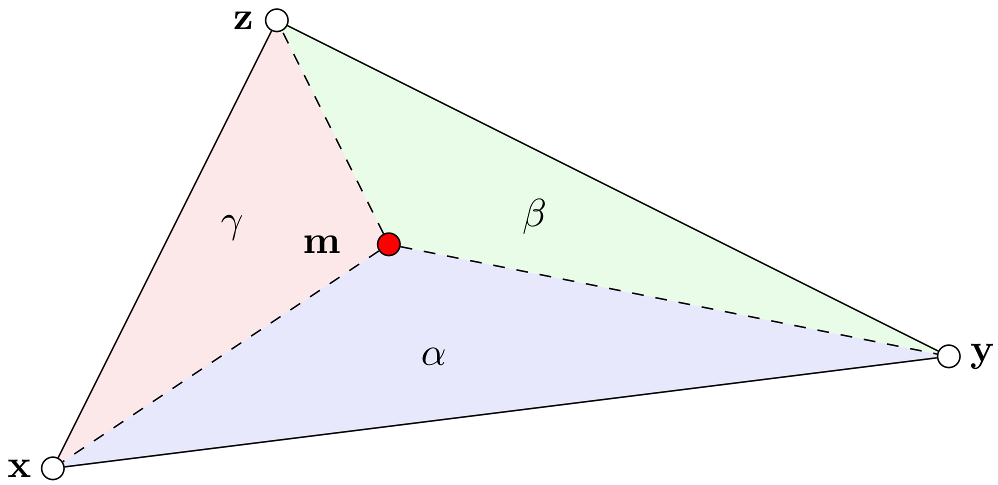

Figure A.4

of data inside the cell. With vertices $\mathbf{x}_{i,j,k}$, corresponding data values $f_{i,j,k}$, and point $p = (x, y, z)$ inside the cell, the trilinear interpolated value $f(p) = f(x, y, z)$ is:

$$\begin{aligned} f(x,y,z) = (1-\alpha)(1-\beta)(1-\gamma)f_{i,j,k} + \alpha(1-\beta)(1-\gamma)f_{i+1,j,k} + \\ \alpha\beta(1-\gamma)f_{i+1,j+1,k} + (1-\alpha)\beta(1-\gamma)f_{i,j+1,k} + \\ (1-\alpha)(1-\beta)\gamma f_{i,j,k+1} + \alpha(1-\beta)\gamma f_{i+1,j,k+1} + \\ \alpha\beta\gamma f_{i+1,j+1,k+1} + (1-\alpha)\beta\gamma f_{i,j+1,k+1}, \\ \text{with } \alpha = \frac{x-x_i}{x_{i+1}-x_i}, \quad \beta = \frac{y-y_j}{y_{j+1}-y_j}, \quad \gamma = \frac{z-z_i}{z_{i+1}-z_i}. \end{aligned} \tag{A.10}$$

α, β, and γ are in local coordinates and have to be calculated beforehand. This is done analogously to the bilinear case (A.8). Note that trilinear interpolation consists of a bilinear interpolation in x-y-direction, and an additional linear interpolation in z-direction, thus, trilinear interpolation is cubic. This scheme can be generalized to higher dimensions, by assigned the each vertex a weight equal to the portion of volume the opposite n-orthotope (higher dimensional cuboid).

A.2.3 Barycentric Interpolation

Barycentric is a linear interpolation method for triangles. Given a triangle with vertices $\mathbf{x}, \mathbf{y}$ and $\mathbf{z}$ and a point within the triangle $\mathbf{m}$, the barycentric coordinates of the center point $\mathbf{m}$ are given by the relative area of the sub-triangles α, β, and γ

$$r = \frac{\text{area}(\alpha)}{\text{area}(\alpha+\beta+\gamma)}, \quad s = \frac{\text{area}(\beta)}{\text{area}(\alpha+\beta+\gamma)}, \quad t = \frac{\text{area}(\gamma)}{\text{area}(\alpha+\beta+\gamma)}, \tag{A.11}$$

where area($\alpha + \beta + \gamma$) is the area of the entire triangle. If the vertices $\mathbf{x}, \mathbf{y}, \mathbf{z}$ are given positions in 3D space, the area can be computed as follows

$$\pm\mathbf{area}(\mathbf{x}, \mathbf{y}) = \frac{1}{2}\det\begin{pmatrix} x_1 & x_2 & x_3 \\ y_1 & y_2 & y_3 \\ 1 & 1 & 1 \end{pmatrix}. \tag{A.12}$$

With these coordinates, the position of $\mathbf{m}$ can be computed by weighting each vertex by the relative size of the sub-triangle on the opposite side.

$$\mathbf{m} = s\mathbf{x} + t\mathbf{y} + r\mathbf{z}. \tag{A.13}$$

Note that two of the coordinates suffice to compute the position of $\mathbf{m}$ because $t = 1 - (r + s)$. One may obtain the function value at position $\mathbf{m}$ of a vector valued function $\mathbf{f} : \mathbb{R}^n \to \mathbb{R}^m$ given for all vertices $\mathbf{x}, \mathbf{y}, \mathbf{z}$ by substituting the vertices with the function values in Equation (A.13)

$$\mathbf{f}(\mathbf{m}) = s\mathbf{f}(\mathbf{x}) + t\mathbf{f}(\mathbf{y}) + r\mathbf{f}(\mathbf{z}). \tag{A.14}$$

List of Figures

List of Tables

Acronyms

FFF	Feature flow field
FTLE	Finite-time Lyapunov exponent
HHD	Helmholtz-Hodge decomposition
IVP	Initial value problem
LCS	Lagrangian coherent structures
LIC	Line integral convolution
ODE	Ordinary differential equation
PCA	Principal component analysis
PDE	Partial differential equation
PV-Operator	Parallel vectos operator
SFFF	Stable feature flow field

Bibliography

[Asi93] D. Asimov. *Notes on the topology of vector fields and flows*. Technical report. Technical report, NASA Ames Research Center, 1993. RNR-93-003, 1993.

[BC*10] M. Ben-Chen, A. Butscher, J. Solomon, and L. Guibas. "On discrete killing vector fields and patterns on surfaces". In: *Computer Graphics Forum*. Volume 29. 5. Wiley Online Library. 2010, pages 1701–1711.

[Bha*13] H. Bhatia, G. Norgard, V. Pascucci, and P.-T. Bremer. "The Helmholtz-Hodge decomposition—a survey". *IEEE Transactions on visualization and computer graphics* 19:8, 2013, pages 1386–1404.

[Bha*14] H. Bhatia, V. Pascucci, R. M. Kirby, and P.-T. Bremer. "Extracting Features from Time-Dependent Vector Fields Using Internal Reference Frames". In: *Computer graphics forum*. Volume 33. 3. Wiley Online Library. 2014, pages 21–30.

[BHJ16] R. Bujack, M. Hlawitschka, and K. I. Joy. "Topology-inspired Galilean invariant vector field analysis". In: *Pacific Visualization Symposium (PacificVis), 2016 IEEE*. IEEE. 2016, pages 72–79.

[Bis*15] A. Biswas, D. Thompson, W. He, Q. Deng, C.-M. Chen, H.-W. Shenk, R. Machiraju, and A. Rangarajan. "An uncertainty-driven approach to vortex analysis using oracle consensus and spatial proximity". In: *2015 IEEE pacific visualization symposium (PacificVis)*. IEEE. 2015, pages 223–230.

[BPB14] H. Bhatia, V. Pascucci, and P.-T. Bremer. "The natural Helmholtz-Hodge decomposition for open-boundary flow analysis". *IEEE transactions on visualization and computer graphics* 20:11, 2014, pages 1566–1578.

[BR10] S. L. Brunton and C. W. Rowley. "Fast computation of FTLE fields for unsteady flows: a comparison of methods". *Chaos* 20:1, 2010, **page** 017503.

[Che*17] A. Chern, F. Knöppel, U. Pinkall, and P. Schröder. "Inside fluids: clebsch maps for visualization and processing". *ACM Transactions on Graphics (TOG)* 36:4, 2017, **page** 142.

[CL93] B. Cabral and L. C. Leedom. "Imaging vector fields using line integral convolution". In: *Proceedings of the 20th annual conference on Computer graphics and interactive techniques*. ACM. 1993, pages 263–270.

[CMM90] A. J. Chorin, J. E. Marsden, and J. E. Marsden. *A mathematical introduction to fluid mechanics*. Volume 3. Springer, 1990.

[Com14] W. Commons. *File:LightPaintingExample.jpg — Wikimedia Commons, the free media repository*. [Online; accessed 13-March-2019]. 2014. URL: https://commons.wikimedia.org/w/index.php?title=File:LightPaintingExample.jpg&oldid=113146075.

[Com18] W. Commons. *File:Aeroakustik-Windkanal-Messhalle.JPG — Wikimedia Commons, the free media repository*. [Online; accessed 13-March-2019]. 2018. URL: https://commons.wikimedia.org/w/index.php?title=File:Aeroakustik-Windkanal-Messhalle.JPG&oldid=285242030.

[DK91] A. Doi and A. Koide. "An efficient method of triangulating equi-valued surfaces by using tetrahedral cells". *IEICE Transactions on Information and Systems* 74:1, 1991, pages 214–224.

[DL76] R Drouot and M Lucius. "Approximation du second ordre de la loi de comportement des fluides simples. Lois classiques déduites de l'introduction d'un nouveau tenseur objectif". *Archiwum Mechaniki Stosowanej* 28:2, 1976, pages 189–198.

[Ebe*94] D. Eberly, R. Gardner, B. Morse, S. Pizer, and C. Scharlach. "Ridges for image analysis". *Journal of Mathematical Imaging and Vision* 4:4, 1994, pages 353–373.

[FP01] J. D. Furst and S. M. Pizer. "Marching ridges." In: *SIP*. 2001, pages 22–26.

[FSP12] R. Fuchs, B. Schindler, and R. Peikert. "Scale-space approaches to FTLE ridges". In: *Topological Methods in Data Analysis and Visualization II*. Springer, 2012, pages 283–296.

[Fuc*08] R. Fuchs, R. Peikert, H. Hauser, F. Sadlo, and P. Muigg. "Parallel vectors criteria for unsteady flow vortices". *IEEE Transactions on Visualization and Computer Graphics* 14:3, 2008, pages 615–626.

[GGT17] T. Günther, M. Gross, and H. Theisel. "Generic objective vortices for flow visualization". *ACM Transactions on Graphics (TOG)* 36:4, 2017, **page** 141.

[GH13] J. Guckenheimer and P. Holmes. *Nonlinear oscillations, dynamical systems, and bifurcations of vector fields*. Volume 42. Springer Science & Business Media, 2013.

[GST16] T. Günther, M. Schulze, and H. Theisel. "Rotation invariant vortices for flow visualization". *IEEE Transactions on Visualization & Computer Graphics* 1, 2016, pages 1–1.

[GT14] T. Günther and H. Theisel. "Vortex Cores of Inertial Particles". *IEEE Transactions on Visualization and Computer Graphics (Proc. IEEE Scientific Visualization)* 20:12, 2014, pages 2535–2544.

[GT18a] T. Günther and H. Theisel. "Hyper-Objective Vortices". *IEEE Transactions on Visualization and Computer Graphics*, 2018.

[GT18b] T. Günther and H. Theisel. "The State of the Art in Vortex Extraction". *Computer Graphics Forum* 37:6, 2018, pages 149–173.

[Guo*16] H. Guo, W. He, T. Peterka, H. Shen, S. M. Collis, and J. J. Helmus. "Finite-Time Lyapunov Exponents and Lagrangian Coherent Structures in Uncertain Unsteady Flows". *IEEE Transactions on Visualization and Computer Graphics* 22:6, 2016, pages 1672–1682. ISSN: 1077-2626. DOI: 10.1109/TVCG.2016.2534560.

[Had*19] M. Hadwiger, M. Mlejnek, T. Theußl, and P. Rautek. "Time-Dependent Flow seen through Approximate Observer Killing Fields". *IEEE transactions on visualization and computer graphics* 25:1, 2019, pages 1257–1266.

[Hal00] G. Haller. "Finding finite-time invariant manifolds in two-dimensional velocity fields". *Chaos: An Interdisciplinary Journal of Nonlinear Science* 10:1, 2000, pages 99–108.

[Hal01] G. Haller. "Distinguished material surfaces and coherent structures in 3-dimensional fluid flows". *Physica D: Nonlinear Phenomena* 149:4, 2001, pages 248–277.

[Hal05] G. Haller. "An objective definition of a vortex". *Journal of fluid mechanics* 525, 2005, pages 1–26.

[Hal11] G. Haller. "A variational theory of hyperbolic Lagrangian coherent structures". *Physica D: Nonlinear Phenomena* 240:7, 2011, pages 574–598.

[Hal15] G. Haller. "Lagrangian coherent structures". *Annual Review of Fluid Mechanics* 47, 2015, pages 137–162.

[Hal*16] G. Haller, A. Hadjighasem, M. Farazmand, and F. Huhn. "Defining coherent vortices objectively from the vorticity". *Journal of Fluid Mechanics* 795, 2016, pages 136–173.

[Hal80] J. Hale. "Ordinary differential equations". *RE Krieger Publ*, 1980.

[Har83] R. M. Haralick. "Ridges and valleys on digital images". *Computer Vision, Graphics, and Image Processing* 22:1, 1983, pages 28–38.

[Hei*16] C. Heine, H. Leitte, M. Hlawitschka, F. Iuricich, L. De Floriani, G. Scheuermann, H. Hagen, and C. Garth. "A survey of topology-based methods in visualization". In: *Computer Graphics Forum*. Volume 35. 3. Wiley Online Library. 2016, pages 643–667.

[Hel58] H. von Helmholtz. "Über Integrale der hydrodynamischen Gleichungen, welche den Wirbelbewegungen entsprechen." *Journal für Mathematik Bd. LV. Heft* 1, 1858, **page** 4.

[HH89] J. Helman and L. Hesselink. "Representation and display of vector field topology in fluid flow data sets". *Computer* 8, 1989, pages 27–36.

[HH91] J. L. Helman and L. Hesselink. "Visualizing vector field topology in fluid flows". *IEEE Computer Graphics and Applications* 3, 1991, pages 36–46.

[HRS18] L. Hofmann, B. Rieck, and F. Sadlo. "Visualization of 4D Vector Field Topology". *Computer Graphics Forum* 37:3, 2018, pages 301–313. DOI: 10.1111/cgf.13421.

[HS11] G. Haller and T. Sapsis. "Lagrangian coherent structures and the smallest finite-time Lyapunov exponent". *Chaos: An Interdisciplinary Journal of Nonlinear Science* 21:2, 2011, **page** 023115.

[Hun87] J. Hunt. "Vorticity and vortex dynamics in complex turbulent flows". *Transactions of the Canadian Society for Mechanical Engineering* 11:1, 1987, pages 21–35.

[HWM88] J. C. Hunt, A. A. Wray, and P. Moin. "Eddies, streams, and convergence zones in turbulent flows", 1988.

[JC16] I. T. Jolliffe and J. Cadima. "Principal component analysis: a review and recent developments". *Philosophical Transactions of the Royal Society A: Mathematical, Physical and Engineering Sciences* 374:2065, 2016, **page** 20150202.

[JH95] J. Jeong and F. Hussain. "On the identification of a vortex". *Journal of fluid mechanics* 285, 1995, pages 69–94.

[JJ08] J. Jost and J. Jost. *Riemannian geometry and geometric analysis*. Volume 42005. Springer, 2008.

[JMT05] M. Jian, R. Machiraju, and D. Thompson. "14 - Detection and Visualization of Vortices". In: *Visualization Handbook*. **byeditor**C. D. Hansen and C. R. Johnson. Butterworth-Heinemann, Burlington, 2005, pages 295 –309. ISBN: 978-0-12-387582-2. DOI: https://doi.org/10.1016/B978-012387582-2/50016-2. URL: http://www.sciencedirect.com/science/article/pii/B9780123875822500162.

[Jun*17] P. Jung, P. Hausner, L. Pilz, J. Stern, C. Euler, M. Riemer, and F. Sadlo. "Tumble-Vortex Core Line Extraction". In: *Proceedings of SIBGRAPI WVIS*. 2017.

[Kas*11] J. Kasten, J. Reininghaus, I. Hotz, and H.-C. Hege. "Two-dimensional time-dependent vortex regions based on the acceleration magnitude". *IEEE Transactions on Visualization and Computer Graphics* 17:12, 2011, pages 2080–2087.

[Kas*12] J. Kasten, I. Hotz, B. R. Noack, and H.-C. Hege. "Vortex merge graphs in two-dimensional unsteady flow fields". *EuroVis-Short Papers*, 2012, pages 1–5.

[Ken98] D. N. Kenwright. "Automatic detection of open and closed separation and attachment lines". In: *Visualization'98. Proceedings.* IEEE. 1998, pages 151–158.

[KHL99] D. N. Kenwright, C. Henze, and C. Levit. "Feature extraction of separation and attachment lines". *IEEE Transactions on Visualization and Computer Graphics* 5:2, 1999, pages 135–144. ISSN: 1077-2626. DOI: 10.1109/2945.773805.

[KMP07] M. Kilian, N. J. Mitra, and H. Pottmann. "Geometric modeling in shape space". In: *ACM Transactions on Graphics (TOG).* Volume 26. 3. ACM. 2007, **page** 64.

[Kuh*12] A. Kuhn, C. Rössl, T. Weinkauf, and H. Theisel. "A benchmark for evaluating FTLE computations". In: *Visualization Symposium (PacificVis), 2012 IEEE Pacific.* IEEE. 2012, pages 121–128.

[Kuz06] Y. A. Kuznetsov. "Saddle-node bifurcation". *Scholarpedia* 1:10, 2006. revision #151865, **page** 1859. DOI: 10.4249/scholarpedia.1859.

[Lar*07] R. S. Laramee, H. Hauser, L. Zhao, and F. H. Post. "Topology-based flow visualization, the state of the art". In: *Topology-based methods in visualization.* Springer, 2007, pages 1–19.

[LC87] W. E. Lorensen and H. E. Cline. "Marching cubes: A high resolution 3D surface construction algorithm". In: *ACM siggraph computer graphics.* Volume 21. 4. ACM. 1987, pages 163–169.

[Lin98] T. Lindeberg. "Edge detection and ridge detection with automatic scale selection". *International Journal of Computer Vision* 30:2, 1998, pages 117–156.

[LSD90] Y. Levy, A. Seginer, and D. Degani. "Graphical visualization of vortical flows by means of helicity". *AIAA journal* 28:8, 1990, pages 1347–1352.

[Mac*16] G. M. Machado, S. Boblest, T. Ertl, and F. Sadlo. "Space-Time Bifurcation Lines for Extraction of 2D Lagrangian Coherent Structures". *Computer Graphics Forum* 35:3, 2016, pages 91–100. DOI: 10.1111/cgf.12885.

[Man*03] A. M. Mancho, D. Small, S. Wiggins, and K. Ide. "Computation of stable and unstable manifolds of hyperbolic trajectories in two-dimensional, aperiodically time-dependent vector fields". *Physica D: Nonlinear Phenomena* 182:3-4, 2003, pages 188–222.

[Mar*16] R. S. Martins, A. S. Pereira, G. Mompean, L. Thais, and R. L. Thompson. "An objective perspective for classic flow classification criteria". *Comptes Rendus Mecanique* 344:1, 2016, pages 52–59.

[MAT18] MATLAB. *version (R2018a).* The MathWorks Inc., Natick, Massachusetts, 2018.

[MH94] J. E. Marsden and T. J. Hughes. *Mathematical foundations of elasticity.* Courier Corporation, 1994.

[MSE13] G. M. Machado, F. Sadlo, and T. Ertl. "Local Extraction of Bifurcation Lines". In: *Proceedings of International Workshop on Vision, Modeling and Visualization (VMV)*. 2013, pages 17–24. DOI: 10.2312/PE.VMV.VMV13.017-024.

[PC12] T. S. Parker and L. Chua. *Practical numerical algorithms for chaotic systems*. Springer Science & Business Media, 2012.

[PC87] A. E. Perry and M. S. Chong. "A description of eddying motions and flow patterns using critical-point concepts". *Annual Review of Fluid Mechanics* 19:1, 1987, pages 125–155.

[Pob*11] A. Pobitzer, R. Peikert, R. Fuchs, B. Schindler, A. Kuhn, H. Theisel, K. Matković, and H. Hauser. "The state of the art in topology-based visualization of unsteady flow". In: *Computer Graphics Forum*. Volume 30. 6. Wiley Online Library. 2011, pages 1789–1811.

[Pos*03] F. H. Post, B. Vrolijk, H. Hauser, R. S. Laramee, and H. Doleisch. "The state of the art in flow visualisation: Feature extraction and tracking". In: *Computer Graphics Forum*. Volume 22. 4. Wiley Online Library. 2003, pages 775–792.

[PR99] R. Peikert and M. Roth. "The "parallel vectors" operator: a vector field visualization primitive". In: *Proceedings of the conference on Visualization'99: celebrating ten years*. IEEE Computer Society Press. 1999, pages 263–270.

[Rot00] M. Roth. *Automatic extraction of vortex core lines and other line type features for scientific visualization*. Volume 2. Hartung-Gorre, 2000.

[RP98] M. Roth and R. Peikert. "A higher-order method for finding vortex core lines". In: *Proceedings of the conference on Visualization'98*. IEEE Computer Society Press. 1998, pages 143–150.

[Sad10] F. Sadlo. "Computational Visualization of Physics and Topology in Unsteady Flow". PhD Dissertation No. 19284. ETH Zurich, 2010. DOI: 10.3929/ethz-a-006435276.

[Sah*07] J. Sahner, T. Weinkauf, N. Teuber, and H.-C. Hege. "Vortex and strain skeletons in eulerian and lagrangian frames". *IEEE Transactions on Visualization and Computer Graphics* 13:5, 2007, pages 980–990.

[Sch*97] G. Scheuermann, H. Hagen, H. Kruger, M. Menzel, and A. Rockwood. "Visualization of higher order singularities in vector fields". In: *Visualization'97., Proceedings*. IEEE. 1997, pages 67–74.

[SH95a] D. Stalling and H.-C. Hege. "Fast and resolution independent line integral convolution". In: *Proceedings of the 22nd annual conference on Computer graphics and interactive techniques*. ACM. 1995, pages 249–256.

[SH95b] D. Sujudi and R. Haimes. "Identification of swirling flow in 3-D vector fields". In: *12th Computational Fluid Dynamics Conference*. 1995, **page** 1715.

[SLM05] S. C. Shadden, F. Lekien, and J. E. Marsden. "Definition and properties of Lagrangian coherent structures from finite-time Lyapunov exponents in two-dimensional aperiodic flows". *Physica D: Nonlinear Phenomena* 212:3-4, 2005, pages 271–304.

[SP09] F. Sadlo and R. Peikert. "Visualizing Lagrangian Coherent Structures and Comparison to Vector Field Topology". In: *Topology-Based Methods in Visualization II*. Springer Berlin Heidelberg, 2009, pages 15–29. DOI: 10.1007/978-3-540-88606-8_2.

[SV52] M de Saint-Venant. "Surfaces à plus grande pente constituées sur des lignes courbes". *Bulletin de la Société Philomathématique de Paris*, 1852, pages 24–30.

[SW10] F. Sadlo and D. Weiskopf. "Time-Dependent 2-D Vector Field Topology: An Approach Inspired by Lagrangian Coherent Structures". *Computer Graphics Forum* 29:1, 2010, pages 88–100. DOI: 10.1111/j.1467-8659.2009.01546.x.

[SWH05] J. Sahner, T. Weinkauf, and H.-C. Hege. "Galilean invariant extraction and iconic representation of vortex core lines." In: *EuroVis*. 2005, pages 151–160.

[TCH11] W. Tang, P. W. Chan, and G. Haller. "Lagrangian coherent structure analysis of terminal winds detected by lidar. Part I: Turbulence structures". *Journal of Applied Meteorology and Climatology* 50:2, 2011, pages 325–338.

[The*05a] H. Theisel, J. Sahner, T. Weinkauf, H.-C. Hege, and H.-P. Seidel. "Extraction of parallel vector surfaces in 3D time-dependent fields and application to vortex core line tracking". In: *VIS 05. IEEE Visualization, 2005*. IEEE. 2005, pages 631–638.

[The*05b] H. Theisel, T. Weinkauf, H.-C. Hege, and H.-P. Seidel. "Topological methods for 2D time-dependent vector fields based on stream lines and path lines". *IEEE Transactions on Visualization & Computer Graphics* 4, 2005, pages 383–394.

[TK94] M. Tabor and I Klapper. "Stretching and alignment in chaotic and turbulent flows". *Chaos, Solitons & Fractals* 4:6, 1994, pages 1031–1055.

[TN04] C. Truesdell and W. Noll. "The non-linear field theories of mechanics". In: *The non-linear field theories of mechanics*. Springer, 2004, pages 1–579.

[TS03] H. Theisel and H.-P. Seidel. "Feature Flow Fields". In: *Proc. Joint Eurographics - IEEE TCVG Symposium on Visualization (VisSym'03)*. 2003, pages 141–148.

[TSH01] X. Tricoche, G. Scheuermann, and H. Hagen. "Topology-Based Visualization of 2D Time-Dependent Vector Fields". In: *Joint EUROGRAPHICS - IEEE TCVG Symposium on Visualization (2001)*. **byeditor**D. S. Ebert, J. M. Favre, and R. Peikert. Springer Vienna, Vienna, 2001, pages 27–42. ISBN: 978-3-7091-6215-6. DOI: 10.1007/978-3-7091-6215-6_13. URL: http://dx.doi.org/10.1007/978-3-7091-6215-6_13.

[ÜSE13] M. Üffinger, F. Sadlo, and T. Ertl. "A Time-Dependent Vector Field Topology Based on Streak Surfaces". *IEEE Transactions on Visualization and Computer Graphics* 19:3, 2013, pages 379–392. DOI: 10.1109/TVCG.2012.131.

[Ver06] F. Verhulst. *Nonlinear differential equations and dynamical systems*. Springer Science & Business Media, 2006.

[Wei*05] T. Weinkauf, H. Theisel, K. Shi, H.-C. Hege, and H.-P. Seidel. "Extracting higher order critical points and topological simplification of 3D vector fields", 2005.

[Wei*07a] T. Weinkauf, H. Theisel, H.-C. Hege, and H.-P. Seidel. "Feature Flow Fields in Out-of-Core Settings". In: *Proc. Topo-In-Vis 2005*. 2007, pages 51–64.

[Wei*07b] T. Weinkauf, J. Sahner, H. Theisel, and H.-C. Hege. "Cores of swirling particle motion in unsteady flows". *IEEE Transactions on Visualization and Computer Graphics* 13:6, 2007, pages 1759–1766.

[Wei*10] T. Weinkauf, H. Theisel, A. V. Gelder, and A. Pang. "Stable Feature Flow Fields". *IEEE Transactions on Visualization and Computer Graphics*, 2010. URL: http://tinoweinkauf.net/.

[WGS02] A. Wiebel, C. Garth, and G. Scheuermann. "Computation of localized flow for steady and unsteady vector fields and its applications". *IEEE Trans. Visualization and Computer Graphics* 1:8, 2002.

[Wie*07] A. Wiebel, X. Tricoche, D. Schneider, H. Jaenicke, and G. Scheuermann. "Generalized streak lines: Analysis and visualization of boundary induced vortices". *IEEE Transactions on Visualization and Computer Graphics* 13:6, 2007, pages 1735–1742.

[Wig03] S. Wiggins. *Introduction to applied nonlinear dynamical systems and chaos*. Volume 2. Springer Science & Business Media, 2003.

[WSG04] A. Wiebel, G. Scheuermann, and C. Garth. "Feature detection in vector fields using the Helmholtz-Hodge decomposition". *Master's thesis. University of Kaiserslautern*, 2004.

[WT10] T. Weinkauf and H. Theisel. "Streak lines as tangent curves of a derived vector field". *IEEE Transactions on Visualization and Computer Graphics* 16:6, 2010, pages 1225–1234.